High Resolution Dynamics Limb Sounder

Level-2
Algorithm Theoretical Basis Document

Alyn Lambert[1], Paul L. Bailey[1], David P. Edwards[1], John C. Gille[1,2],
Brian R. Johnson[1], Chris M. Halvorson[1], Steven T. Massie[1], Ken A. Stone[2]

[1]National Center for Atmospheric Research, Boulder
[2]University of Colorado, Boulder
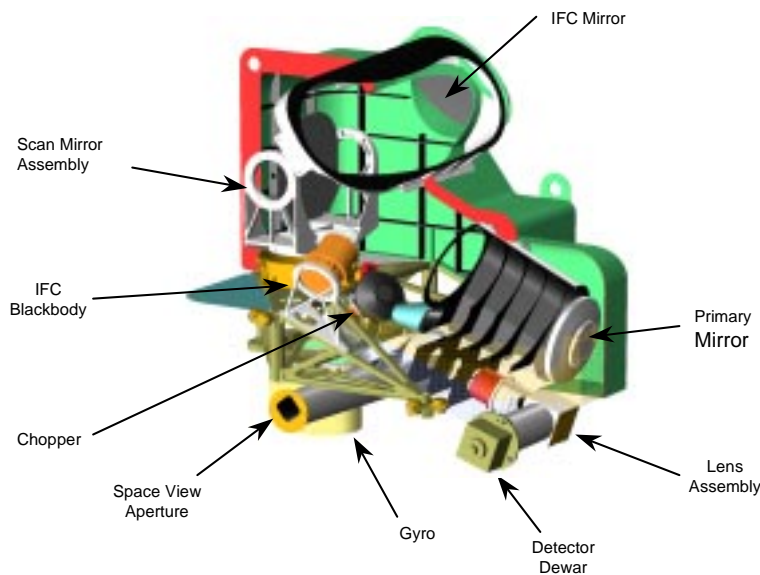
Version 2 October 1999

Contents

Abstract

In this document we describe the scientific basis of the Level-2 processor algorithms to be used for the High Resolution Dynamics Limb Sounder (HIRDLS) that is scheduled to fly on the chemistry platform of the Earth Observing System (EOS) mission (EOS-CHEM). The Level-2 processing stage ingests the Level-1 calibrated radiance data and generates the Level-2 product data consisting of atmospheric profiles of geophysical quantities such as temperature and constituent mixing ratios on a pressure grid. HIRDLS is a joint US-UK project between the University of Colorado at Boulder and the University of Oxford.

The HIRDLS instrument is a 21-channel infrared limb-scanning radiometer designed to sound an altitude range from the upper troposphere to the mesosphere to determine profiles of temperature, trace gas concentrations, aerosols, and the location of polar stratospheric clouds and cloud tops. The goals are to provide sounding observations with a horizontal and vertical resolution superior to those previously obtained, to observe the lower stratosphere with improved sensitivity and accuracy, and to improve understanding of atmospheric processes through data analysis, diagnostics, and the use of two- and three-dimensional models.

This release of the Level-2 ATBD applies specifically to the algorithms under development for the engineering version delivery. Updates of this document will be provided at appropriate stages to incorporate changes arising from the evaluation and refinement of the Level-2 processor algorithms.

1   Introduction

The purpose of this Algorithm Theoretical Basis Document is to present the physical and mathematical principles that underlie the algorithms to be developed by the High Resolution Dynamics Limb Sounder (HIRDLS) team to extract geophysical information from the radiances measured by the HIRDLS instrument. This processing of the data will lead to the retrieval of atmospheric temperature, the mixing ratios of 10 trace gases, the distribution of atmospheric aerosols, and cloud top heights, all with atmospheric pressure as the vertical profile.

The inputs to these algorithms will be the calibrated, geolocated radiances contained in the HIRDLS Level-1 data, resulting from the previous processing of the raw HIRDLS instrument output with associated ephemeris and spacecraft (S/C) information. Application of the algorithms will produce, as outputs, the HIRDLS Level-2 data, containing high vertical resolution profiles of the retrieved quantities, spaced $5°$ or less in longitude and latitude to provide higher horizontal resolution that has been achieved previously.

Section 2 of this document provides a brief summary of the experiment objectives, some historical background, and a description of the instrument, with emphasis on the selection of the spectral channels, and the treatment of aerosols. The algorithms themselves are described in Section 3, which presents the preprocessing of the radiances, the forward model, and the retrieval algorithm, including the error analysis. Section 4 describes the Evaluation and Testing of the algorithms, and is followed by discussions of Practical Considerations, Calibration and Validation, Quality Control and Diagnostics. Details of radiance and weighting function calculations are included in an appendix.

2   Overview and Background Information

2.1   Experimental Objective

Concerns for the stability of the Earth's ozone layer have dominated research attention on the stratosphere and mesosphere since the middle 1970s, when attention originally focussed on the impact of supersonic aircraft, but quickly shifted to the effects of chlorine released by photolysis of anthropogenic chlorofluorocarbons. The unexpected discovery of the rapid decline of the springtime ozone column over Antarctica resulted in many new measurements, theories and models, including chemistry taking place on particles, that provide a great deal of clarity on the processes involved. The development of our understanding of atmospheric dynamics has been less dramatic but no less important. Theoretical developments and observational studies have fundamentally changed the picture of the planetary scale circulation. These developments have had far-reaching implications for our understanding of the general circulation of the middle atmosphere, and the associated transport and mixing of trace

constituents. Taken together, these advances have clarified our understanding of the ozone layer, and resulted in the Montreal Protocol and related agreements to phase out a wide range of species implicated in ozone depletion.

More recently attention is being paid to questions of global change and the possible effects of human activities on the climate system. As part of this study, the role of the stratosphere and stratospheric processes in climate has emerged as a critical area of study. The picture of the structure of the lower stratosphere and upper troposphere has been clarified, but there are still enduring questions about the ways in which exchange between these regions takes place. In addition, the distributions of particulates and radiatively important trace gases, such as ozone and especially water vapor, are not known well enough. For water there is not enough information to look for evidence of long term trends.

The general objectives of HIRDLS then are twofold; to provide information to assess the role of the stratosphere, especially the lower stratosphere and the upper troposphere (UT/LS) in climate processes; and to observe the processes that affect the stratospheric ozone layer at a time when the concentrations of active chlorine have reached a maximum and are beginning to decrease. These data will improve our understanding of the dynamics of these chemical and dynamical processes, and improve our ability to model the future evolution of the atmosphere. These objectives are fully consistent with the objectives of the NASA Earth Science Enterprise.

2.1.1   Principal Scientific Objectives

Seven principal scientific objectives have been chosen as the focus of the investigations for which the HIRDLS Science Team intends to use the data that is produced by the HIRDLS instrument. These objectives are:

1. To understand the fluxes of mass and chemical constituents (including greenhouse gases and aerosols) that affect the dynamics and composition of the troposphere, stratosphere, mesosphere, and thermosphere and link these regions together. These fluxes must be determined down to smaller scales than previously observed.

2. To understand the chemical processing, transport, and small-scale irreversible mixing of trace constituents in the middle atmosphere, including the chemical and dynamical processes responsible for creating the antarctic (and perhaps arctic) ozone holes.

3. To understand the momentum, energy, and potential vorticity balances of the middle atmosphere, by extending global observations to smaller horizontal and vertical scales than has previously been possible. These small-scale processes are believed to be fundamentally important to the determination of some large-scale characteristics and are thought to cause irreversible chemical mixing.

4. To obtain climatologies of upper tropospheric, stratospheric, and mesospheric quantities, in particular, profiles of temperature, ozone, several radiatively active gases, aerosol, gravity wave activity, and cloud top heights. Seasonal, interannual, and long-term trends will be obtainable because of the five-year measurement sequence that will be provided by each Earth Observing System (EOS) instrument, combined with pre-EOS measurements and future EOS observations.

5. To provide data to validate and improve numerical models of the atmosphere, in order to gain confidence in their ability to predict climate change. These simulations are critically dependent on the treatment of horizontal and vertical scales that are much finer than those currently observed.

6. To improve the understanding of tropospheric chemistry through the use of temperature and constituent retrievals that extend into the upper troposphere, under favorable conditions. The combination of these observations with observations from other EOS instruments, and with chemical models, will yield information about the oxidation capacity of the atmosphere.

7. To improve the understanding of stratospheric and tropospheric aerosols and clouds by acquiring long-term high-resolution observations of their nature and distribution. Aerosols and polar stratospheric clouds are now known to play essential roles in the depletion of ozone in the lower stratosphere, and subvisible cirrus clouds in the upper troposphere significantly impact the radiative heating and cooling of the atmosphere.

A number of particular problems were identified to address these objectives, and used to define the requirements on the geophysical data to be returned by the experiment. These are summarized in Table 1. The HIRDLS

Temperature		Altitude Range	Precision	Absolute
		< 50 km	0.4 K	1 K
		> 50 km	1.0 K	2 K
Constituents	O_3, H_2O, CH_4, N_2O, NO_2, HNO_3, N_2O_5, $ClONO_2$, CFC11, CFC12		1 – 5 %	5 – 10 %
	Aerosol spectral extinction		1 – 5 %	25 %
Horizontal geopotential height gradient		Temporal	Vertical	Horizontal
			20 m	500 km
Equivalent 60ºN geostrophic wind				3 m/s
Coverage			8 – 80 km Upper troposphere to mesopause	Global , pole to pole (including polar night)
Resolution		Global field in 12 hours	1 – 1.25 km	5º x 5º latitude longitude

Table 1: HIRDLS Measurement Requirements.

measurement requirements aim for a temperature precision of 0.4 K and accuracy of 1 K below 50 km, and a precision of 1 K and accuracy of 2 K above 50 km. For the constituent measurements, a precision of 1–5 % and accuracy of 5–10 % is expected, depending on species. The measurement of anthropogenic fluorocarbons, CFC11 ($CFCl_3$) and CFC12 (CF_2Cl_2), is important because of the role of the chlorine released from their photolysis in the destruction of stratospheric O_3, and as greenhouse gases. A limb sounder such as HIRDLS is able to obtain useful information about the fall-off of these species in the middle stratosphere so allowing for their use as tracers in dynamical studies. HIRDLS will retrieve profiles of four gases, HNO_3, N_2O_5 N_2O, and NO_2, to provide information on global distribution and diurnal variation of nitrogen species for chemistry and transport studies.

The aerosol loading of the lower stratosphere is highly variable and can change suddenly, by several orders of magnitude, due to a major volcanic eruption. It then requires 2 years or more to return once again to background levels. The increase in the atmospheric absorption and emission causes the signal from trace gas sources to be severely contaminated below about 25 km.

Measurements of the spectral variation of the aerosol extinction allow the effect to be included in the trace gas retrievals. According to Mie theory, the spectral variation over the infrared depends on the aerosol type and size distribution. Sulfate aerosol is the main concern here along with polar stratospheric clouds in the winter polar regions. By measuring aerosol extinction in several channels the assumed spectral variation can be verified and used to correct for aerosol effects in the trace gas channels. For this reason, HIRDLS has 4 aerosol channels interspersed among the 17 gas sounding channels.

Modern infrared filter manufacturing technology allows the instrument to use narrow channel spectral pass-bands, of full width at half maximum (FWHM) better than 1 % of the central wavenumber, when this is desirable to isolate the emission of a particular trace gas. Four relatively narrow channels at spectral positions having low

optical depth and interspersed over the full spectral range allow background aerosol measurements to be made. This allows the spectral variation of the aerosol continuum emission to be characterized.

HIRDLS will obtain profiles over the entire globe, including the poles, during both day and night. Complete Earth coverage, including polar night, can be obtained in 12 hours. High horizontal resolution is obtained with a commandable azimuth position which, in conjunction with a rapid elevation scan, provides a 2000–3000 km wide swath of profiles along the satellite track. Vertical profiles are spaced every $5°$ in latitude and longitude, with a 1–1.5 km vertical resolution. HIRDLS will measure infrared limb emission in the 21 channels shown in Table 2 which range in frequency from 575–1608 cm^{-1} (17.4–6.22 μm). Each channel will be used to make retrievals over the widest possible altitude range.

2.2 Historical Perspective

The first successful proposal for the flight of an infrared limb viewing radiometer was that for the Limb Radiance Inversion Radiometer (LRIR), put forward for flight on Nimbus 6. Initial difficulties caused by the stringent requirements on pointing knowledge were solved by Gille and House (1971), who showed how the limb measurements themselves could be used to make this determination, or equivalently to solve for the vertical temperature profile as a function of pressure as a vertical coordinate. LRIR was launched in June, 1975; a brief discussion of its measurements of temperature and ozone is contained in Gille *et al.*(1980a,b).

A similar instrument, the Limb Infrared Monitor of the Stratosphere (LIMS) was flown on Nimbus 7 (Gille and Russell, 1984). It added the capabilities to measure water vapor, nitrogen dioxide, and nitric acid to the LRIR capabilities. Another limb sounder, the Stratosphere and Mesosphere Sounder (SAMS) also flew on Nimbus 7, measuring notably temperature, methane and nitrous oxide [*Drummond et al.*(1980)]. The results from these instruments added greatly to knowledge of stratospheric dynamics and chemistry.

Two infrared limb viewers flew on the Upper Atmosphere Research Satellite (UARS). The Improved Stratosphere and Mesosphere Sounder (ISAMS), a limb scanner [*Taylor et al.*(1993)] and the Cryogenic Limb Array Etalon Spectrometer (CLAES) [*Roche et al.*(1993)], a limb-staring instrument. These instruments together measured temperature and the distributions of ozone, water vapor, methane, nitrous oxide, nitric acid, nitrogen dioxide, chlorofluorocarbon 11 and 12, carbon monoxide and nitric oxide. In addition they determined the distributions and composition of aerosols. These measurements have greatly added to our knowledge of the distribution of trace species and aerosols in the stratosphere and mesosphere, and the processes that maintain them.

The HIRDLS algorithms will build on the heritage of these earlier precursors and the knowledge gained from them. All of these instruments were limited to viewing in a single azimuth at any time, and thus the longitudinal spacing of the retrieved profiles was set by the orbital spacing, approximately 25 degrees.

2.3 Instrument Characteristics

2.3.1 Limb Emission Measurement Technique

The fundamental measurement in infrared limb scanning is the atmospheric radiance as a function of the relative altitude of the line-of-sight of the instrument as it is scanned across the limb; measurement of thermal emission from satellites permits global coverage, both day and night (including the polar night). The vertical distribution of atmospheric quantities, such as temperature or ozone concentration, can be determined with high vertical resolution (e.g. $< 1 - 2$ km) using this technique. Because of the combination of the limb geometry and the exponential fall off of density with altitude, most of the contribution to observed radiance arises from very near to the tangent point. The limb weighting function is further broadened by the instrument field of view which therefore should be limited to 1–2 km at the limb. All the radiation reaching the instrument originates from atmospheric emission; contributions to the signal from the cold space background are negligible and therefore signal variations at the entrance aperture of the instrument are due only to variations in atmospheric emission. The significantly longer gas emission path along the limb results in a larger emission signal enabling measurement of the more tenuous gas concentrations to higher altitudes. The upper altitude limit of vertical coverage is set when the signal-to-noise becomes too low. The lower altitude limit is determined by limb opacity, including the presence of thick aerosol or clouds.

During the data reduction process, the measured vertical profiles of the radiance emitted by CO_2 (which has a known distribution in the atmosphere) provide almost all the information that is inverted to determine the temperature of the atmosphere as a function of pressure (i.e. the altitude). Limb observations in at least two spectral bands with differing optical properties located near the 15 μm band of CO_2 allow a self-consistent reference pressure to be found by requiring that the temperatures derived from all spectral channels be the same [*Gille and House* (1971)]. The relative pressure levels between radiance samples are determined by knowing the relative line-of-sight angle between samples. The "two color" technique of Gille and House alleviates the stringent requirements for precise absolute knowledge and control of spacecraft attitude and position. The temperature and pressure information are therefore retrieved simultaneously. The retrieved temperature profile information is combined with measured vertical profiles of radiance emitted by other gases or aerosols to determine their vertical distributions. Finally, regional and global maps of the temperature, and gas and aerosol concentrations can be constructed from the vertical profiles.

2.3.2 Instrument Requirements

The geophysical quantities derived from HIRDLS observations must be accurately and precisely determined to address the scientific objectives discussed in Section 2.1. Systematic and random errors in the radiometry, and knowledge of the line-of-sight position between samples are translated into inaccuracy and imprecision in retrieved quantities. Consequently, those instrument characteristics that affect measured radiances and those that define relative pointing knowledge must be accurately and precisely determined.

Systematic error in knowledge of the observed radiance must be 1 % or less for all spectral channels with a goal of 0.5 % for the critical temperature sounding channels (Channels 2–5). The radiometric noise in each channel must be less than or equal to the noise values given in Table 2 for an effective measurement bandwidth of 7.5 Hz. Also shown in Table 2 are the required 50 % spectral response points and tolerances for each channel. For limb observations, it is necessary to reduce incident spectral radiation falling outside of the spectral band to low levels, particularly for those channels located near strong interfering emission features. The requirement is therefore that the integrated response for out-of-spectral band radiation (outside of the 0.2 % response points) must be less than 1 % of the total integrated in-band response.

The end-to-end vertical response function of each channel must have a full width at half maximum of 1 km when measured at the limb. The presence of strong off-axis earth radiation places demanding requirements on reduction of diffracted radiation and radiation scattered by optical surfaces. The total integrated off-axis radiation for relative altitudes greater than 4 km from the center of the detector FOV must be less than 1 % of the total integrated response. This requirement may be relaxed slightly with accurate knowledge of the off-axis response, which permits corrections for stray radiation to be made in data processing.

As discussed in the previous section, it is not necessary to know the absolute LOS elevation angle, however it is critical to know the relative elevation angle between radiance samples. For a single elevation scan, the systematic error in the knowledge of the relative elevation angle for any two radiance samples that are measured within the same channel must be less than 0.25 % of the nominal angular spacing or 0.35 arcsec, whichever is greatest. The random error in knowledge of the relative LOS spacing within an effective bandwidth of 7.5 Hz, must be less than 1 arcsec, with a design goal of 0.7 arcsec. These values include the effects of the imprecision in the measurement of the relative LOS angles, and the motions and vibrations of the spacecraft and the instrument.

Additional requirements on pointing knowledge, and consequently on the gyroscope and the mechanical stability of the optical bench, come from the requirement to derive gradients in the geopotential height of a pressure surface. Knowledge of the relative LOS angles between separate elevation scans is driven by the desire to derive geostrophic winds from gradient measurements with a precision of 3 m/s at mid-latitudes. This translates into a required precision in derived geopotential height gradient of approximately 20 m over a distance of about 500 km, the nominal distance between elevation scans. Therefore, the relative vertical registration between elevation scans must be known to better than 1.4 arcsec (rms) for adjacent elevation scans (separated by approximately 10 sec), for any two elevation scans within an azimuth swath ($\leq$ 66 sec apart), or for elevations scans separated by one orbit ($\sim$100 min. apart).

The elevation scan range must be sufficiently large to allow each channel to view the atmospheric sounding range and extend well above the upper tangent height specified in Table 1, at all points along the spacecraft orbit.

Channel	Species	50% Response (cm^{-1})		Sounding Range (km)	Radiometric Noise (10^{-4} Wm^{-2}sr^{-1})
		Lower	Upper		
1	N_2O, A	563.50 ± 2.0	587.25 ± 1.0	8–70	12.0
2	CO_2-L	600.50 ± 2.0	614.75 ± 1.0	8–40	6.3
3	CO_2-M	610.00 ± 3.0	639.50 ± 2.0	8–60	5.9
4	CO_2-M	626.00 ± 3.0	660.00 ± 3.0	15–60	6.0
5	CO_2-H	655.00 ± 3.0	680.00 ± 2.0	30–105	4.3
6	A	821.50 ± 2.3	835.00 ± 2.4	8–55	1.9
7	CFC11	835.00 ± 2.4	852.00 ± 2.4	8–50	2.0
8	HNO_3	861.50 ± 2.5	903.50 ± 2.5	8–70	4.2
9	CFC12	916.00 ± 2.6	931.50 ± 2.6	8–50	2.0
10	O_3-M	991.00 ± 2.8	1009.00 ± 2.8	8–55	1.5
11	O_3-H	1011.00 ± 2.9	1046.50 ± 2.9	30–85	2.4
12	O_3-L	1120.00 ± 3.2	1138.50 ± 3.2	8–55	0.96
13	A	1202.00 ± 3.4	1259.75 ± 3.4	8–55	1.1
14	N_2O_5	1229.50 ± 2.0	1259.75 ± 1.0	8–60	1.1
15	N_2O	1256.25 ± 1.0	1281.75 ± 1.0	8–70	1.1
16	$ClONO_2$	1278.25 ± 1.0	1298.75 ± 1.0	8–70	1.1
17	CH_4	1325.50 ± 3.8	1367.50 ± 3.8	8–80	1.2
18	H_2O-L	1387.00 ± 4.0	1435.00 ± 4.0	8–40	1.2
19	A	1402.25 ± 1.0	1415.75 ± 1.0	8–55	1.3
20	H_2O-H	1422.00 ± 4.1	1542.00 ± 4.3	15–85	1.6
21	NO_2	1585.50 ± 4.5	1630.50 ± 4.6	8–70	1.1

Table 2: HIRDLS spectral channels, sounding ranges and radiometric noise requirements. The sounding ranges represent the tangent heights over which useful retrievals will be possible and includes an additional 15 km at the upper boundary required for the retrieval process. The letters L, M and H indicate low, mid and high altitudes sounding ranges; A denotes aerosol.

The azimuth position range must extend as close to the direction of the sun as possible, on one side, and far enough on the other side to overlap one or more scan tracks from the adjacent orbit. A door/sunshade can be used to extend the scan range on the sun side and prevent direct sunlight from entering the viewing aperture. Over the entire atmospheric sounding range, the absolute azimuth angle must be known with an error of at most 0.1°. The error in the knowledge of the relative azimuth angle of each channel between two adjacent elevation scans must be at most 0.04°. This applies whether the two adjacent altitude scans are at a single azimuth position, at two azimuth positions that are sequential along the orbit, or at two azimuth positions at approximately the same latitude from successive orbits.

The instrument must be controlled by a microprocessor programmable from the ground. The instrument processor must be capable of controlling the moveable sunshield, elevation scanning and azimuth positioning, signal processing and conditioning, and the collection of engineering data. The processor must also prepare both scientific and engineering data for output to the spacecraft telemetry stream.

2.3.3 HIRDLS Instrument Overview

The High Resolution Dynamics Limb Sounder is an infrared limb-scanning radiometer designed to measure atmospheric limb emission in 21 spectral channels operating over the wavelength range from 6 to 18 μm. Requirements for increased vertical and horizontal resolution, the ability to sound down into the lower stratosphere and upper troposphere, and the ability to measure simultaneously a large number of trace species with a range of chemical lifetimes, necessitate improvements over previous limb scanning instruments. Limb scanners, such as LIMS and ISAMS, provided vertical resolution of about 2 to 3 km, but their longitudinal sampling was limited to approximately 2600 km at the equator (and half that at 60° latitude). HIRDLS will improve on the capabilities of previous limb scanners by incorporating azimuth scanning to obtain a horizontal spacing between vertical profiles of roughly 5° or 500 km at the equator. Furthermore, the vertical resolution will be increased by continuously scanning a narrow 1-km vertical field-of-view and over-sampling the vertical radiance profile nominally every 0.2 km. Detailed simulations have shown that spatial features having wavelengths 1.5 km can be adequately resolved. A schematic diagram of the HIRDLS instrument is shown in Figure 1.

2.3.3.1 HIRDLS subsystems. The instrument consists of nine subsystems; the key subsystems are described below. The structural-thermal subsystem (STH) provides an outer cover to create a stable mechanical and thermal environment for the instrument, a radiator panel for removing heat from the mechanical cryocooler, and a baseplate on which the telescope subsystem is mounted. The instrument views rearward from the spacecraft with the boresight inclined approximately 25 degrees from the local horizon. A sunshield subsystem (SSH) controls a moveable door to prevent sunlight from directly illuminating the instrument aperture when the satellite is in the high latitude portion of the orbit.

2.3.3.1.1 Telescope subsystem. Limb radiation enters the instrument aperture and is collected by the optical telescope after reflection off the flat scan mirror. The telescope subsystem (TSS) consists of a two-axis scan mirror, an off-axis, 3-mirror Gregorian reflective telescope, and two Ge lenses to relay the image of the atmosphere produced by the telescope onto the focal plane consisting of 21 infrared detectors while maintaining good image quality. The optical system is designed to image a 1-km vertical dimension at the atmospheric limb a distance of 3000 km away onto detectors with a vertical dimension of 82 μm. The telescope forms an f/2.5 intermediate image at the focus of the off-axis parabolic primary mirror. The secondary, an off-axis ellipse, re-images this to a good quality but slow image which is transferred by Ge lenses to a nearly diffraction limited f/1.5 image at the detectors. A Lyot stop system is used to control diffracted stray radiation. The scan mirror (SMA) rotates about two axes to view the field at a given azimuth angle (variable over a 60° range) and scan in elevation angle to view the desired part of the atmospheric limb or to view the collimated beam of a small, high quality blackbody for in-flight radiometric calibration (IFC). The entrance pupil diameter is approximately 160 mm with an effective focal length of the optical system of 245 mm. Incoming atmospheric radiation, collected by the primary mirror, is mechanically chopped at a nominal frequency of 500 Hz by a reflective rotary chopper located at the first focal plane. The chopper reflects a view of space via a relay mirror to the detectors when closed.
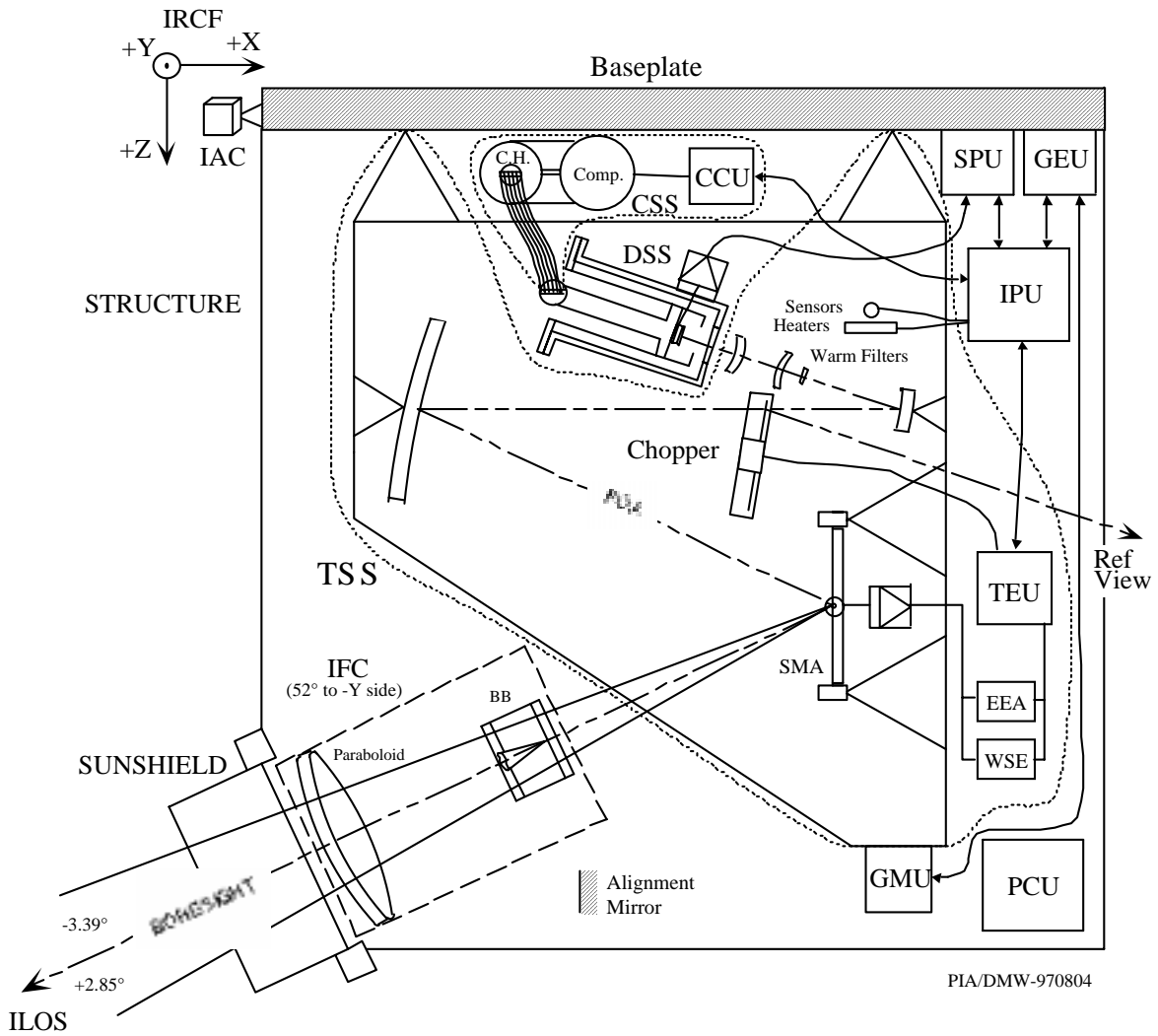
Figure 1: Schematic diagram of the HIRDLS instrument identifying the subsystems discussed in Section 2.3.3.

2.3.3.1.2   In-flight radiometric calibration.   In-flight calibration is performed by turning the scan mirror to view the IFC blackbody via a parabolic calibration mirror. The blackbody is designed to have high emissivity, small thermal gradients and its temperature precisely monitored by high quality platinum resistance thermometers. The calibration mirror temperature is controlled to within 1 K of the IFC blackbody temperature to minimize radiometric error due to uncertainty in the IFC mirror emissivity. The nominal calibration period is 66 seconds. This provides an end-to-end gain calibration point using the same optical configuration as used in limb measurements. A zero radiance calibration point is provided every 10 seconds by viewing cold space at the top of each vertical profile.

2.3.3.1.3   Spectral bandpass filters.   Spectral selection is achieved through the use of 21 individual interference filters operating at ambient temperature and located at an intermediate focal plane. A second set of filters is located on the cold focal plane in close proximity to the detectors, having roughly twice the spectral bandpass of the warm filters. The cold filters are necessary to achieve a high level of out-of-band spectral blockage and to significantly reduce unwanted optical cross talk due to scattering by or internal reflections from the Ge lens relay system. The thickness of the substrate of each of the cold filters is selected to compensate for the small residual longitudinal chromatic aberration in the relay system.

2.3.3.1.4   Detector focal plane.   The detector focal plane dimensions and the relative positions of the spectral channels are shown in Figure 2. The center detector column has been offset from the middle to allow room for electrical connections to be made. The physical size of detector elements is $82\ \mu\text{m} \times 820\ \mu\text{m}$, with a corresponding angular FOV of 0.332 mrad $\times$ 3.32 mrad. The vertical dimension of the instantaneous detector FOV is 1-km at the limb, with a horizontal dimension of 10 km. The composite field-of-view is 55 km $\times$ 55 km. The alignment quad-cell detector at the top of the array is to facilitate pre-flight testing of the line-of-sight and will not be operational in-flight.

2.3.3.1.5   Field of view and pointing.   The detector fields-of-view are alternately scanned upward and downward across the limb at a nominal scan rate of 0.3 deg/sec in the global observation mode. The angular position of the scan mirror relative to the optical bench is measured by optical encoders every 12 msec, corresponding to approximately 14 arcsec. Any inertial motion of the optical bench produced by spacecraft and instrumental disturbances will introduce undesired motion of the LOS, which will not be sensed by the encoders. It is expected that data from the spacecraft attitude control system will not be of sufficient precision nor will the relationship between the spacecraft gyro and HIRDLS line-of-sight be known precisely enough to meet this requirement. Therefore, a multi-axis gyroscope is mounted to the optical bench to measure bench motion relative to inertial space, making corrections to pointing knowledge possible. The gyroscope subsystem (GSS) consists of a mechanical unit, which is mounted directly to the optical bench providing angular motion measurements of the bench. The gyroscope unit is a GEC-Marconi Avionics Type 125 gyro with an electronic unit (GEU) specifically designed for HIRDLS requirements.

2.3.3.1.6   Detectors, cryogenic cooler and signal processing.   The modulated atmospheric radiation and unmodulated background radiation emitted within the instrument is detected by 21 separate HgCdTe photoconductive detectors. The detector subsystem (DSS) contains the focal plane and vacuum dewar. The detectors and cold filters are cooled by a Stirling cycle cryocooler (CSS) operating near 60 K and controlled by the cooler electronics unit (CEU). The detector signals are ac-coupled to remove constant or slowly varying background signals before being amplified by low-noise preamplifiers. The amplified ac signal is passed through an analog bandpass filter with a bandwidth somewhat greater than two times the expected signal bandwidth and centered about the fundamental component of the chopping frequency to prevent aliasing of higher or lower frequency components into the signal band. The filtered signal is demodulated by sampling the waveform synchronously with the chopping frequency. The signal is digitized using a 16-bit analog-to-digital converter. A programmable lowpass digital filter for each channel allows the performance of the signal processing system to be optimized in orbit and minimizes sensitivity to drift or changes in electrical component values. After digital lowpass filtering, the signal samples

Composite FOV Outline

Alignment
Quad Detector

ch 18 H_2O	ch 5 CO_2	ch 17 CH_4
6.97 to 7.22 μm	14.71 to 15.27 μm	7.30 to 7.55 μm
ch 19 Aerosol	ch 4 CO_2	ch 16 $ClONO_2$
7.06 to 7.13 μm	15.15 to 15.97 μm	7.70 to 7.82 μm
ch 20 H_2O	ch 3 CO_2	ch 15 N_2O
6.49 to 7.03 μm	15.63 to 16.39 μm	7.80 to 7.96 μm
ch 21 NO_2	ch 2 CO_2	ch 14 N_2O_5
6.12 to 6.32 μm	16.26 to 16.67 μm	7.94 to 8.14 μm
ch 12 O_3	ch 1 N_2O, Aero	ch 13 Aerosol
8.77 to 8.93 μm	17.01 to 17.76 μm	8.20 to 8.33 μm
ch 11 O_3	ch 6 Aerosol	ch 7 CFC-11
9.54 to 9.89 μm	11.96 to 12.18 μm	11.72 to 11.98 μm
ch 10 O_3	ch 9 CFC-12	ch 8 HNO_3
9.90 to 10.10 μm	10.72 to 10.93 μm	11.05 to 11.63 μm

736 μm
9.0 km
2.98 mrad

2.9 mm

81.8 μm
1.0 km
0.332 mrad

Space

Earth

4.50 mm
55.0 km
18.2 mrad

1.39mm
17.0 km
5.63 mrad

0.65 mm
8.0 km
2.65 mrad

818 μm
10.0 km
3.32 mrad

4.50 mm
55.0 km
18.2 mrad

Figure 2: Schematic diagram of the HIRDLS focal plane array.

are decimated by a factor of 6 to a final effective sampling rate of nominally 83.3 Hz before being output to the telemetry stream.

2.3.3.1.7   Instrument control.   The instrument control and onboard data processing functions are performed by a flexible on-board microprocessor, referred to as the instrument processing unit (IPU), which can be programmed from the ground. In particular, the IPU controls the GMU via the gyro electronics unit, and similarly the mechanical chopper and scan mirror commands through the telescope electronics unit (TEU).

2.3.4   HIRDLS Observing Modes

The HIRDLS instrument is designed to be versatile in its ability to scan the line-of-sight in both vertical (elevation) and horizontal (azimuth) directions. As such, the LOS azimuth position, elevation scan rate and range, can be commanded individually. A number of standard scan patterns, referred to as observing modes, are currently envisaged and are designed to address a range of science investigations; these standard modes will be described briefly in this section. In addition to the standard modes, other viewing modes not currently planned can be developed in response to special geophysical events or as part of special engineering testing. There is a strong desire to provide, as much as possible, observational data that is spatially and temporally uniform over the life of the HIRDLS mission. The primary observing modes provide broad, contiguous global coverage.

2.3.4.1   Global Observing Mode.   This mode is envisaged as the normal mode for scientific data collection. In this mode, there will be 6 vertical scans separated by $5°$ in the across-track direction (i.e. nominally in the longitudinal direction) and $5°$ along the satellite track (i.e. latitudinal direction). Each vertical scan will cover about $3°$ in elevation and be completed in 10 seconds. The entire azimuth swath will be completed in approximately 66 seconds, covering a range of LOS azimuth angles from $-21°$ to $43°$. In-flight radiometric calibration will be performed by viewing cold space above the atmospheric limb signal every elevation scan and by viewing an internal warm blackbody calibration source after every complete swath. The interval between blackbody views may be increased if warranted by in-flight experience. A consequence of equal angular spacing of profiles is the progressively closer horizontal spacing of profiles in the longitudinal direction as the spacecraft moves toward the poles.

2.3.4.2   Alternative Global Observing Mode.   This mode provides vertical profiles with a fixed horizontal distance of 500 km between profiles in the across-track direction and 500 km in the along-track direction.

2.3.4.3   Fine Horizontal Spacing Modes.   The Medium Resolution observing mode, with a profile spacing of approximately $2.5° \times 2°$, and the High Resolution observing mode, with a spacing of $1° \times 1°$, provide finer horizontal spacing of profiles, but do not provide contiguous coverage from orbit to orbit. These modes are desirable for observing limited geographic features such as the polar vortex boundaries or rapidly changing concentrations of certain photochemically active species along the day-night terminator. In the Medium Resolution mode, the in-flight calibration target is viewed after every other azimuth swath maintaining the 66 second calibration period; this mode produces 4 vertical profiles per swath, each profile scan taking about 6 sec to be completed. In the High resolution mode, there will be 2 vertical scans per swath and 3 swaths between views of the in-flight calibrator.

2.3.4.4   Additional Observing Modes.   These include the Gravity Wave mode intended to provide data at the highest possible vertical resolution for studies of gravity waves. This is achieved by viewing at a fixed azimuth angle along the orbit track and vertically scanning at the slowest rate. The stratospheric and tropospheric (STE) observing mode is intended for observing the upper troposphere and lower stratosphere with high horizontal and vertical spatial resolution, and high signal to noise. This is accomplished by a combination of three "short" vertical scans spanning only the altitude range of interest and a "long" scan that will include observations to high altitudes and a view of cold space for zero correction. Finally, a Selected Targets mode will allow viewing certain fixed geographic locations for such targets as volcanic eruptions, formation of polar stratospheric clouds, and over ground sites to facilitate comparisons with correlative data.

2.4 HIRDLS Sounding Channels

The selection of channel spectral passbands for a radiometer is based on several considerations, which are sometimes competing. At least one channel is required for each trace gas that will be measured. In an ideal situation, the spectral passband would be situated over the strongest emission band of the gas being studied and should be sufficiently narrow to exclude the contaminating signal from other gases. In practice, the situation is usually more complicated. For several species, there is only one measurable infrared spectral feature. This may be relatively weak, and the primary consideration is then the ratio of limb emission signal to instrument noise. In making the channel passband wide enough to obtain sufficient signal, it often overlaps the emission bands of other species which then give a contaminating signal. This effect can be minimized by prudently choosing the passband boundaries to avoid the stronger contaminating spectral features. It is also necessary to have a separate channel for the independent measurement of the contaminating gas, especially if the gas is a strong emitter with a variable distribution. This channel is usually in a different part of the infrared spectrum where the gas has its strongest emitting band.

If the atmosphere along the limb path above the tangent height is not optically thick, the weighting functions are strongly peaked in the region of the tangent point. This allows good vertical resolution to be obtained in the profile retrievals. For abundant gases such as H_2O, CO_2, and O_3 which have very strong emission bands, it is possible to use several channels which make use of the varying optical depth over the band profile to selectively emphasize different altitude regions of the atmosphere. In this way, a channel situated in a spectral region of lower optical depth can be chosen such that the channel weighting functions peak in the lower atmosphere. This usually falls on the shoulder of a strong band. The atmospheric opacity, either due to gaseous or particulate absorption alone, or in the presence of optically thick clouds, determines the lower limit of the retrieval [*Gille and House* (1971)].

The weighting functions of a channel that straddles the high optical depth spectral region of the band center will peak in the upper atmosphere. Measurements can be made up to the altitude at which the signal-to-noise ratio of the measurements becomes too low to provide useful information. Depending on the gas and the spectral band, the limb emission from these channels can show non-local thermodynamic equilibrium (non-LTE) emission for tangent heights at high altitudes. The retrieval of gas abundance from such measurements requires the treatment of non-LTE processes.

Window channels in spectral regions of low gaseous absorption are also required to measure aerosol opacity. This allows aerosol extinction profiles to be calculated, and corrections to be made for aerosol absorption in the other trace gas channels. By including aerosol channels at several positions throughout the infrared spectrum being used, these corrections can more readily take into account the spectral variation of the aerosol absorption.

For very important measurements, such as those of temperature and O_3, a degree of redundancy is desirable in the system so that there is a backup in the event of a channel failure. For this reason, HIRDLS uses a total of four CO_2 channels. Two channels is the minimum requirement for temperature retrieval in the stratosphere and mesosphere.

Table 3 summarizes the HIRDLS sounding channels in terms of the targets and contaminants for each channel.

2.4.1 Spectral Modeling

In this section we outline some of the general considerations important in choosing channel spectral passbands. This is followed by sections describing the particular cases of each of the 21 HIRDLS channels. The specifications for the filter 50 % response points are defined in Table 2 along with the altitude range where they are expected to yield useful retrievals. The filter spectral responses used were obtained from the Infrared Multilayer Laboratory at the University of Reading. Radiometers such as HIRDLS measure the integrated spectral radiance over a channel passband of typically 10–50 cm^{-1}. Compared with the measurement of a high-resolution spectrometer, where the spectral resolution is usually in the range 0.01–0.005 cm^{-1}, the radiometer has an advantage in that it is not particularly sensitive to the fine spectral detail of a given line. However, the technique will only work if the spectroscopy is well understood and if all major sources of emission have been identified.

The calculations presented in this section were performed using the general line-by-line atmospheric transmittance and radiance model GENLN2 [*Edwards* (1992)]. This algorithm assumes a multi-layered atmosphere of mixed gases, and has been designed for speed of computation.

Gas	Channel / Target Gas																				
	Aerosol	(T,p)	(T,p)	(T,p)	(T,p)	Aerosol	CFC11	HNO_3	CFC12	O_3	O_3	O_3	Aerosol	N_2O_5	N_2O	$ClONO_2$	CH_4	H_2O	Aerosol	H_2O	NO_2
	1	2	3	4	5	6	7	8	9	10	11	12	13	14	15	16	17	18	19	20	21
CO_2	▨	■	■	■	■	▨	▨		▨		▨		▨	▒		▒	▨				
Aerosol	■					■	▨	▒	▨			▒	■	▨	▒	▒	▒		■	▒	▒
O_3		▨	▨	▨	▨	▨			■	■	■	■	▨					▨			
H_2O	▨					▨	▨	▨			▨		▨		▨	▨	▨	■	▨	■	▨
NO_2																					■
CFC11							■	▨													
HNO_3							▨	■	▨				▨		▨	▨					
CFC12							▨	■				▨									
N_2O_5														■							
N_2O	▨	▨											▨	▨	■	▨	▨				
$ClONO_2$															▨	■					
CH_4													▨	▨		▨		■	▨	▨	▨	▨
CF_4													▨	▨							
O_2																		▨		▨	▨

Table 3: Identification of the target gases (black), and the strong (dark grey) and minor (light grey) contaminants in the HIRDLS sounding channels.

An equinox mid-latitude model atmosphere (March 21, 40°N) was constructed using the Upper Atmosphere Research Satellite (UARS) standard climatology [*Seals et al.*(1991)]. This was supplemented with an aerosol profile taken at the University of Wyoming on 1 May 1991, four months before the Mount Pinatubo eruption [*Deshler et al.*(1993)]. A background aerosol loading was considered the most relevant for this study since the very high aerosol turbidity encountered after the Pinatubo eruption represents a large perturbation from normal conditions. For the high-altitude studies, the decrease in the CO_2 mixing ratio in the thermosphere was included using a mean profile from rocket measurements [*López-Puertas et al.*(1992)]. Calculations are presented for limb view tangent heights above 10 km, with the upper limit of the measurement range depending on the channel. The atmospheric layering was chosen so that the variation of temperature and Voigt spectral line half width across a layer were kept within specified limits. This resulted in narrow layers, of vertical width 0.1 km near the tangent point, such that the calculated limb radiances are not sensitive to the forward model layer structure. A ray tracing algorithm was used to describe the limb viewing geometry and atmospheric refraction was included. Curtis-Godson mean values for pressure, temperature, and absorber amount were calculated within each narrow layer.

Local thermodynamic equilibrium (LTE) has been assumed for most calculations. However, we discuss the non-LTE effects at high altitudes in the channels covering the 15 μm band of CO_2 [*Edwards et al.*(1993)], and in the 9–11 μm bands of O_3 [*Edwards et al.*(1994)]. A study is also planned to investigate the effect in the high-altitude H_2O channel at 6.3 μm [*Kerridge et al.*(1989)].

The following sections describe the purpose and special considerations for each of the 21 HIRDLS channels listed in Table 2. The channels are dealt with in order of channel number, with the exception of the aerosol channels, which are discussed together.

2.4.1.1 Channels 2–5: Temperature. HIRDLS will have four channels measuring CO_2 emission for retrieval of temperature and pressure. The positions of the channels are shown in Figure 3 along with the limb radiance from each of the principal emitting gases. The weighting functions for the temperature sounding channels are shown in Figure 23.

Channel 2 is intended to measure CO_2 emission from tangent points at low altitudes to provide information for
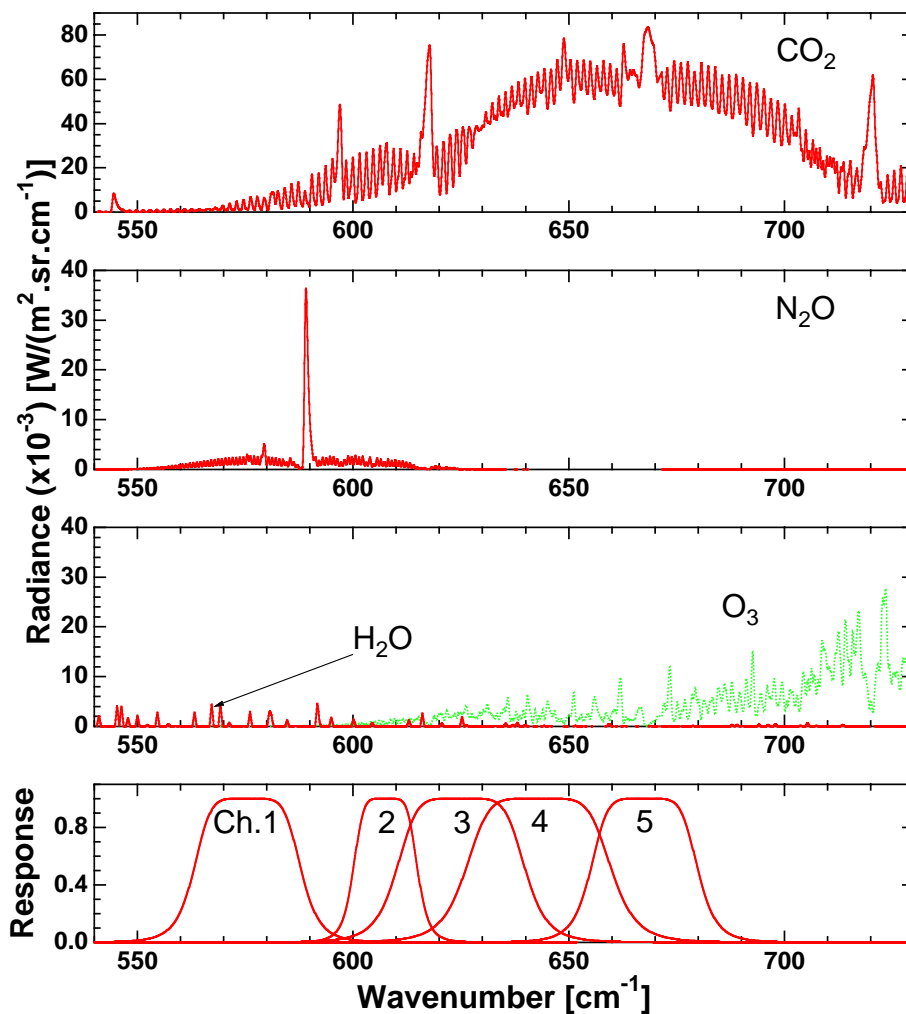
Figure 3: Limb radiance spectra for HIRDLS channels 1–5 calculated for a tangent height of 25 km, 21 March, 40°N. The spectral resolution is 0.5 cm^{-1}.

the temperature retrieval down to 8 km. For this reason, the channel is situated on the side of the main CO_2 band where the optical depth is lower. This allows radiation to reach the satellite from lower in the atmosphere without being reabsorbed as it traverses higher layers. The primary gaseous contaminating signal comes from N_2O. This channel sits in a region between the strong CO_2 *Q*-branches at 597 and 618 cm^{-1} which are purposely avoided to keep the limb optical depth low.

Channels 3 and 4 both measure CO_2 emission from mid-altitude tangent points, and as such provide some redundancy in the system for this very important measurement, which is desirable in the event of a channel failure. However, taken together, the two measurements add extra sensitivity to the retrieval. Channel 4 is positioned on the low frequency side of the main 15-μm CO_2 band, a spectral region of higher opacity than that of Channel 3. As a result, the peaks of the weighting functions for this channel are largest at around 30 km, compared with 23 km in the case of Channel 3 (Figure 23).

Channel 5 is the high-altitude temperature sounding channel. The maxima of the weighting functions peak at about 36 km. This channel is located over the peak of the strong $^{12}C^{16}O_2$ *Q-branch* at 667 cm^{-1}. Because of the high optical depth of the atmosphere in this spectral region, radiation from below about 27 km does not contribute significantly to the measured signal (Figure 23).

The CO_2 Channels 3, 4, and 5 all have very large signals due to the high opacity of the CO_2 bands. This allows measurements to be taken to high altitude. We assume that useful radiance measurements may be obtained up to the tangent height where the limb radiance is equal to the noise equivalent radiance (NER) for a single measurement. These altitudes are 80, 90, 110, and 125 km in Channels 2, 3, 4, and 5, respectively, although retrievals to these levels would not necessarily be part of the operational specification. (The NER values quoted in this paper assume an effective measurement bandwidth of 7.5 Hz, which is the nominal bandwidth for the global mode). At high altitudes, non-LTE effects in the 15-μm bands of CO_2 have been shown to be an important consideration for limb viewing radiometers at tangent heights greater than 70 km [*Edwards et al.*(1993)]. The departure of a given band radiance from LTE values for a particular limb view tangent height and day–night differences follow the divergence of the upper state vibrational temperature profile from the kinetic temperature. Channels 2 through 5 show a departure from LTE above 70 km. The magnitude of any diurnal variation depends on the relative contribution of the 15 μm ν_2 hot bands to the channel radiance since their state populations are affected by solar absorption by CO_2 at 2.7 and 4.3 μm. This is greater for the low wavenumber channels that include radiation from the first hot band centered at 617 cm^{-1}. The inclusion of non-LTE effects in the modeling is also important for determining the tangent height that can be considered to be effectively a space view since this is needed for calibration purposes. This has been defined at the $\frac{1}{10}$ NER radiance level. These altitudes are 95, 125, 140, and 150 km, in Channels 2, 3, 4, and 5, respectively, and are lower than would be calculated under LTE conditions because the non-LTE limb emission does not follow the sharp rise of the kinetic temperature in the thermosphere.

2.4.1.2   Channel 7: CFC11; Channel 8: HNO_3; Channel 9: CFC12.   The measurement of CFC11 using limb emission has proved difficult in the past due to its relatively low signal. The band centered at 848 cm^{-1} provides perhaps the best candidate region because of relatively low contamination from other gases compared to bands in other spectral regions. The measurement does, however, require good knowledge of the spectroscopy governing the contaminating signal from HNO_3, and the line parameters for the hot bands in the low frequency wing of this feature, Figure 4, are not well-known. The aerosol emission, with its broad-band nature, is also a problem in the lower stratosphere. The CFC11 bands themselves have not been resolved into individual spectral lines by laboratory measurements, and are included in the model calculations using absorption cross-sections measured in the laboratory at a set of 6 different temperatures. This leaves some doubt as to the exact pressure and temperature variation of the absorption coefficient across the band, because the physics of pressure broadening of each line cannot be included explicitly. This, along with the fact that the band has a smooth emission profile, without features to provide good spectral contrast, has made CFC11 retrieval from measurements made by the Cryogenic Limb Array Etalon Spectrometer (CLAES) on the UARS platform very difficult [*Roche et al.*(1993), *Grose et al.*(1994)].

HIRDLS Channel 7 will be used to measure CFC11. The passband has been chosen to cover the whole band therefore maximizing the available signal. Even so, the CFC11 signal falls to the channel NER value for tangent heights around 30 km. Minor gaseous contaminants in this spectral region include H_2O, CO_2, and O_3. The main concern, as mentioned above, is the contaminating signal from HNO_3, and this tightly constrains the upper boundary of the passband. The lower boundary, which overlaps the aerosol Channel 6, is not so critical.
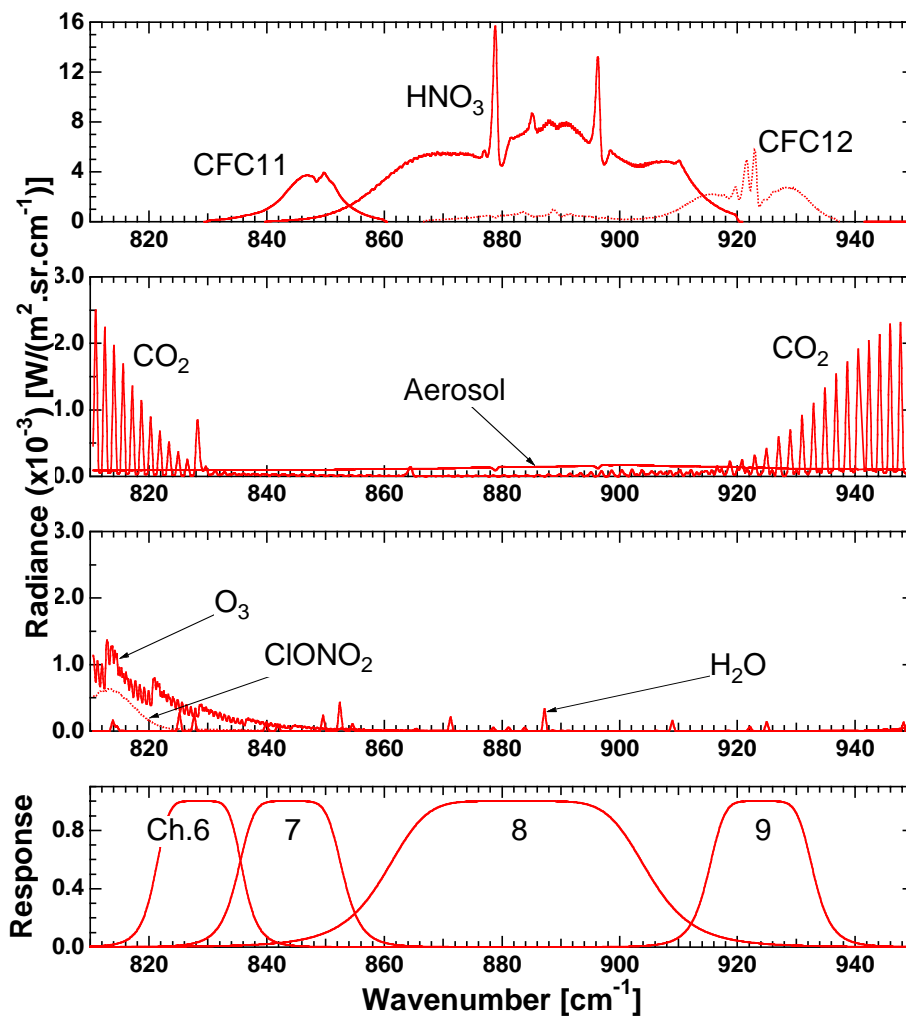
Figure 4: Limb radiance spectra for HIRDLS channels 6–9 calculated for a tangent height of 25 km, 21 March, $40°N$. The spectral resolution is 0.5 cm^{-1}.

Channel 8 will be used to measure HNO_3. This has a relatively wide passband and covers the emission from the strong ν_5 and $2\nu_9$ bands. This is a relatively clean channel. Primary gaseous contaminants are CFC11 and CFC12 on the low and high frequency sides, respectively, of the channel passband. Retrievals of HNO_3 should be possible to an altitude of about 40 km.

CFC12 will be measured in Channel 9. The emission from this gas falls to the value of the channel NER at an altitude of about 35 km. Below this altitude, the main contaminating signal comes from HNO_3 and the lower passband boundary is carefully placed to capture the signal from the CFC12 922 cm^{-1} Q-branch whilst avoiding the main part of the HNO_3 band. If the channel were widened on the high-frequency side, CO_2 contamination would be increased, and above 35 km nearly all the channel signal comes from the CO_2 laser band. The emission from this band is strongly influenced by non-LTE processes due to solar absorption by CO_2 at 4.3 μm and a large daytime enhancement will be seen above 55 km [*Edwards et al.*(1994)]. There exists the possibility of indirectly studying these processes using high-altitude radiance measurements in this channel.

2.4.1.3 Channels 10–12: O_3. HIRDLS will have three O_3 channels in the 9–11 μm spectral region. Channels 10 and 12 cover spectral regions of relatively low optical depth over the O_3 ν_3 hot bands and ν_1 fundamental bands, respectively, as shown in Figure 5. These will measure O_3 abundance in the lower atmosphere, primarily
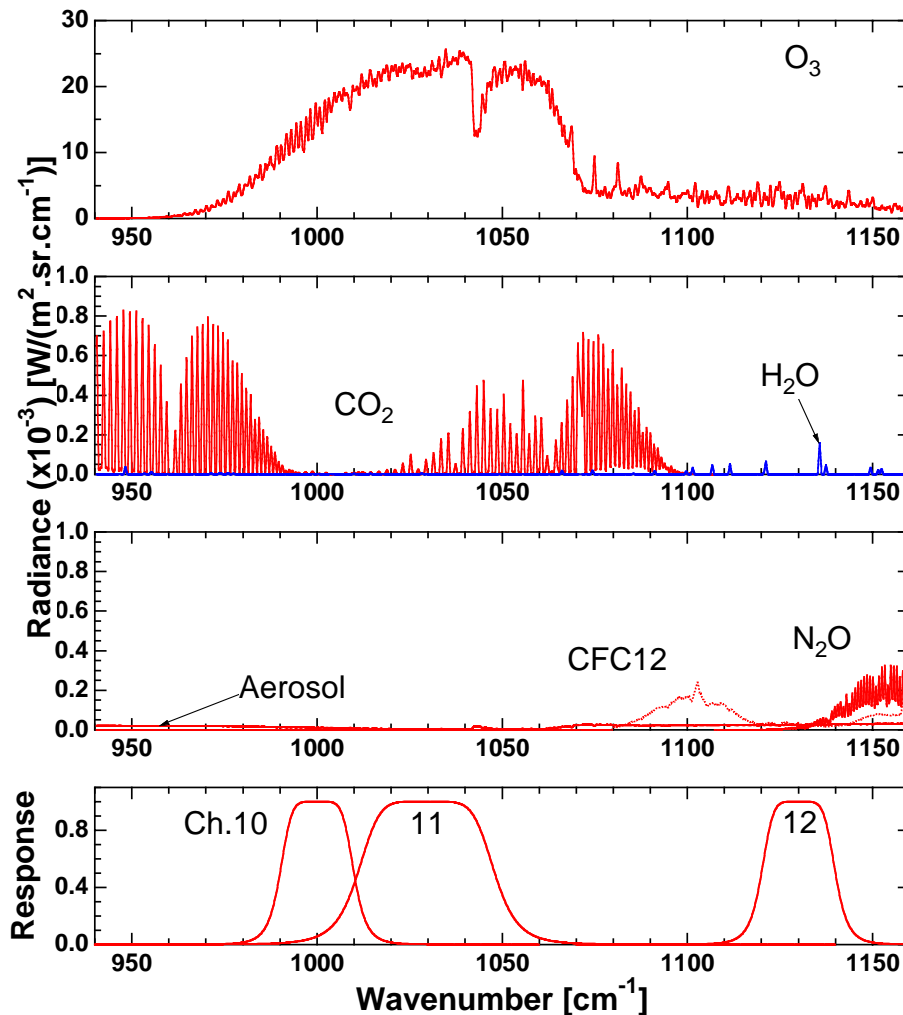
Figure 5: Limb radiance spectra for HIRDLS channels 10–12 calculated for a tangent height of 25 km, 21 March, 40°N. The spectral resolution is 0.5 cm^{-1}.

in the 10–30 km altitude range. Used together, these channels provide extra sensitivity for this measurement since the Channel 12 weighting functions peak at 5 km below those of Channel 10 (Figure 27). Having two channels from which a low altitude O_3 retrieval can be made also allows for a degree of redundancy in the system. The primary contaminating signal in Channel 10 comes from the CO_2 (00011–10002) fluorescent band. The primary contaminants in Channel 12 are N_2O and CFC12 on the high and low wavenumber sides, respectively. At low altitudes, H_2O and aerosol must be considered. Channel 11 covers the strong band center of the ν_3 fundamental. Because of the greater optical depth in this spectral region, the weighting functions peak higher in the atmosphere at the altitude of the O_3 layer above 30 km. Measurements are also possible to higher altitudes. Below about 70 km there is only minor contamination from the CO_2 (00011–10001) fluorescent band.

The primary goal of all three O_3 channels is the retrieval of the O_3 profile from the upper troposphere into the mesosphere. Over this altitude range, the tangent height sensitivity of the Channel 10 and 11 weighting functions is not affected greatly by small changes in the passband positions or widths. However, studies have shown [*Edwards et al.*(1994)] that the positioning is very important if an O_3 retrieval above 70 km is to be made. The selection of the Channel 10 and 11 spectral passbands was therefore optimized for high-altitude studies with the constraint that the stratospheric performance be in no way compromised.

Given the band-dependent nature of non-LTE processes, modeling the high-altitude signal in a particular channel is simplified considerably if the radiance from only one band, or set of bands with similar non-LTE behavior, dominate. In this spectral region, the O_3 ν_3 fundamental, hot, and combination bands all show enhanced non-LTE emission above 70 km. There is also a large diurnal radiance variation due to increase in O_3 concentration at night in the absence of photolysis, and the primary non-LTE processes are also different. The CO_2 daytime radiance from the two fluorescent bands shows a very large departure from LTE above 65 km due to solar absorption in the CO_2 4.3-μm band. These processes are described in detail in Edwards *et al.*(1994).

The daytime limb radiance calculated using the non-LTE model described in Edwards et al. was used in the passband selection of Channel 10 with the condition that the total signal be greater than $\frac{1}{4}$ NER for tangent heights below 90 km. Assuming that several profiles can be averaged together, useful measurements might be made at this radiance level. This passband choice keeps the CO_2 radiance to a minimum whilst also minimizing the contribution of the O_3 ν_3 fundamental relative to the other O_3 bands. Most of the signal comes from the O_3 ν_3 hot and combinational bands which show non-LTE daytime radiance enhancements due to chemical pumping of the ν_3 excited states, and there is a large difference between the non-LTE and LTE total radiances for tangent heights above about 65 km. At night, the relative contribution of the O_3 ν_3 fundamental band increases as radiative pumping of the O_3 (001) state becomes more important. The total signal level increases relative to the day and the total radiance eventually falls to $\frac{1}{4}$NER at 95 km. Above 85 km, the radiance from the other O_3 bands remains essentially the same as during the day due to the diurnal invariance of the atomic oxygen concentration and O_3 recombination rate at these altitudes. For lower tangent heights, between 70 and 85 km, the atomic oxygen concentration falls at night resulting in less recombination and chemical pumping and a lower limb radiance from these bands. Channel 10 can be used to study non-LTE hot band processes. Depending on how well these can be modeled, Channel 10 radiances could also help in the retrieval of high altitude O_3 when using the ν_3 fundamental band signal in Channel 11 where the hot and combination bands provide the major contaminating signal.

The Channel 11 passband spans the low frequency branch of the O_3 ν_3 fundamental band, emission from which provides the main contribution to the signal at all tangent heights. This helps the forward modeling for retrieval purposes, since the non-LTE processes of the (001) state alone are the most important. There is significant departure from LTE for tangent heights above 70 km which is mainly due to radiative pumping of the (001) state after absorption of upwelling radiation. Contaminating signals are also present from the O_3 ν_3 hot, combination, and ν_1 fundamental bands, along with the CO_2 laser band. The passband choice minimizes the CO_2 contribution whilst maximizing total signal. Because the CO_2 amount is reasonably well known, it should be possible to account for emission using the non-LTE model. The measurements of the weaker O_3 bands in Channel 10 may help to characterize their non-LTE emission in this channel. During the day, the signal falls to $\frac{1}{4}$NER for a tangent height of 95 km. At night, the concentration of ground state O_3 increases throughout the mesosphere and thermosphere in the absence of photolysis. Radiative pumping of the (001) state is greater than during the day, and results in a greater nighttime limb emission. At all tangent heights, the O_3 ν_3 fundamental band is the only significant contributor to the signal which falls to $\frac{1}{4}$NER at a tangent height of 100 km.

2.4.1.4 Channel 14: N_2O_5; Channel 15: N_2O; Channel 16: ClONO$_2$; Channel 17: CH$_4$. The spectral region between 1200 and 1400 cm^{-1} contains the emission features of several trace gases of interest in atmospheric chemistry. It is also a region of overlapping bands where several gases contribute significantly to the total channel signals as is shown in Figure 6. This makes channel selection more complicated, and channels must be treated as
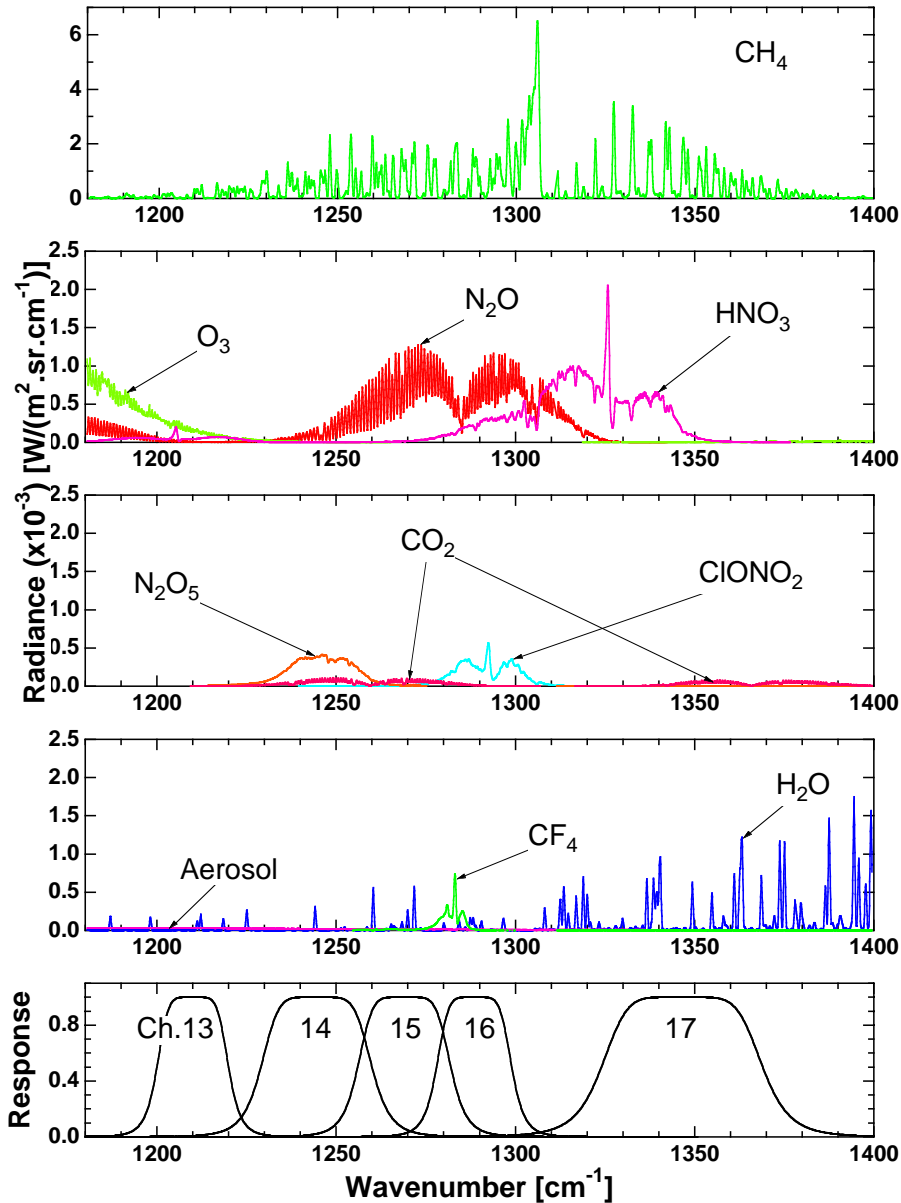
Figure 6: Limb radiance spectra for HIRDLS channels 13–17 calculated for a tangent height of 25 km, 21 March, 40°N. The spectral resolution is 0.5 cm^{-1}.

interdependent. The method used to simultaneously optimize the spectral passbands of interdependent channels is described in Edwards *et al.*(1995). This consists of maximizing the sensitivity of the channel signal to changes in the concentration of the primary gas being measured in the particular channel. Choosing several channels in each of which a particular gas contributes significantly compared to its neighbors, allows for the simultaneous retrieval of gas concentrations using all the channels.

Channel 14 for measuring N_2O_5 is to be centered on the ν_{12} band. Because the signal is rather weak, this

channel is wide enough to cover the whole band. The major contaminants, in order of importance, are CH_4 and N_2O at all altitudes, H_2O and CO_2 at low altitudes. Channel 15 for measuring N_2O is centered over the *P*-branch of the ν_1 transition. The major contaminants are CH_4 at all altitudes, HNO_3 and $ClONO_2$ at higher altitudes, H_2O and CO_2 at low altitudes. Channel 16 for measuring $ClONO_2$ will to be centered over the ν_2 band. Major contaminants are N_2O, CH_4, and HNO_3. Channel 17 for measuring CH_4 is located in the short wavelength part of the ν_4 band. The major contaminants are N_2O, HNO_3, and H_2O.

The wavenumber bounds of the N_2O Channel 15 and the CH_4 Channel 17 were optimized simultaneously to achieve maximum sensitivity to the target gases. Both Channels 15 for N_2O and 17 for CH_4 have signal contamination from other gases. In the case of Channel 15 for N_2O, the main contaminants that must be included besides CH_4, are HNO_3 and $ClONO_2$. In Channel 17 for CH_4, the signal contamination is due to HNO_3 and H_2O.

Having fixed the wavenumber bounds of Channels 15 for N_2O and 17 for CH_4, the wavenumber bounds of the N_2O_5 and $ClONO_2$ channels were obtained. The optimization for these channels was performed for a tangent height of 30 km and solar zenith angle of $30°$. This is the altitude region where these species have their largest mixing ratios and where the measurements have greatest significance. In the case of Channel 14 for N_2O_5, the channel contaminants are N_2O and CH_4. A similar procedure was followed for $ClONO_2$ in Channel 16. The contaminants in the channel are N_2O, CH_4, and HNO_3. In both cases, the channel wavenumber bounds were chosen so as to minimize the fractional uncertainty in the gas amounts. The selected Channel 14 passband avoids unnecessary CH_4 contamination at the lower boundary and N_2O contamination at the upper boundary whilst maximizing the N_2O_5 signal component. The Channel 16 passband lower boundary avoids the low frequency branch of the N_2O band, and the upper boundary avoids the peak of the CH_4 band. Retrievals of both these gases should be possible to 40 km or higher.

2.4.1.5   Channels 18 and 20: H_2O; Channel 21 NO_2. HIRDLS will measure water vapor using two channels in the 6.3-μm ν_2 band. The low altitude H_2O Channel 18 is situated in a spectral region of relatively low optical depth, as shown in Figure 7. The weighting function peaks are largest at about 12 km, although useful profile information should be obtained down to about 8 km. The primary contaminants in this channel are CH_4 at all altitudes and the O_2 pressure induced continuum at low altitudes, with minor contamination coming from CO_2. The edge of the CH_4 band constrains the lower boundary of the passband, and if the upper boundary is moved higher there is a greater O_2 contribution at lower altitudes which is undesirable for this low altitude channel.

The high altitude H_2O Channel 20 is a wide channel covering a large part of the band. As such, it has a high optical depth and the weighting functions peak at 15 km and show good response for tangent heights through the lower stratosphere. The primary contaminants are the pressure induced O_2 continuum for tangent height limb views up to about 20 km, and CH_4 at higher altitudes. The passband boundaries are not tightly constrained within a few wavenumbers, and the channel passband has been optimized along with the NO_2 Channel 21 using the method described in the previous section.

The shortest wavelength HIRDLS channel covers the NO_2 ν_3 band at 6.2-μm. The channel passband has been optimized to maximize the NO_2 signal with respect to H_2O contamination using the Channel 20 signal. Contamination by signals from CH_4 and the O_2 continuum have also been considered. The channel is wide enough to include most of the NO_2 signal whilst avoiding the strong H_2O lines on either side. Non-LTE daytime H_2O and NO_2 enhanced emission will probably be a consideration in Channels 20 and 21 for tangent heights above 65 km as reported in Kerridge and Remsberg (1989).

2.4.1.6   Channels 1, 6, 13, and 19: Aerosol. Channels of low molecular absorption optical depth are required to measure aerosol extinction. Because low molecular opacity is required in an aerosol channel, they have relatively narrow spectral passbands in order to avoid molecular emission features. Channel 1 will be used for aerosol retrieval and also be used for a secondary retrieval of N_2O. The primary contaminants are H_2O and CO_2, and the lower passband boundary sits above some strong H_2O lines, Figure 3, which must be avoided if the low altitude aerosol retrieval is not to be affected. If the top boundary is moved higher, a strong N_2O line is included along with increased CO_2 contamination. This would affect the retrieval of high altitude aerosol.

Channel 6 lies just below the CFC11 Channel 7 (Figure 4). The primary contaminants are CO_2, O_3, and H_2O. The bottom boundary is set to avoid increased contamination from O_3 and CO_2 at higher altitudes. The primary
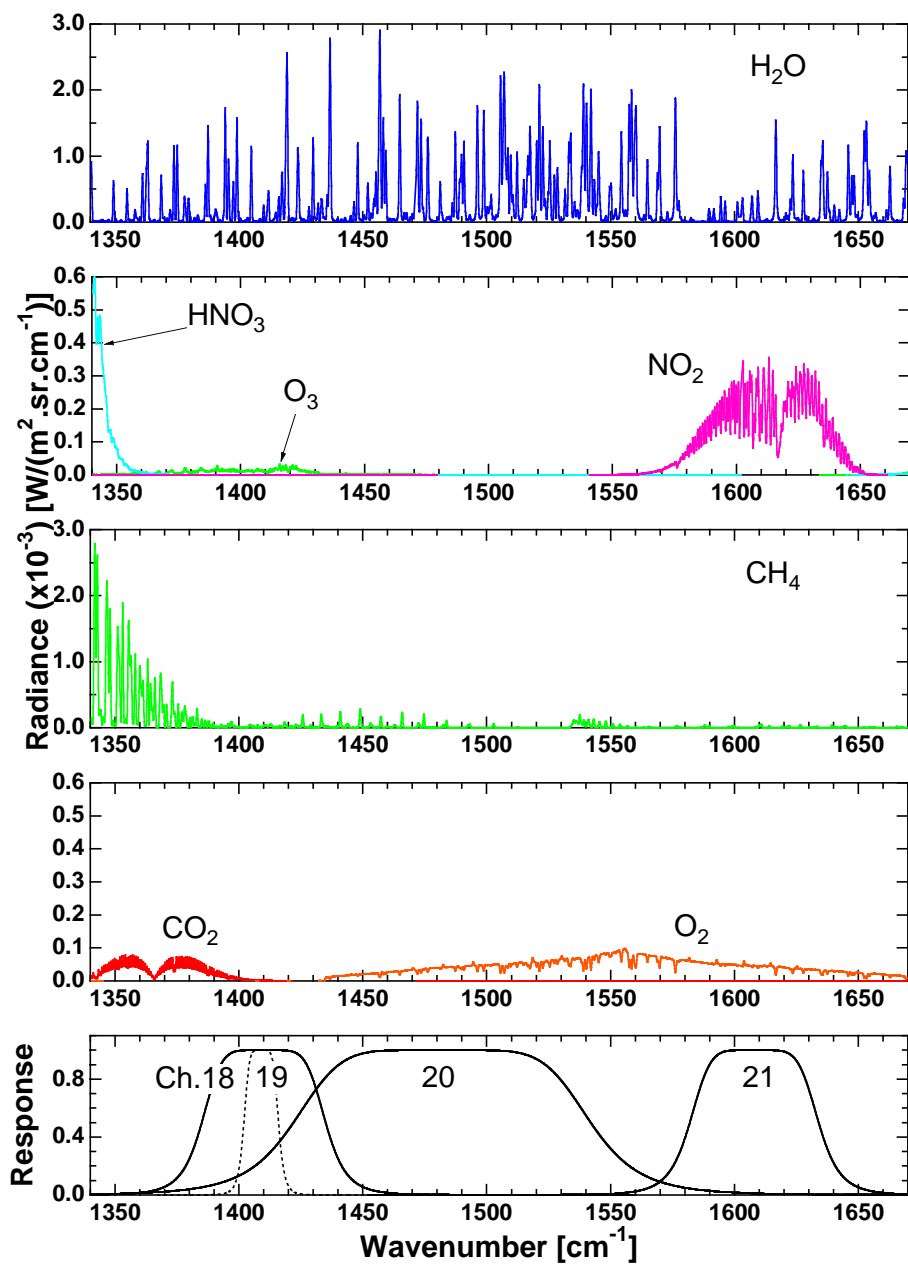
Figure 7: Limb radiance spectra for HIRDLS channels 18–21 calculated for a tangent height of 25 km, 21 March, 40°N. The spectral resolution is 0.5 cm^{-1}.

contaminants of Channel 13 (Figure 6), are CH_4, CO_2, N_2O, H_2O, and HNO_3. The lower boundary is set just above the N_2O band which, if included, would become a major contaminant at low altitudes. The top boundary is set to avoid strong CH_4 lines at higher frequency. This channel is heavily contaminated at low altitudes but relatively clean above 20 km. Channel 19 is a narrow channel that sits within the passband of the low altitude H_2O Channel 18 (Figure 7). The passband boundaries are set within a relatively clean micro-window amongst the H_2O lines. The channel is heavily contaminated by H_2O below 15 km.

2.5 Treatment of Aerosols, Polar Stratospheric Clouds, and Cirrus

The presence of aerosols and clouds causes interfering effects in the determination of the gaseous atmospheric chemical composition inferred from HIRDLS data. However, in addition to correcting for channel contamination useful information will be obtained on the nature of atmospheric aerosols. In this section we consider the three main types of atmospheric aerosol relevant to the HIRDLS observations; sulfate (H_2SO_4/H_2O) aerosols, polar stratospheric clouds, and cirrus clouds.

2.5.1 Aerosol Particle Types and Size Distributions

Aerosol particles make a significant contribution to the infrared opacity of the atmosphere, especially following major volcanic eruptions. The aerosol opacity has a gradually varying wavelength dependence in contrast to the very fine structure of molecular spectra and the spectrum is a function of several variables; particle composition (which determines the complex indices of refraction of the particle), particle size distribution, and particle shape (spherical, columnar, hexagonal, etc). Several types of aerosol are present in the altitude range of the HIRDLS observations.

Calculation of theoretical aerosol extinction spectra requires that the particle size distribution is represented either in tabular form, or as a parametric distribution, e.g. a lognormal distribution is a suitable form,

$$n(r) = \frac{N}{r\sqrt{2\pi}\ln\sigma_g}\exp\left[-\frac{\ln^2(r/r_g)}{2\ln^2\sigma_g}\right] \tag{1}$$

where N is the number of particles per unit volume, r_g is the median radius and σ_g is the distribution standard deviation. The effective particle radius is defined as a weighted mean

$$r_e = \frac{\int_0^\infty r^3 n(r)\,dr}{\int_0^\infty r^2 n(r)\,dr} \tag{2}$$

Examples of log-normal size distributions are those of the H_2SO_4/H_2O aerosols obtained from in situ measurements over Laramie, Wyoming [*Deshler et al.*(1993)] and examples of tabulated PSC spectra are presented in Dye *et al.*(1992). The Dye et al. distributions were measured by the Forward Scattering Spectrometer Probe (FSSP-300) during the Airborne Arctic Stratospheric Experiment (AASE II).

For each particle type, a set of particle size distributions for a range of effective particle radius is specified. For example, H_2SO_4/H_2O sulfate aerosol size distributions (which span a large range of effective radii) are used to calculate theoretical spectra for different sets of refractive indices (i.e. as given by the H_2SO_4/H_2O weight percent value), to generate a set of sulfate spectra spanning the range normally encountered in the stratosphere. Size distributions of cirrus ice crystals of different effective radius and particle shape are also calculated, using the H_2O indices of refraction. Distributions for ternary droplets, and for NAT and NAD particles (nitric acid trihydrate and nitric acid dihydrate PSC particles) are used in similar calculations. The full ensemble of aerosol spectra are calculated in order to develop a set of spectra which spans the different types that will be encountered by the HIRDLS experiment.

2.5.1.1 Sulfate aerosol. Within the last fifteen years, there have been two major volcanic eruptions (El Chichon in 1982 and Mt Pinatubo in 1991. Large volcanic eruptions inject substantial amounts of sulfur dioxide and ash into the Earth's stratosphere. The SO_2 gas injected by a volcanic eruption is oxidized, and the products react with

water vapor to form sub-micron sized spherical drops on the time scale of 1 month [*Hamill et al.*(1997)]. The infrared opacity of the atmosphere following a volcanic eruption decreases with an e-folding time of 0.7 years [*Massie et al.*(1996)] and the sulfate aerosol distributions change markedly as a function of altitude and latitude [*Lambert et al.*(1993)]. Small amounts of H_2SO_4/H_2O aerosol are still present several years after a major eruption. Some volcanic contribution to the stratospheric aerosol loading is quite likely to occur during the time-frame of the HIRDLS measurements. Although the aerosol loading at the time of the HIRDLS measurements is unpredictable, we may use conditions determined from SAGE II, POAM II and UARS to evaluate the possible effects ranging from background to volcanic aerosol loadings. Note that UARS obtained information on background aerosols early in its mission (October 1991) before the Pinatubo cloud spread to high latitudes. Figure 8 shows a representative sulfate aerosol spectrum.
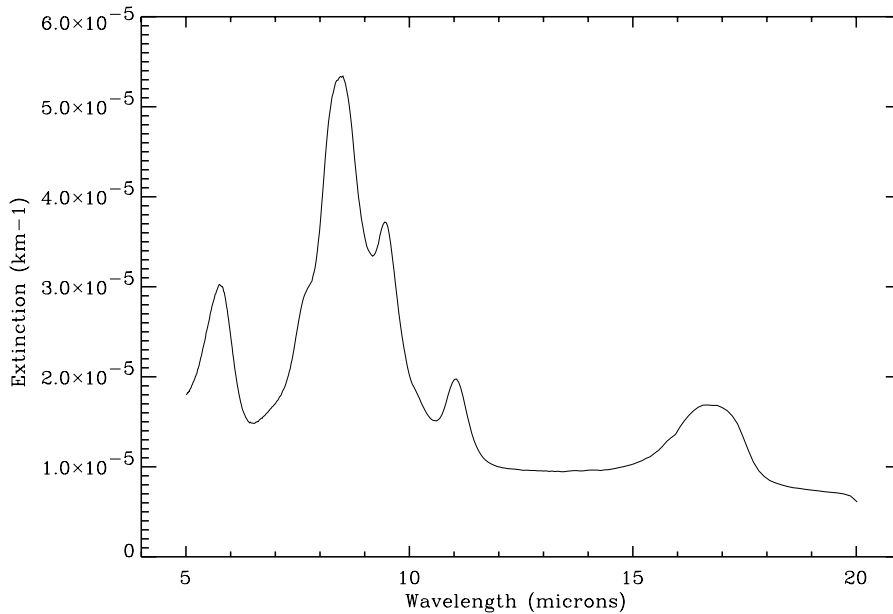
Figure 8: A representative sulfate aerosol spectrum calculated for a 50 % H_2SO_4 composition.

2.5.1.2 Polar stratospheric clouds. Polar stratospheric clouds (PSCs) are observed in the polar regions when temperatures approach and become less than 195 K [*McCormick et al.*(1982)]. The composition of PSCs is not yet predictable with confidence, both liquid and solid particle types have been detected using de-polarization studies of lidar soundings [*Browell et al.*(1990), *Gobbi et al.*(1998)]. Several composition types have been proposed and several types have been observed. At temperatures less than the ice frost point, PSC II (ice) particles are expected to form, whereas at higher temperatures near 195 K, nitric acid trihydrate (NAT) solid particles are thought to exist. Both PSC II and NAT particles are nonspherical. Figure 9 shows a representative NAT spectrum. Ternary solution ($H_2SO_4/H_2O/HNO_3$) spherical droplets have also been observed at temperatures between that of the NAT and PSC II temperature thresholds [*Carslaw et al.*(1994)].

2.5.1.3 Cirrus. Cirrus (water-ice) particles are observed at and below the tropopause [*Wang et al.*(1996)]. The distribution of the cirrus is confined to altitudes below the tropopause. Though the generation mechanisms for the cirrus are the subject of current theoretical modeling, they are frequently associated with the outflow regions of deep convective clouds [*Houze* (1993)].

The cirrus particles are of various shapes and sizes. Heymsfield (1986) measured ice particles in a cirriform cloud at 16 km altitude over the Marshall Islands (near the equator). Figures 3 and 4 of Heymsfield show photographs of sampled particles, and the particles are of various shapes (triangular, crosses, bullets, etc.). Macquhar
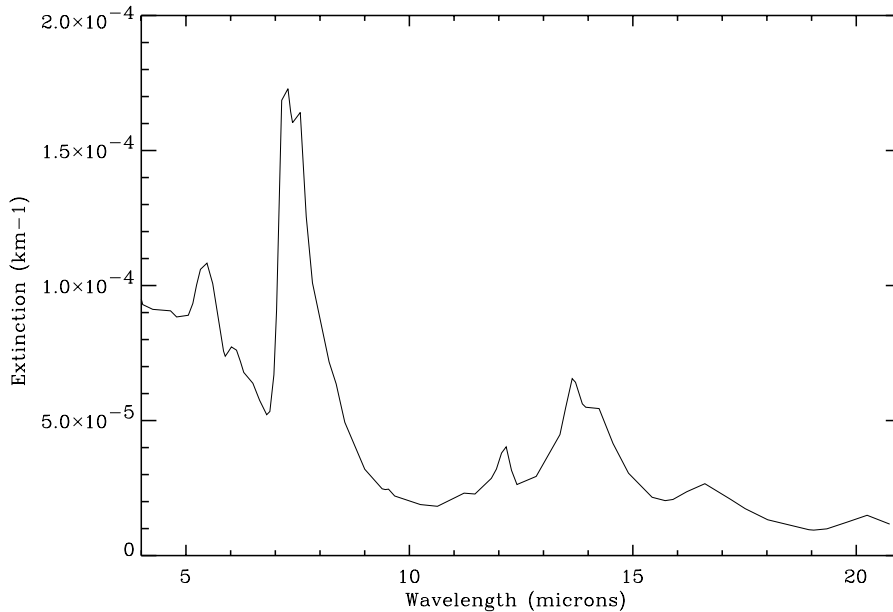
Figure 9: A representative NAT PSC spectrum calculated for an effective particle radius of 0.3 μm and ambient conditions determined from FSSP data obtained during the AASE II campaign [*Dye et al.*(1992)].

and Heymsfield (1997) report on the dimensions of the tropical cirrus ice crystals (in terms of mass equivalent spheres) observed during the Central Equatorial Pacific Experiment (CEPEX). The particles varied between 10 and 1000 μm in size (see Figure 2 of Macquhar and Heymsfield).

Figure 10 presents a representative cirrus spectrum, using the coarse wavelength model of Fu et al.(1993). The effective particle radius is 23 μm, and Fu et al. used hexagonal ice crystal geometry in their calculations.

Though the shapes and sizes of ice crystals are diverse and complicated, the large size of an ice crystal produces a ratio of particle size to infrared wavelength which is also large. (The value of Q_{ext} in Eqn 5 asymptotes to 2, and the extinction spectrum becomes less wavelength dependent). Large particles generally have "flat" i.r. spectra, in comparison to the smaller sulfate particles and PSC particles. Detailed calculations will be used to see which spectral variations are possible for the cirrus particles due to a wide range of particle shape and size.

2.5.1.4 Aerosol homogeneity. Aerosol particles are distributed in the atmosphere in various ways. The sulfate aerosol several years after a major volcanic eruption tends to be uniform. Early after the eruption, however, lidars observe numerous thin layers, which change daily. In the troposphere, the upper troposphere sulfate aerosol is likely to be fairly uniform, while opaque deep convective clouds can be sporadic. Aerosol particles are frequently distributed along the line of sight in a very nonuniform manner, with abrupt and very opaque upper boundaries. This wide range of cloud morphology poses a problem for the interpretation of the HIRDLS radiances. The formulation of aerosol covariance matrices (especially the off-diagonal terms) is problematic.

2.5.2 Aerosol Refractive Indices

The refractive indices of some types of aerosol are dependent on the ambient temperature, and partial pressure of H_2O and HNO_3. For sulfate aerosols, the composition (weight percentage of H_2SO_4) may be determined from thermodynamic calculations [*Steele and Hamill* (1982)]. The complex refractive indices for several aerosol species are tabulated in the HITRAN96 compilation [*Rothman et al.*(1998), *Massie et al.*(1994)], including water, ice, aqueous sulfuric acid, aqueous nitric acid, nitric acid trihydrate (NAT), nitric acid dihydrate (NAD), nitric acid monohydrate (NAM), and amorphous NAT. The indices are measured in the laboratory using thin-film (e.g. see
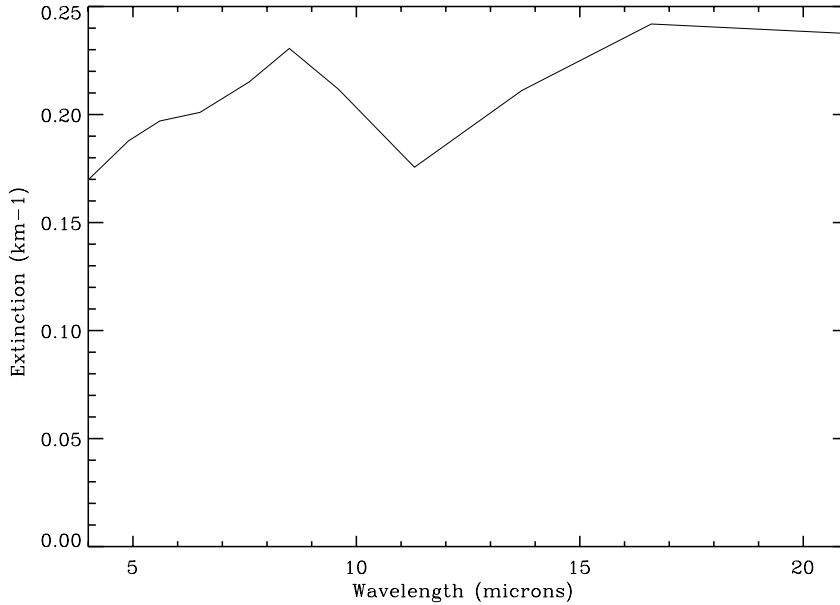
Figure 10: A representative cirrus spectrum calculated for an effective particle radius of 23 μm [*Fu et al.*(1993)].

Toon et al. (1994)) and by measurements using generated particles. Recent laboratory measurements of aqueous sulfuric acid refractive indices at cold temperatures representative of the stratosphere by Tisdale *et al.*(1998) and Niedziela *et al.*(1998) have superceded the room temperature measurements [*Palmer and Williams* (1976)] included in HITRAN96. Ternary solution (H_2SO_4/H_2O/HNO_3) refractive indices are not yet available.

2.5.3 Aerosol Extinction

Aerosol particles both absorb and scatter radiation. For nonspherical particles, a hierarchy of radiative transfer codes will be utilized to calculate aerosol spectra, and to perform sensitivity studies of the effects of particle shape and size upon the particle extinction spectrum. The codes handle spherical particles (using Mie theory) and oblate spheroids (the T matrix codes of Barber et al.(1990) and Mishchenko et al.(1996)). For particles which are very large, and are of diverse shapes (e.g. ice crystals) the geometrical optics (ray tracing) codes of Macke (1993), and the discrete-dipole code of Draine et al.(1994) will be used in exploratory calculations.

For a path segment of length, ds, the increment, $d\chi$, to the optical depth is,

$$d\chi = \beta_{ext}\,ds \tag{3}$$

where

$$\beta_{ext} = \beta_{abs} + \beta_{sca} \tag{4}$$

is the aerosol volume extinction coefficient [km^{-1}], which is the sum of absorption, β_{abs}, and scattering, β_{sca}, terms [*van de Hulst* (1975)]. The dimensionless single scattering albedo, $\omega = \beta_{sca}/\beta_{ext}$, i.e. the ratio of scattering to extinction, plays an important part in multiple scattering calculations [*Liou et al.*(1980)].

For spherical particles, Mie theory can be used to calculate the scattering, absorption and extinction coefficients. The extinction coefficient integrated over a particle size distribution is given by,

$$\beta(\lambda, \eta) = \int_0^\infty \pi r^2\, Q_{ext}(x, m(\lambda, \eta))\, n(r)\, dr \tag{5}$$

where Q_{ext} is the dimensionless Mie extinction efficiency factor, $x = 2\pi r/\lambda$ is the dimensionless size parameter, r is the particle radius, $n(r)$ is the particle size distribution, $m(\lambda, \eta)$ is the complex refractive index of the particle which is a function of the wavelength, λ, and particle composition, η. For size parameters smaller than about 0.25 a particle can be considered to act practically as a pure absorber [*Grainger et al.*(1995)]. This corresponds to drop sizes of less than 0.24 μm for wavelengths greater than 6 μm and is a good approximation for background sulfate aerosols with median radii less than 0.1 μm.

For non-spherical particles, T-matrix [*Barber et al.*(1990)] and discrete-dipole techniques [*Draine et al.*(1994)] can be used to calculate the scattering and absorption for a given particle shape and index of refraction.

2.5.4   Aerosol Spectral Models

It is convenient to define an aerosol spectral factor, F, as the ratio of the extinction at wavelength, λ_c, to the extinction at a reference wavelength, λ_0,

$$F^c[m(\lambda, \eta), n(r)] = \frac{\int_{\Delta\lambda_c} f_c(\lambda) \, \beta(\lambda, \eta) \, d\lambda}{\int_{\Delta\lambda_0} f_0(\lambda) \, \beta(\lambda, \eta) \, d\lambda} = \frac{\beta^c}{\beta^0} \tag{6}$$

where $(f_0(\lambda), \Delta\lambda_0)$ and $(f_c(\lambda), \Delta\lambda_c)$ are the filter functions and spectral passbands of the reference channel and channel c, respectively. In practice, the spectral factor is tabulated simply as a function of channel wavelength, λ_c, composition, η_t, and effective particle radius, r_{e_t}, so that $F^c[m(\lambda, \eta), n(r)] \rightarrow F^c[\lambda_c, \eta_t, r_{e_t}]$ and the extinction in channel c is given by,

$$\beta^c = \beta^0 \times INTERPOLATE(F^c[\lambda_c, \eta_t, r_{e_t}], \eta, r_e) \tag{7}$$

2.5.5   Effects of Sulfate Aerosols on the HIRDLS Channels

The expected perturbations to the radiances measured by HIRDLS is illustrated for a representative sulfate aerosol stratospheric loading (Figures 11 and 12). The aerosol contamination has the smallest impact in the strong CO_2 temperature sounding channels at 15 μm and in the ozone band at 10 μm. The atmospheric window regions near 11 μm and 12 μm show the largest effects as expected.

2.5.6   Multiple Scattering

Multiple scattering effects will have some influence upon the radiation fields sensed by HIRDLS. An illustration of these effects is presented in Figure 13 which shows the percent differences between MODTRAN3 radiance calculations, for cases with and without multiple scattering effects, for a ray path at 20 km for the aerosol loading 939 days after the eruption of Mt. Pinatubo (see Figure 11 for the radiance levels for this case). Due to limitations of the multiple scattering routines which are utilized in the MODTRAN program, the percent differences are set to 0% and to 1% for wavelengths between 14 and 16 μm, and for wavelengths greater than 18 μm. The values are usually much less than 5%. Other examples of the effects of multiple scattering are presented in Echele *et al.*(1998), who present MODTRAN3 radiance calculations at 11, 14, and 16 km altitude, with and without multiple scattering, for conditions which applied to MIPAS-B observations of the Mt. Pinatubo aerosol cloud in March 1992 (nine months after the June 1991 eruption).

It is expected that the multiple scattering effects will be largest for wavelengths at which the ratio of aerosol to gaseous optical depth is largest, and the single scattering albedo is largest. Since the single scattering albedo is a function of aerosol composition (e.g. PSC particles will generally have single scattering albedos larger than that of the sulfate aerosol) the multiple scattering effects will vary as aerosol composition and aerosol layering characteristics varies.

Calculations for sulfate and other aerosol particles (ice particles, PSC ternary droplets, PSC NAT particles) will be carried out to assess the effects of multiple scattering upon the radiation fields sensed by HIRDLS. The MODTRAN3 code will be used in these calculations. Other codes (as yet to be determined) will be used to check upon the MODTRAN3 capabilities and limitations.
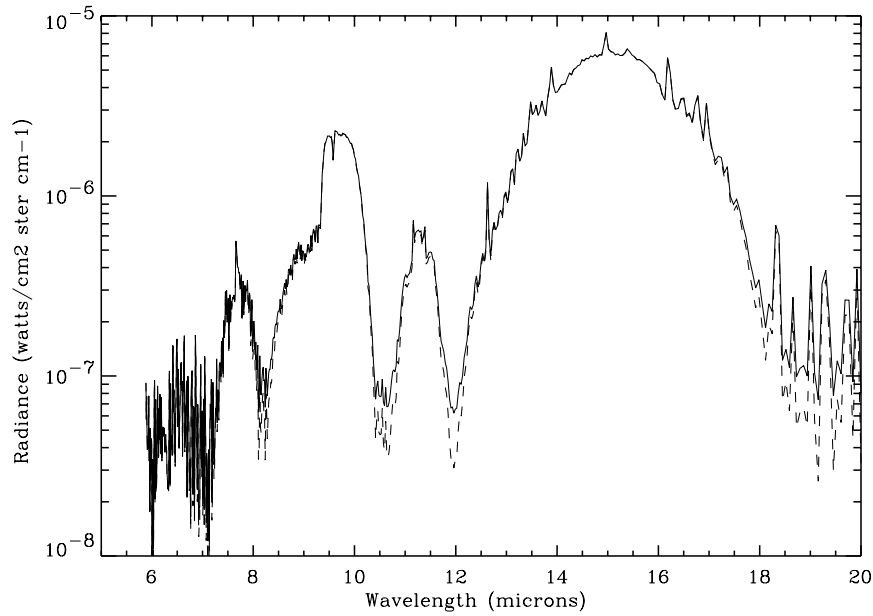
Figure 11: Limb-radiance spectrum covering the HIRDLS wavelength range calculated for a tangent height of 21 km at a mid-latitude location. The solid line includes an aerosol contribution corresponding to conditions 939 days following the Mt Pinatubo eruption. The dashed line is for gaseous species only.
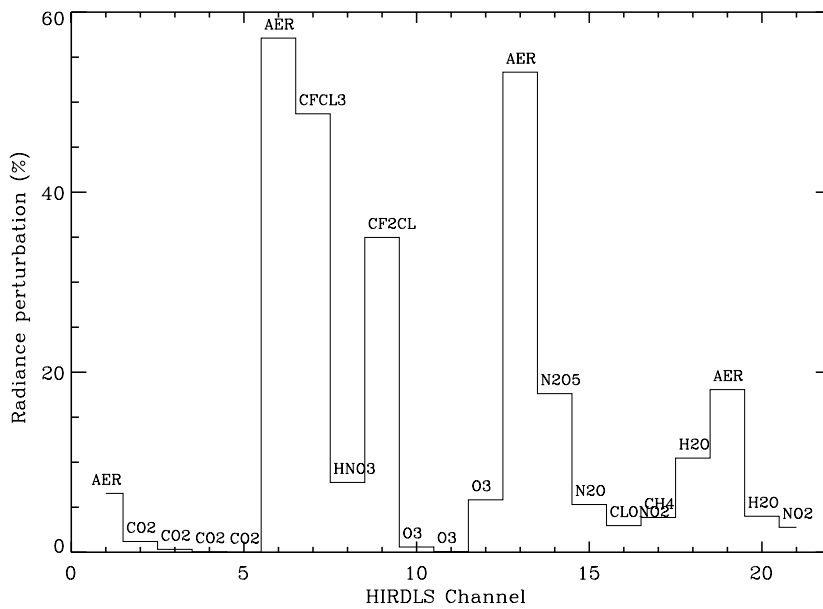
Figure 12: Aerosol induced radiance perturbations in the HIRDLS channels calculated from the data shown in Figure 11. The target species for the HIRDLS channels are shown for reference.
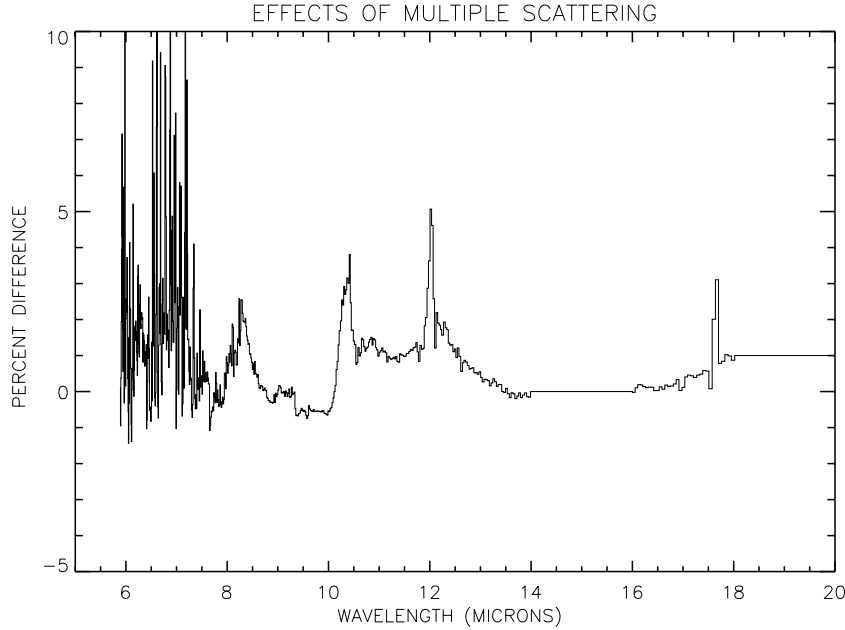
Figure 13: Calculation of the effects of multiple scattering for a ray path at 20 km corresponding to the sulfate aerosol loading 939 days after the eruption of Mt. Pinatubo. The results are presented as percent differences in the radiance calculated with multiple scattering subtracted from the case without multiple scattering.

3 Algorithm Description

3.1 Physics of the Problem

In this section we address the atmospheric remote sounding inverse problem in the context of the HIRDLS observations i.e. the retrieval of temperature and constituent mixing ratios from measurements of the thermal infrared radiance originating from an atmospheric limb path.

The atmospheric forward problem can be stated as the calculation of emergent radiance detected by an instrument for a given atmospheric path and atmospheric model. The atmospheric model specifies the temperature, pressure and mixing ratios of relevant constituents along the atmospheric path. The forward model must take into account not only the physics of the radiative transfer process, but also the peculiarities of the instrument. The actual instrument will have a number of deficiencies from the ideal such as detector noise, calibration errors, finite field of view etc. and of course the radiative transfer cannot be modelled exactly. The inverse problem for HIRDLS is to take the measurements of thermal limb radiances on a set of tangent heights with precisely known spacing and to find a consistent solution in terms of vertical profiles of atmospheric temperature, pressure and constituent mixing ratios with associated errors.

The channel radiance, $R(x_o, h)$, received when viewing a particular tangent altitude, h, at an observation point, x_o, is given by,

$$R(x_o, h) = \int_{-\infty}^{x_o} \int_{\Delta \nu} B(\nu, T(x)) \frac{d\tau(\nu, q(x), x)}{dx} f(\nu) d\nu dx \qquad (8)$$

where x is the position along the ray path which has its tangent point at h, ν the wavenumber, B the Planck function, which depends the temperature T, and τ the transmittance from x to x_o, which depends on the gas mixing ratio q. The channel filter response function is $f(\nu)$ and extends over a spectral passband of width $\Delta \nu$. The term $d\tau/dx$ is known as the contribution function. If this quantity has a large value at a particular altitude, then

the local emission contributes strongly to the measured radiance. The altitude at which the contribution function has its peak value depends on the channel opacity, and using four channels of varying opacity allows good vertical sensitivity. Taking advantage of the known mixing ratio of CO_2 and the hydrostatic equation, the transmittance in a given channel can be calculated, and the radiative transfer equation (Eqn 8) inverted to obtain the temperature and pressure profiles as discussed in Section 3.6.6. Once the temperature and pressure profiles are known, they are used to determine the Planck function profile for the trace gas channels. This profile, along with the measured radiance in each channel, allows the transmittance of each trace gas species to be determined. The mixing ratio distribution can then be found.

The retrievals will be carried out using inversion techniques that have been developed and applied successfully in the atmospheric remote sounding field for many years [*Rodgers* (1976), *Rodgers* (1990)]. These techniques yield a formalism for the retrieval algorithms which bring an elegant approach to the areas of error analysis and diagnostic information. The degree of non-linearity of the limb-sounding inverse problem is such that simple regression techniques are not applicable.

3.2   Radiance Pre-processing

The purpose of the pre-processing step is to extract calibrated radiance, pointing and ancillary data from the Level-1 data file and to prepare the data for Level-2 processing. Several procedures must be applied to the data, and supporting calculations made before the data are passed to the retrieval algorithm. Once processed, the measured radiance profiles, one for each of the 21-spectral channels, will have been placed onto a common, uniformly spaced tangent height grid. An estimate of errors due to pointing uncertainties will be made based upon scan angle encoder and gyroscope measurement errors determined during Level-1 processing. The presence of high cloud in the field of view will be detected and the cloud-top altitude determined. The effect of the finite detector field-of-views on measured limb radiance profiles must be considered, either in the modeling of limb radiances in the retrieval algorithm or by correcting the limb radiances by deconvolution in pre-processing step. Both approaches will be explored during the algorithm development process and the relative merits quantified in terms of accuracy and computational speed. A decision on the approach to handling the FOV effect will be made before final implementation of the operational algorithm.

3.2.1   Extract and Prepare Vertical Scans

Valid elevation (or vertical) scans will be extracted from the Level-1 data file using a scan direction flag which has been set during Level-1 processing. Non-standard scan patterns and azimuth-step data will be written to a separate file for off-line processing. Scale factors are applied to radiance and pointing data and values flagged as bad during the Level-1 process will be replaced by interpolation of nearby samples. It is expected that limb radiance samples will not be uniformly spaced in elevation angle, with an occasional reversal in the direction of samples, caused by mechanical disturbances imported from the spacecraft. Since sample reversals are possible, the vertical scans must be sorted into ascending (or descending) order for later interpolation onto the tangent height grid.

The pointing information obtained from encoder and gyroscopic measurements are defined for the instrument boresight direction. To determine the actual pointing direction for the individual spectral channels, the angular offsets measured during pre-flight calibration must be applied (see Figure 2 for reference). The offsets measured near zero azimuth scan position are expected to change a small amount with azimuth scan position due to the scan geometry and a correction must be applied to vertical scans over the range of azimuth angles in a swath.

3.2.2   Cloud Detection

The presence of high clouds along the limb path must be flagged for Level-2 processing to identify the affected radiances and set a lower altitude bound for inversion of the radiance data. Retrieval of clouds parameters, and temperature and constituent concentrations in altitude regions where clouds are present will not be part of the operational algorithm, but will be the focus of research-mode processing. The optically thin spectral channels, particularly channels 6, 13 and 19, will clearly show enhanced radiance when a thick cloud is present; the cloud signature appears as a sharp increase in limb radiance due to the increased limb opacity. The altitude location of

the cloud top will be estimated using the LOS angle associated with the cloud-top and knowledge of the spacecraft position. Cloud-top altitude can be determined with high vertical resolution (200 m). An optically thin aerosol channel is located in each of the three columns on the detector focal plane array making some measure of the horizontal extent (in the across-track direction) of the cloud possible.

3.2.3 FOV Convolution/Deconvolution

The effect of instrument spatial response on the information content of measured limb radiances has been discuss previously by Gille and Bailey (1978) and Peckham (1995). Removing the spatial response from the measured limb radiance profile by a deconvolution process before inversion has the potential advantage of computational efficiency and has been successfully used on previous limb experiments [*Bailey and Gille* (1986)]. The deconvolution can be implemented efficiently using a fast Fourier transform technique and performed only once during the pre-processing step. An alternate and more direct approach is to apply the measured FOV response to simulated radiances produced by the forward model. The vertical spacing required for the convolution or deconvolution will depend upon the expected scale of vertical variations in the limb profile and small-scale variations in FOV response. A concern with inclusion of the FOV effect in the forward radiance model is the additional computational burden that may result if several iterations of the retrieval process are necessary and if fine tangent height spacing is necessary. Currently, both approaches are under study.

3.2.3.1 Convolution. Small-scale vertical features in the radiance profile, produced by variations in temperature and constituent concentrations, are smoothed by the detector FOV as it is scanned across the limb. This smoothing reduces the amplitudes of high spatial frequency components and must be carefully modeled or the effect removed to achieve the high vertical resolution requirements for HIRDLS observations.

Smoothing by the detector FOV can be expressed as a convolution of the FOV response with the limb radiance profile, assuming the FOV response is invariant with vertical scan position. This is a reasonable assumption for vertical scans near zero degrees in azimuth. Corrections for vertical scans at the extreme azimuth positions may be necessary. Mathematically, the convolution integral is,

$$g(\theta) = \int_{-\infty}^{\infty} h(\theta - \xi) \, f(\xi) \, d\xi \tag{9}$$

where $h(\theta)$ represents the vertical response function of a detector channel as a function of relative line-of-sight elevation angle, θ, and $f(\xi)$ is the limb radiance profile specified on the same relative angle scale.

The vertical response function is defined as the horizontally integrated spatial response of a spectral channel to incident radiation. For the HIRDLS detectors, the vertical response is determined by the finite field-of-view (FOV) of a detector, and to a lesser extent by diffraction, aberrations and electronic response. An example of the FOV response for HIRDLS channel 10 calculated assuming a 1 km FOV for the detector and the effect of diffraction is shown in Figure 14 (0 degree curve).

The vertical response function is affected by a rotation of the FOV, which can be caused by spacecraft attitude (expected to be 2 degrees or less) or by the scan mirror geometry, as shown in this figure. Rotation caused by spacecraft roll will be defined by a field rotation angle calculated during Level-1 processing. The rotation due to scan mirror geometry is well characterized by $\alpha = 2\epsilon_m \, sin\phi_m$, where ϵ_m and ϕ_m are the elevation and azimuth mirror position angles. For the extreme elevation and azimuth position, a = 1.5 degrees.

The convolution integral can be equivalently expressed in the Fourier domain,

$$G(s) = H(s).F(s) \tag{10}$$

The Fourier spectra of the actual and measured limb radiances are $F(s)$ and $G(s)$, respectively. $H(s)$ represents the Fourier transform of the vertical response function, which is often referred to as the system modulation transfer function (MTF). For all of the HIRDLS spectral channels, H(s) rolls-off smoothly with increasing spatial frequency, approaching zero at the detector cutoff, i.e. 1 km^{-1} in object space (see Figure 14). Spatial frequency components beyond the detector cutoff will have been attenuated below the expected radiometric noise level and
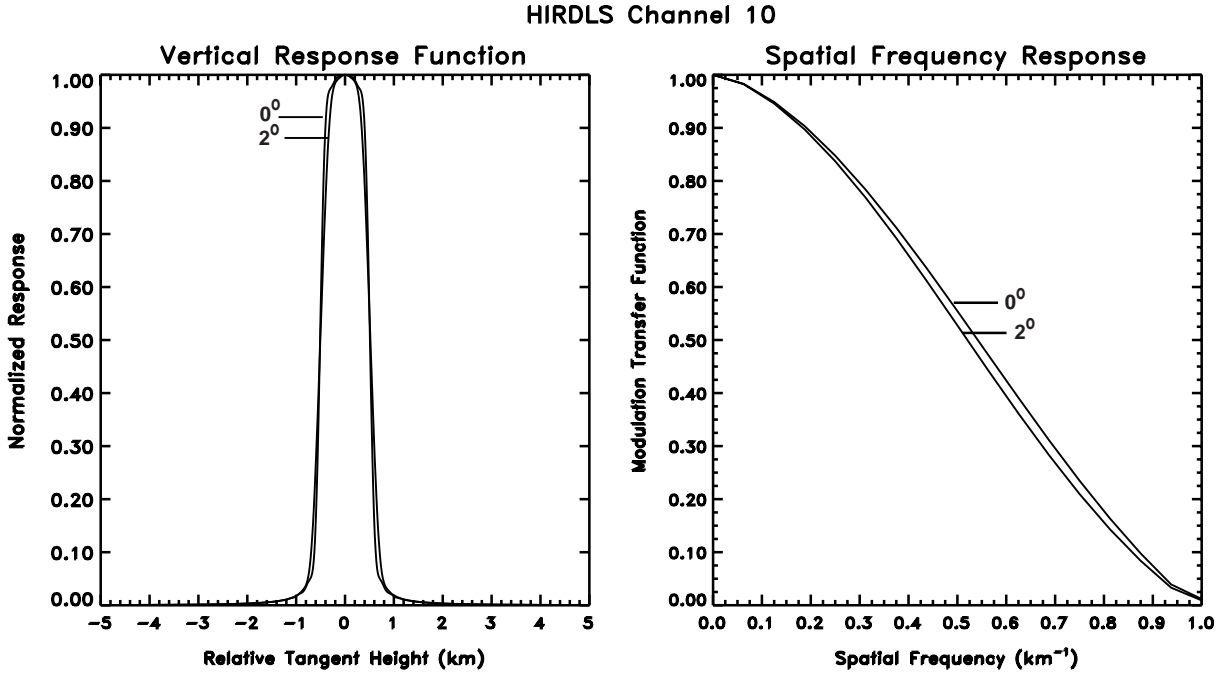
Figure 14: Modeled FOV response for channel 10 for the nominal case (0 degree) and with a 2 degree rotation.

therefore cannot be reconstructed from the measure limb profiles. This sets a practical upper limit on the smallest distinguishable vertical scales that can be recovered from HIRDLS observations. Vertical spacing in the retrievals significantly less than one-half of this provides no additional information.

3.2.3.2 Deconvolution. An alternative to modeling the FOV convolution in the forward radiance calculation is to remove the effect before inversion of the radiance profiles. To recover the original limb spectrum, Equation 10 may be directly inverted ([*Brault and White* (1971)]),

$$F(s) = H(s)^{-1}.G(s) \tag{11}$$

and the deconvolved radiance profile reconstructed from $F(s)$ by an inverse Fourier transform. The inverse MTF restores the amplitudes of high spatial frequency components attenuated by the instrument MTF. Note that this is a restoration process seeking to preserve the original signal spectrum and is not an enhancement process. The direct inversion method is problematic because in the presence of measurement noise, the solution becomes unbounded as $H(s)$ approaches the detector cutoff frequency due to the of amplification of high frequency noise components. Regularization techniques are commonly used to condition the problem, and to produce stable and meaningful solutions by applying some form of smoothing ([*Andrews* (1974)], [*Banham and Katsaggelos* (1977)]), e.g.,

$$F(s) = H(s)^{-1}.G(s).R(s) \tag{12}$$

The form of the restoration filter, $R(s)$ depends upon assumptions about the original signal using either stochastic or deterministic models. An example of an approach based on a stochastic model of the signal is the optimal (or Wiener) filtering technique where the product $H(s)^{-1}.R(s)$ forms the Wiener filter ([*Andrews and Hunt* (1977)]). The optimal filtering approach seeks to minimize the mean-square error between the restored and true signals. This method requires knowledge of the power spectrum of the signal. Estimates of the original signal spectrum are often made indirectly using the observed spectrum.

Preliminary analysis showed that the final results were rather sensitive to how well the signal spectrum could be estimated from the observed signal. Therefore following an approach similar to that used for LIMS processing ([*Bailey and Gille* (1986)]), the restoration filter $R(s)$ will be a fixed lowpass filter of high order. This approach maintains a consistent frequency response over all profiles. An optimum channel-dependent cutoff frequency will be chosen by simulation. A possible criterion for setting the cutoff would be to find the spatial frequency where the signal spectrum equals the noise spectrum. From the results of a limited number of simulations, this cutoff frequency will likely be 0.6 to 0.7 km^{-1}, corresponding to vertical wavelengths of about 1.5 km. Beyond this cutoff frequency, the observed limb spectrum is dominated by measurement noise. Therefore, it will be possible to distinguish small vertical variations in the limb radiance profiles, and hence in temperature and constituent retrievals, having spatial wavelengths greater than about 1.5 km. The field-of-view deconvolution process can be efficiently implemented in the Fourier frequency domain by using Fast Fourier Transform (FFT) algorithms. Application of the FFT routine will require radiance samples be expressed on a uniformly spaced grid with a spacing consistent with the information content of the limb profile. For global mode observations, this suggests a relative angle spacing of approximately 14 arcsec (equivalent to 200 m at the limb) between radiance samples to maintain the desired over-sampling. The end-points of a profile will be extended and a smooth transition from zero to each end-point added to eliminate end-around leakage in the convolution and the introduction of spurious frequency components generated by an abrupt transition. Finally, computationally efficient FFT routines require the number of data points to be a power of 2, therefore the "conditioned" profile will be extended by zero padding. The restored profile is extracted from the inverse transform of the deconvolved profile and placed onto a uniform grid with a nominal 0.75 km tangent height spacing.

3.2.4 Interpolation to a Uniform Tangent Height Grid

Calculation of the tangent height of a radiance sample given the measured elevation and azimuth LOS angles in the spacecraft reference coordinate frame (SRCF), and knowledge of the spacecraft position will make use of the SDP toolkit geolocation routines (Section 5.1.1). The boresight LOS vector is defined for each radiance sample based upon the measured elevation and azimuth angles in SCRF. The vector must then be transformed into the earth-centered rotating coordinate frame (ECR) using the toolkit routine PGS_CSC_SCTOECI followed by the PGS_CSC_ECITOECR routine. The spacecraft position in earth-centered inertial coordinate frame (ECI) is obtained from the Level-1 data file at approximately 0.8 sec intervals. The spacecraft position must be transformed into the ECR frame. The toolkit grazing ray routine is called to obtain the tangent height, and the latitude and longitude of the boresight. The pre-calculated detector offsets are added to the boresight tangent point to obtain the channel-dependent tangent points. The radiance samples are then interpolated onto a common, uniform, tangent height grid with a nominal spacing of 0.75 km and covering a range from 0 to 150 km using a smoothing cubic spline designed for noisy data ([*de Boor* (1978)]).

3.2.5 Estimating Pointing Errors

The angular elevation and azimuth position of the scan mirror relative to the optical bench coordinate frame (referred to as the telescope reference coordinate frame or TRCF) is measured by high resolution optical encoders. A tilt of the azimuth axis due to imperfect behavior of the azimuth bearings will be measured by Kaman proximity sensors, referred to as wobble sensors. Motion (and hence attitude) of the optical bench will be measured by the HIRDLS gyroscope mounted on the bench. Estimates of sensor measurement precessions will be made in Level-1 processing and output to the Level-1 data file. These data are then used to estimate the radiance error due to imprecise pointing knowledge using the following expression,

$$\sigma_p^2 = \left(\frac{\partial N}{\partial \theta} \right)^2 \left(\sigma_e^2 + \sigma_g^2 + \sigma_w^2 \right) \tag{13}$$

where the variance in radiance due to random pointing error is σ_p^2, the individual sensor noise variances are σ_e^2, σ_g^2 and σ_w^2 corresponding to elevation encoder, gyroscope and wobble sensors, respectively. The term $\frac{\partial N}{\partial \theta}$ is the radiance derivative with respect to elevation angle,

$$\frac{\partial N}{\partial \theta} = \frac{\partial N}{\partial h} \frac{\partial h}{\partial \theta} \tag{14}$$

where the vertical gradient of the radiance profile $\frac{\partial N}{\partial h}$, is calculated from the gridded radiance data and $\frac{\partial h}{\partial \theta}$ is the derivative of the tangent altitude with respect to the elevation angle.

An estimate of pointing jitter noise, σ_j, due to LOS motions, σ_{los}, with frequencies above the measurement bandwidths of the pointing sensors is given by,

$$\sigma_j^2 = \frac{q}{2} \left(\frac{\partial^2 N}{\partial h^2} \right)^2 \sigma_{los}^2 \tag{15}$$

The non-linear jitter error depends upon the second derivative of the radiance profile. The parameter q is a channel dependent constant determined from simulations. The on-orbit LOS jitter level cannot be determined from measurement and must be estimated based upon model predictions of the instrument mechanical behavior and expected vibrational disturbance levels imported from the spacecraft.

3.3 Radiance Forward Model

The purpose of the forward model is to provide a simulation of the calibrated Level 1 radiances (which may have undergone pre-processing at Level 2 to deconvolve the field of view) from the given atmospheric input data.

3.3.1 Forward Model Hierarchy

We are developing a hierarchy of forward models which are specifically adapted to the somewhat disparate requirements of prototype algorithm development and operational processing. In the former case it is important to have models available which retain the essential physics of the measurement. In the latter case the speed of execution is a primary concern and this can only be achieved through using more highly parameterized models. A schematic diagram showing the forward model hierarchy is shown in Figure 15. At this time, more than three years before launch, the forward models that we have in place are: GENLN2, a state of the art line-by-line model; a reasonably fast absorption coefficient look-up table code; and a fast model for use in instrument studies. The new line-by-line GENLN3 version will be available at the end of 1999. Our group has also gained considerable expertize from developing the EOS-TERRA/MOPITT instrument operational forward models. This has led to experience working with different fast model approaches, and we already have several codes in-house. These are based on the techniques described in Section 3.3.5 and each of these will be evaluated for the HIRDLS application by constructing a prototype code. The final decision regarding the selection of one of these codes as the operational forward model will be made closer to launch and will depend on the results of sensitivity studies, and accuracy and performance considerations.

3.3.2 Radiative Transfer Equation for Limb-Sounding Application

The forward model solves the radiative transfer equation for a given observation geometry and atmospheric model. Consider the passage of radiation of wavenumber ν [cm^{-1}] in the z-direction through an element of absorber thickness dz [cm]. The radiation attenuation is,

$$-dI(\nu, z) = I(\nu, z) \, \kappa(\nu, z) \, \rho_a(z) \, dz \tag{16}$$

where $I(\nu, z)$ [W/(m^2.sr.cm^{-1})] is the radiation intensity, $\rho_a(z)$ [mol m^{-3}] is the absorber molar density, and $\kappa(\nu, z)$ [m^2 mol^{-1}] is the monochromatic absorption cross-section. Integrating this equation from a source point z_s to an observation point z_{obs} gives,

Forward Model Hierarchy

GENLN3: LBL CODE
- **Full Physics**
- **Benchmark Studies**
- **Parameter Generation**

HIRDLS Specific Model

| Retrieval Interface | Geometry & Raytracing | Calculation of Channel Transmittances | Radiative transfer |

Absorption Coefficient Look-Up Table

- **Monochromatic Calculation**
- **Retains Access to Physics**

Operational Fast Model

- **CG/EGA**
- **OPTRAN**
- **Correlated-k**
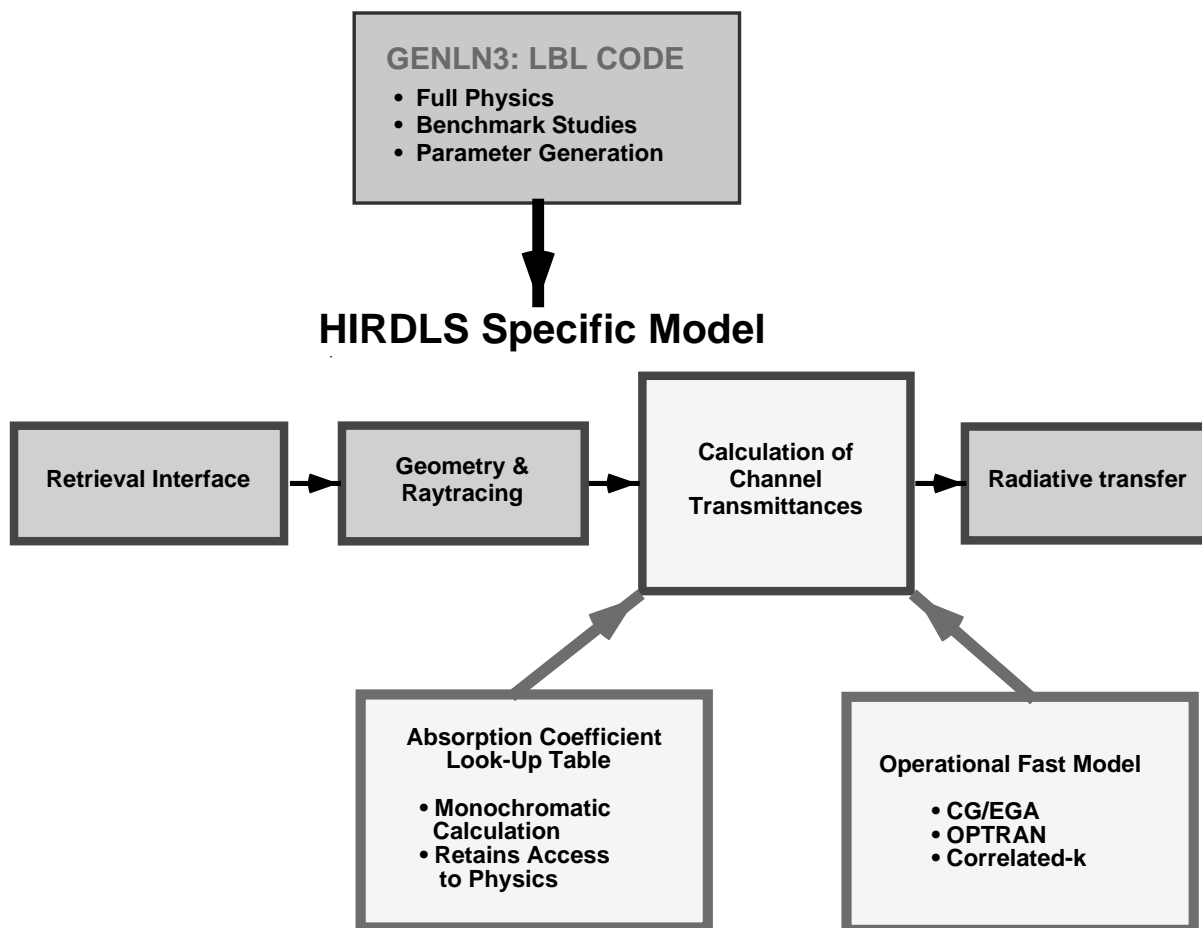
Figure 15: Schematic of the development of the HIRDLS forward model hierarchy.

$$\int\limits_{I(\nu,z_s)}^{I(\nu,z_{obs})} \frac{-dI(\nu,z)}{I(\nu,z)} = \int\limits_{z_s}^{z_{obs}} \kappa(\nu,z)\,\rho_a(z)\,dz \qquad (17)$$

and performing the integral we obtain,

$$\tau(\nu,z_s,z_{obs}) = \frac{I(\nu,z_{obs})}{I(\nu,z_s)} = \exp\left(- \int\limits_{z_s}^{z_{obs}} \kappa(\nu,z)\,\rho_a(z)\,dz\right) \qquad (18)$$

where $\tau(\nu,z_s,z_{obs})$ is defined as the transmittance between z_s and z_{obs}.

The element of absorbing gas will also emit radiation, the intensity of which depends on its temperature T [K]. Under local thermodynamic equilibrium (LTE) conditions the source function is given by the Planck function, $B(\nu,T)$ [W/(m^2.sr.cm^{-1})],

$$B(\nu,T) = \frac{c_1\nu^3}{\exp(c_2\nu/T) - 1} \qquad (19)$$

where $c_1 = 2hc^2 = 1.19104 \times 10^{-8}$ W/(m^2.sr.cm^{-4}), $c_2 = hc/k = 1.439$K/cm^{-1}, and h, k and c are the Planck constant, Boltzmann constant and speed of light, respectively. Thus from Eqn 16, the absorbed radiation in the z-direction would be $B(\nu,T)\,\kappa(\nu,z)\,\rho_a(z)\,dz$. Assuming the gas to be in local thermodynamic equilibrium (LTE), the temperature must remain constant, and it follows from Kirchhoff's law that the radiation intensity emitted in the z-direction will also be $B(\nu,T)\,\kappa(\nu,z)\,\rho_a(z)\,dz$.

The radiative transfer equation will therefore have two parts: a transmitted radiation component which depends on the intensity at z_s and the transmittance from z_s to z_{obs}, and a radiation component due to the emission from all elements dz between z_s and z_{obs} that actually arrives at z_{obs},

$$I(\nu,z_{obs}) = I(\nu,z_s)\,\tau(\nu,z_s,z_{obs}) + \int\limits_{z_s}^{z_{obs}} \left[B(\nu,T(z))\,\kappa(\nu,z)\,\rho_a(z)\,dz\right]\tau(\nu,z,z_{obs}) \qquad (20)$$

3.3.2.1 Atmospheric layering. The inhomogeneous nature of the atmosphere along a radiation path is most readily treated by sub-dividing the atmosphere into a series of layers. In this way, the integration over z becomes a summation over the constituent layers. The layer boundaries should be chosen in such a way that the gas within the layer may be considered homogeneous and well represented by appropriate Curtis-Godson absorber weighted mean parameters for temperature and pressure. For a given tangent height the atmosphere is divided into a series of layers that are thin close to the tangent height (0.1 km) and progressively thicker towards the top of the atmosphere. This structure reflects the fact that most of the limb radiance originates from close to the tangent point. Within each layer, a series of single gas paths are defined along the actual ray trajectory within the layer for each of the different gases comprising the layer. Since the gas within the layer is homogeneous, a path forms the basic unit for the calculation of optical depth. The optical depths for each of the single gas paths within each layer are calculated and then these are combined monochromatically in spectral space to obtain the multi-gas optical depths of each layer.

3.3.2.2 Ray tracing. The atmospheric layer boundaries must be chosen to ensure that sufficient layers are used for an accurate radiative transfer calculation. Once the layer structure has been determined, a path is defined for each of the required gases within the layer. Figure 16 shows a 2D vertical cross-section, (h,ψ), along the line of sight. As the the limb-sounder scans up or down the atmosphere a locus of geometrical tangent point altitudes are defined which do not lie on a vertical through the Earth's center. A reference tangent height is selected which is
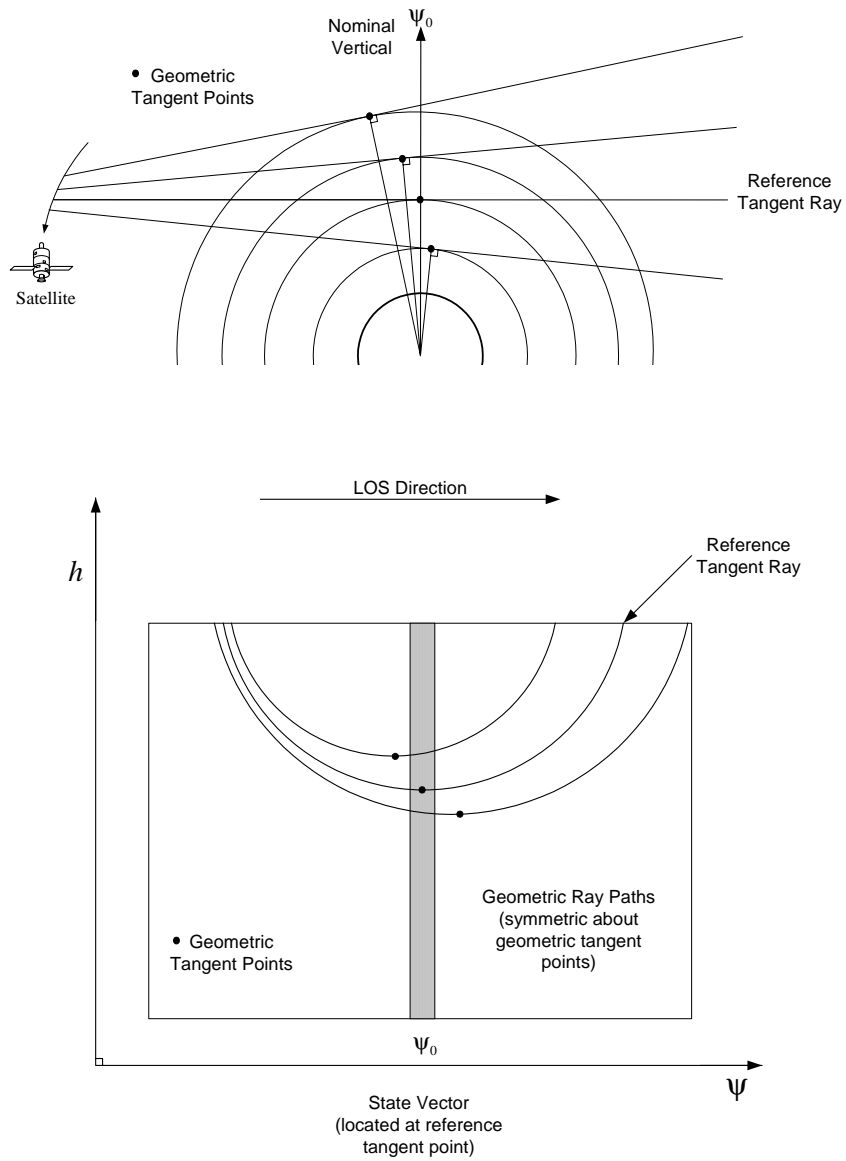
Figure 16: Geometry for the limb-sounding problem.

used to define the nominal vertical profile location, ψ_0, along the line of sight and its (latitude, longitude) position on the Earth. The state vector (see Section 3.4.1.2) is located at this reference position as are the atmospheric profiles used in the retrieval. Figure 17 shows schematically that atmospheric refration deviates the light ray from the geometric path resulting in a true tangent point which is lower in altitude and further from the satellite than the geometric (or apparent) tangent point location. This is the true path through the atmosphere and it must be modelled adequately to achieve an accurate radiative transfer calculation.
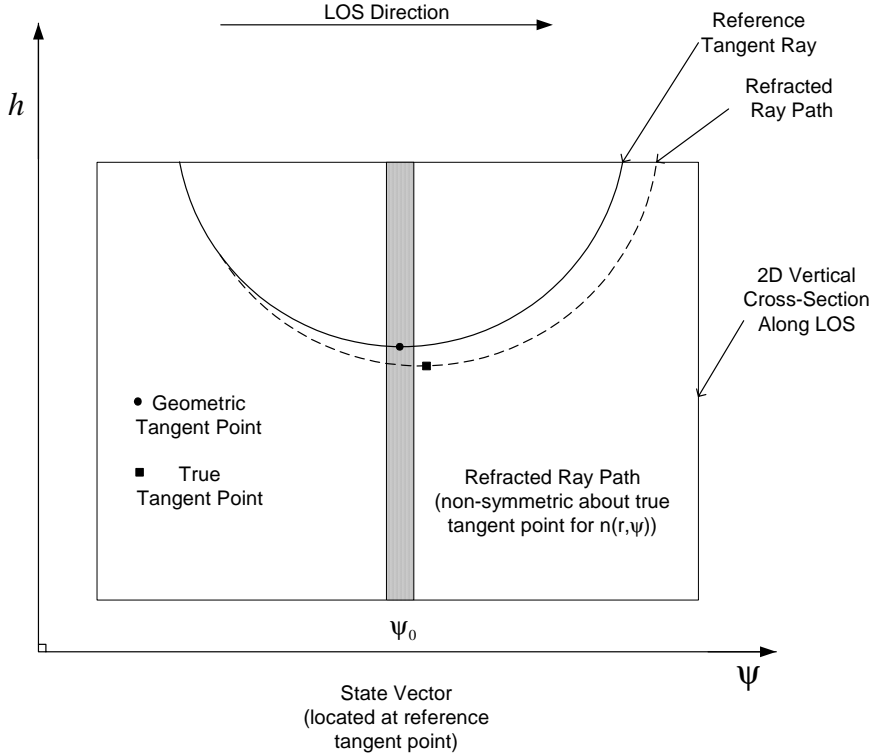
Figure 17: Effects of atmospheric refraction on a ray path.

3.3.2.2.1 Horizontally homogeneous atmosphere. For a horizontally homogeneous atmosphere (i.e. circularly symmetric in the plane of the ray), the refractive varies only as a function of altitude, i.e. $n(r)$, The parameters required to define the ray trajectory over the path are the layer boundary altitudes and the local zenith angle at the lower layer boundary. For a limb-viewing geometry, the initial ray zenith angle at the lowest boundary of the atmosphere is $90°$. The local zenith angle θ at the lower boundary of each layer is then calculated according to Snell's law,

$$C = n(r)r\sin\theta \tag{21}$$

where C is a constant along the ray path and $n(r)$ is the refractive index of air at Earth radius of curvature r. A vertical profile for the refractive index of air is calculated from the atmospheric temperature, pressure and water vapor profiles for use in the ray-tracing algorithm.

3.3.2.2.2 Horizontally inhomogeneous atmosphere.   In general there are atmospheric variations along the line of sight, (for a discussion of the treatment of line of sight gradients see Section 3.6.4). An addition complication is that the refractive index varies as a function of altitude and line of sight angle, i.e. $n(r, \psi)$. It can be shown that the vector equation for the propagation of a light ray is given by (Born and Wolf (1975)),

$$\frac{d}{ds}\left(n(\mathbf{r})\frac{d\mathbf{r}}{ds}\right) = \nabla n(\mathbf{r}) \tag{22}$$

where $\nabla n(\mathbf{r})$ is the gradient field of the refractive index. An equation can be obtained expressing the change in the angular deviation of the ray as a function of the line of sight position, $\frac{d\epsilon}{ds}$,where $\epsilon = \psi + \theta$, (see Figure 18)

$$\frac{d\epsilon}{ds} = \frac{1}{n(\mathbf{r})}\nabla n(\mathbf{r}) \cdot \hat{\mathbf{e}}_{\updownarrow} \tag{23}$$

where $\hat{\mathbf{e}}_{\updownarrow}$ is the unit vector perpendicular to the direction of propagation. Equation 23 yields the refracted ray path in terms of the radial distance, $r(s)$, zenith angle, $\theta(s)$, and line of sight angle, $\psi(s)$.

3.3.2.2.3 Reference geoid.   The reference geoid is the surface of constant gravitational potential, which for some applications can be approximated as an ellipsoid. However, since the ellipsoid deviates by up to 110 m from the geoid a more accurate analysis is required for HIRDLS. The WGS 84 reference frame is coordinated in latitude, ϕ, longitude, λ, and altitude, h, above the WGS 84 reference ellipsoid. The SDP Toolkit routine PGS_CSC_GrazingRay determines the tangent point in (ϕ, λ, h). The height above the geoid is called the "orthometric height", H, and is obtained from the ellipsoidal height by, $H = h - N$, where N is the geoid height relative to the ellipsoid which is obtained from the digital elevation model (DEM) using PGS_DEM_GetPoint..

3.3.2.2.4 Path quantities.   When the ray paths have been fully defined, the Curtis-Godson absorber weighted mean values are calculated for each path j. The integrated absorber amount u_j for the ray path s between the vertical layer boundary heights z_{l_-} and z_{l_+} is,

$$u_j = \int_{z_{l_-}}^{z_{l_+}} \left(\rho_a(z)_j \frac{ds}{dz}\right)dz \tag{24}$$

where $\rho_a(z)_j$ is the local molar density of gas j. The mean values for the path pressure p_j and temperature T_j are,

$$p_j = \frac{1}{u_j}\int_{z_{l_-}}^{z_{l_+}} p(z)\left(\rho_a(z)_j \frac{ds}{dz}\right)dz; \qquad T_j = \frac{1}{u_j}\int_{z_{l_-}}^{z_{l_+}} T(z)\left(\rho_a(z)_j \frac{ds}{dz}\right)dz \tag{25}$$

In this way, slightly different values for the layer mean temperature and pressure are obtained for each path gas. The layer is sub-divided into several thinner layers in order to perform the in-layer ray tracing and integration. The algorithm used is similar to that used in the LOWTRAN7 code [*Kneizys et al.*(1988)]. The temperature is assumed to vary linearly between the layer boundaries, whilst the pressure varies exponentially. The transmittance of the line of sight segment layer is obtained from either line-by-line calculation or from one of the chosen tabulation methods of Section 3.3.4.

$\psi = 0$

Refractive
Index
$n = n(r, \psi)$

Geometric
Tangent Point

Geometric Ray

θ_0

True Tangent
Point

s

ψ

h_g

θ

h_t

$\theta + d\theta$

h_0

Refracted Ray

$r_0 = r_c + h_0$

$d\psi$

r_c

$-\psi_0$

ψ
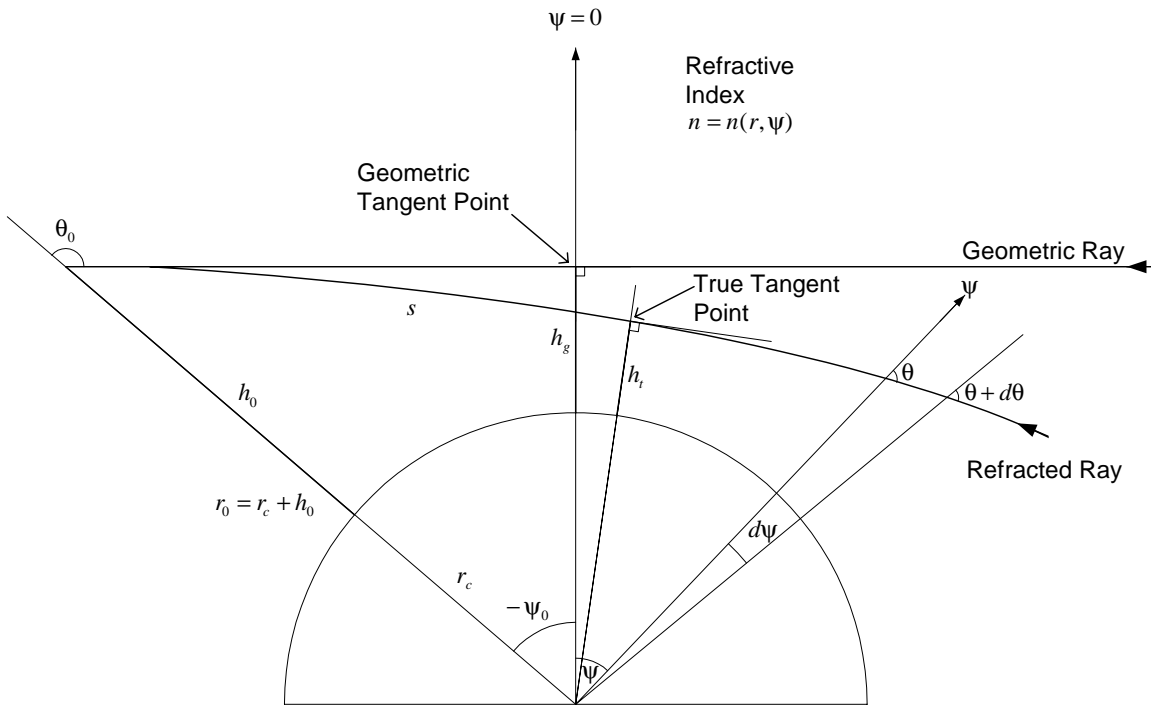
r_c = Radius of curvature of geoid at (lat,lon) location of the reference tangent point in the direction of LOS.

Refractive index of air: a) horizontal homogeneity   : $n = n(r)$

b) LOS variation in T, p, H_2O : $n = n(r, \psi)$

Vector equation for propagation of light ray   : $\dfrac{d}{ds}\left(n(\underline{r})\dfrac{d\underline{r}}{ds}\right) = \nabla n(\underline{r})$

$\hat{\underline{r}}$

$\hat{\underline{e}}_{\Leftrightarrow}$

y

$d\varepsilon$

dx

ε

$r = \sqrt{x^2 + y^2}$

$\psi = \tan^{-1}\dfrac{x}{y}$

dy

ε

ds

$\psi\ \theta$

$\dfrac{dr}{dx} = \dfrac{y}{r}$

$\dfrac{dr}{dy} = \dfrac{x}{r}$

$\nabla n(\underline{r})$

$\dfrac{d\varepsilon}{ds} = \dfrac{1}{n(\underline{r})}\nabla n(\underline{r}) \cdot \hat{\underline{e}}_{\Updownarrow}$

$\theta = \cos^{-1}(\hat{\underline{r}} \cdot \hat{\underline{e}}_{\Leftrightarrow})$

$\dfrac{d\psi}{dx} = \dfrac{y}{r^2}$

$\varepsilon = \psi + \theta$

$\hat{\underline{e}}_{\Updownarrow} \cdot \hat{\underline{e}}_{\Leftrightarrow} = 0$

$\dfrac{d\psi}{dy} = -\dfrac{x}{r^2}$

$\hat{\underline{e}}_{\Updownarrow}$

$\underline{r}$

$\hat{\underline{e}}_{\Leftrightarrow} = \dfrac{d\underline{r}}{ds} = \left[\dfrac{dx}{ds}, \dfrac{dy}{ds}\right] = [\sin\varepsilon, \cos\varepsilon]$

$\underline{r} + d\underline{r}$

ψ

$\hat{\underline{e}}_{\Updownarrow} = [\cos\varepsilon, -\sin\varepsilon]$

x
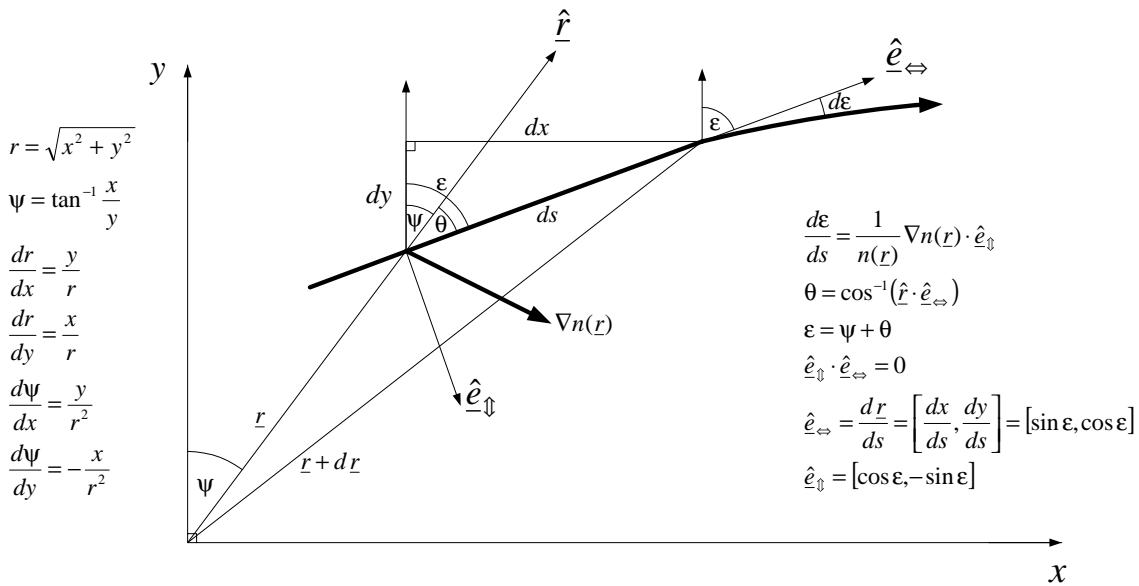
Figure 18: Ray tracing geometry.

3.3.2.3 Spectroscopic data. The most widely used spectroscopic database is the AFGL/HITRAN (Air Force Geophysical Laboratory / High Resolution Transmission) Molecular Absorption Data base [*Rothman et al.*(1992)]. The latest edition of HITRAN is described by Rothman *et al.*(1998). This database is the most logical choice for use with the HIRDLS as it is by far the most comprehensive. In addition to spectral line data, the HITRAN database also includes the most up-to-date compilation of heavy molecule absorption cross-section data for those species for which line parameters are not yet available. Other spectral parameters required are the line coupling coefficients, which are themselves based on data from HITRAN. The line coupling model is discussed in [*Edwards* (1992)].

For the work presented in this document, the Voigt line shape [*Humlicek et al.*(1982)] was used for all calculations. For CO_2, the Voigt profile was modified by a temperature dependent exponentially decreasing χ-factor to take into account the duration of collision effects. Also, spectral line mixing in significant *Q*-branches was included [*Edwards et al.*(1991)]. For H_2O, the line shape of Clough *et al.*(1980) was used to account for non-Lorentzian line wings and the water vapor continuum. H_2O line wings were cutoff at a distance of 25 cm^{-1} from the line center and at greater distances the absorption was included using a precomputed continuum calculated using all lines and the appropriate line shape. The data for the O_2 pressure induced absorption band at 1550 cm^{-1} were taken from Orlando *et al.*(1991). For certain gas species that HIRDLS plans to measure, spectral line data are not currently available. In these cases, high resolution temperature dependent laboratory cross-section data have been employed. The data for CFC11, CFC12, CF_4, and N_2O_5 come from the measurements of McDaniel *et al.*(1990), and that for $ClONO_2$ from Ballard *et al.*(1988).

Future modeling activities will use the absorption cross sections reported on the the latest edition of the HITRAN database. These include the pressure and temperature dependent CFC compilation based on the laboratory measurements of Varanasi and Nemtchinov (1994) and Li and Varanasi (1994).

3.3.2.4 Monochromatic spectral radiance calculation. For the HIRDLS limb viewing geometry with the satellite at a position z_{obs}, the observed radiance will be due to atmospheric thermal emission alone and the radiative transfer equation from Eqn 20 becomes,

$$I(\nu, z_{obs}) = \int_{z_b}^{z_{obs}} \left[B(\nu, T(z)) \, \kappa(\nu, z) \, \rho_a(z) \, dz \right] \tau(\nu, z, z_{obs}) \tag{26}$$

where z_b is the effective edge of the Earth's atmosphere on the far side of the tangent point, ρ_a is the density of the absorbing gas and $B(\nu, T)$ is the Planck emission function at temperature T.

In the radiance calculation, the atmosphere is considered sub-divided into a number of homogeneous layers. The total optical depth of each layer l is defined from the path optical depths, $k(\nu)_j u_j$, of each gas. Assuming that the layer is made up of J single gas paths, the total layer optical depth $\chi(\nu)_l$ will be,

$$\chi(\nu)_l = \sum_{j=1}^{J} \kappa(\nu)_j u_j \tag{27}$$

and the layer transmittance is,

$$\tau(\nu)_l = \exp(-\chi(\nu)_l) \tag{28}$$

Each layer also has an associated temperature T_l which is an absorption weighted mean of the path temperatures that constitute the layer. For a layer in LTE, this allows the layer thermal emission $E(\nu)_l$ to be defined from the integral in Eqn 26 as,

$$E(\nu)_l = B(\nu, T_l) \sum_{j=1}^{J} \kappa(\nu)_j \, \rho_{a_j} \int_{z_{l_-}}^{z_{l_+}} \tau(\nu, z, z_{l_+}) \, dz = B(\nu, T_l) \left[1 - \tau(\nu)_l \right] \tag{29}$$

A step-wise algorithm is then used to calculate the radiance, layer-by-layer, along the ray path through the atmosphere, such that the radiance at the furthest boundary of the lth layer is,

$$I(\nu)_l = I(\nu)_{l-1}\,\tau(\nu)_l \;+\; E(\nu)_l \tag{30}$$

3.3.2.5 Integrated radiance. The integrated radiance, L, over the spectral passband, $\Delta\nu$, for a channel with a spectral filter function, $f(\nu)$, is,

$$L = \int_{\Delta\nu} f(\nu)\,I(\nu)\,d\nu \tag{31}$$

3.3.3 Line-by-Line (LBL) Calculations

The line-by-line code GENLN2 is used as the standard benchmark and as a tool to generate absorption coefficient databases on which the faster forward models are based. The line-by-line calculation involves calculating transmittances over the spectral range of interest in wavenumber space for each gas in several atmospheric layers. The simplest procedure is to choose a wavenumber grid fine enough that the narrowest line is adequately sampled, typically $0.0005\ \text{cm}^{-1}$. Then for each line i of path gas j taken in turn, the monochromatic absorption is calculated at each grid point over the entire wavenumber range. The absorption coefficient at a wavenumber ν can be written as the sum over the absorption contributions from all lines i in the spectral range,

$$\kappa(\nu)_j \;=\; \sum_{all\ lines\ i} S_{ij}\,g(\nu,\nu_i)_j \tag{32}$$

Here, S_{ij} is the strength of line i adjusted to the conditions of path j and $g(\nu,\nu_i)_j$ is the line shape function for line i.

GENLN2 performs a two stage spectral calculation for regions close to, and far from, line center, and there is a full treatment of line wings and of lines lying outside the spectral range of immediate interest. The spectral interval of interest is first divided into wide meshes, each with a typical width of $1\ \text{cm}^{-1}$. Each wide mesh is then sub-divided to give the high-resolution fine wavenumber grid. This grid spacing is chosen so as to adequately sample Doppler-broadened lines in the upper atmosphere. The far line wing and continuum absorption, which change slowly with frequency, are calculated at three points within each wide mesh interval and then interpolated onto the fine grid. A line cutoff is used which terminates the calculations $25\ \text{cm}^{-1}$ from line center. The calculation of spectral line absorption close to line center, which changes rapidly with frequency, takes place directly on the fine wavenumber grid. The full effect of overlapping spectral lines within the same band and with other bands is included.

3.3.4 Forward Model Tabulated Data

It is essential to have forward models that execute much faster than LBL code even for the intermediate stages in the development of retrieval algorithms for HIRDLS. The most time consuming part of the atmospheric radiative transfer problem is the determination of the spectral transmittance. A substantial increase in speed can be achieved by using pre-calculated data, consisting of an absorption coefficient database calculated off-line using LBL code. In the following we describe three types of pre-calculated data used for HIRDLS.

3.3.4.1 Logarithmic optical depth quadratic coefficient table. This is designed to provide a close approximation to the LBL code accuracy and has a fixed atmospheric layering scheme. GENLN2 is used to calculate the monochromatic layer optical depth (spectral resolution $0.0005\ \text{cm}^{-1}$) for each of the gases contributing to the emission within a particular HIRDLS channel corresponding to a chosen reference atmosphere. For a gas, g, within a layer, l, at tangent pressure, p_h, defining a line-of-sight coordinate, x, the layer optical depth, $\chi_g^0(p_h, x, \nu)$ is calculated using LBL for the reference layer temperature, $T^0(p_h, x)$. The process is twice repeated for the same atmospheric gas reference profile, but with the temperature artificially changed to $T^0(p_h, x) + \Delta T^0$ and

$T^0(p_h, x) - \Delta T^0$, where $\Delta T^0 = 50$ K and spans the likely temperature variation within a layer for realistic atmospheres. A quadratic fit is made to the variation in $\ln \chi_g^0$ with temperature and the resulting coefficients, $a_{gi}(p_h, x, \nu)$, are tabulated along with the reference layer temperature and gas absorber column amount. Hence, for an arbitrary temperature, $T(p_h, x)$, and absorber amount, $u_g(p_h, x)$, in the atmospheric layer specified by coordinates (p_h, x), we have,

$$\chi_g(p_h, x, \nu) = \frac{u_g(p_h, x)}{u_g^0(p_h, x)} \exp[a_{g0}(p_h, x, \nu) + a_{g1}(p_h, x, \nu)\Delta T + a_{g2}(p_h, x, \nu)\Delta T^2] \tag{33}$$

where

$$\Delta T = T(p_h, x) - T^0(p_h, x) \tag{34}$$

Hence, the transmittance of the layer is,

$$\tau(p_h, x, \nu) = \exp(-\chi) \quad \text{where} \quad \chi = \sum_g \chi_g(p_h, x, \nu) \tag{35}$$

3.3.4.2 Absorption coefficient table. The monochromatic absorption coefficient table is calculated by LBL for a set of atmospheric paths covering the expected range of pressures and temperatures encountered in the atmosphere (spectral resolution 0.0005 cm^{-1}).

For each gas, g, contributing to the emission within a HIRDLS channel we calculate the absorption coefficient, $\kappa_g(\ln p_t, T_t, \nu)$ $[m^2 mol^{-1}]$, using a LBL calculation for an appropriate tabulation of parameters $(\ln p_t, T_t, \nu)$. The optical depth for an arbitrary atmospheric layer pressure and temperature, (p, T), and absorber amount, u_g, is given by,

$$\chi_g(\ln p, T, \nu) = u_g \times INTERPOLATE[\kappa_g(\ln p_t, T_t, \nu), \ln p, T] \tag{36}$$

Hence, the transmittance of the layer is,

$$\tau(\ln p, T, \nu) = \exp(-\chi) \quad \text{where} \quad \chi = \sum_g \chi_g(\ln p, T, \nu) \tag{37}$$

The interpolation scheme may be one of linear, polynomial, or cubic-spline according to the desired accuracy. Some experimentation is necessary to evaluate the appropriate number of tabulated points for pressure and temperature. This method requires smaller storage requirements than the quadratic coefficient tabulation and will be faster to execute.

3.3.4.3 Band-averaged transmittance table. The band-averaged transmittance for each gas contributing to the emission in a HIRDLS channel is calculated for a tabulation of pressure, temperature and absorber amounts $(\ln p_t, T_t, \ln u_t)$ using,

$$\tau_g(\ln p_t, T_t, \ln u_t) = \frac{\int_{\Delta\nu} f(\nu) \exp[-\kappa_g(\ln p_t, T_t, \nu) \, u_t] d\nu}{\int_{\Delta\nu} f(\nu) d\nu} \tag{38}$$

where $\kappa_g(\ln p_t, T_t, \nu)$ is the gas absorption coefficient calculated by using LBL (see Section 3.3.4.2) and $f(\nu)$ is the spectral filter function over the channel passband $\Delta\nu$.

The transmittance is calculated for a Curtis-Godson path absorber amount and absorber weighted temperature and pressure by interpolation. The multiplicative property of band transmittances [*Goody and Yung* (1989)] assumes that spectra of individual gases are not correlated within the radiometer pass band and it may be necessary

to subdivide the spectral interval to reduce this source of error. The treatment of inhomogeneous path transmittances and the applications to limb-sounding, including the calculation of weighting functions, is discussed in detail by Marks and Rodgers (1993). This method is less accurate than the others discussed above, but it offers a greater speed of execution and the tabulation requires far less storage. It will be useful in obtaining an approximate retrieval solution which may be used as the starting point for a more accurate analysis.

3.3.5 Parameterized Models

Work is underway on the development of a fast forward model for HIRDLS that will form part of the operational retrieval algorithm. Fast models generally rely on a parameterization of the radiative transfer problem that avoids the necessity of performing time consuming line-by-line calculations or the subsequent integration of radiance in frequency over the instrument channel filter. The required run time is several orders of magnitude faster than that of a LBL model although this comes with an associated loss in accuracy. Several fast model approaches are being considered that might meet the operational requirements while keeping the errors associated with the parameterization at an acceptable level. These include a fast regression scheme based on the OPTRAN5 work of McMillin *et al.*(1995) that has recently proved useful in the development of the fast forward model for the EOS-TERRA/MOPITT instrument [*Edwards et al., in preparation*]. We are also performing studies to investigate the applicability of a new modified form of the correlated-k distribution technique [*Lacis and Oinas* (1991)].

3.4 Mathematical Description of the Retrieval Algorithm

In the following description it is assumed that the finite field of view of HIRDLS has been deconvolved from the radiance measurements as described in section 3.2, i.e. the radiances are pre-processed to approximate a δ-function field of view.

3.4.1 Retrieval Overview

The aim of any physical retrieval algorithm is to obtain profiles of the atmospheric constituents (contained in the "state vector") for which the radiative transfer model ("forward model") predicts synthesized radiances which are consistent with the measured radiances ("measurement vector") and the a priori information.

3.4.1.1 Measurement vector and error covariance. The measurement vector, $\mathbf{y}$, has m elements consisting of the vertical profiles of calibrated Level-1 radiances for the channels selected for the retrieval,

$$\mathbf{y} = \{y_c(z_{l_c})\} \tag{39}$$

where the indices, l_c, specify the altitudes, z_{l_c}, to be used for a channel, c. The instrument noise, $\boldsymbol{\epsilon_y}$, is assumed to be uncorrelated between channels (i.e. no cross-talk) and to have zero mean. The measurement error covariance, $\mathbf{S_y}$, is an $(m \times m)$ matrix, where the diagonal elements are equal to the variances of the instrument noise, σ_y^2, and the off-diagonal elements are zero,

$$\mathbf{S_y} = \mathcal{E}\left\{\boldsymbol{\epsilon_y}\boldsymbol{\epsilon_y}^{\mathrm{T}}\right\}; \quad S_y(i,j) = \left\{ \begin{array}{cc} \sigma_y^2(i) & \text{if } i = j, \\ 0 & \text{if } i \neq j \end{array} \right. \tag{40}$$

3.4.1.2 State vector. The state vector, $\mathbf{x}$, has n elements consisting of the quantities to be retrieved e.g. temperature profile, reference pressure and/or constituent mixing ratio profiles at the required altitude ranges,

$$\mathbf{x} = \{x_q(z_{l_q})\} \tag{41}$$

where the indices, l_q, specify the altitudes, z_{l_q}, to be used for a retrieved quantity, x_q.

3.4.1.3   A priori vector and covariance.   The a priori data give an independent estimate of the state of the atmosphere and its expected variability. The influence of the a priori on the retrieval is to provide stabilization against the possible gross amplification of noise associated with direct inversion of the measurements. All the quantities in the state vector require a priori data. The a priori vector, $\mathbf{x_a}$, has n elements with the same structure as the state vector,

$$\mathbf{x_a} = \left\{ x_{q_a}(z_{l_q}) \right\} \tag{42}$$

where the same indices as in Eqn 41, l_q, specify the altitudes, z, to be used for an a priori quantity, x_{q_a}. The a priori covariance, $\mathbf{S_{x_a}}$, is an $(n \times n)$ matrix, where the diagonal elements are the variances and the off-diagonal elements represent the interlevel correlations.

3.4.1.4   Forward model.   We define the act of measurement to be,

$$\mathbf{y} = f(\mathbf{x}, \mathbf{b}) + \boldsymbol{\epsilon_y} \tag{43}$$

where f is identified as the "forward function" and represents the physics of the measurement including the characterization of the instrument and the radiative transfer process. The true atmospheric state is described by the vector $\mathbf{x}$ and $\mathbf{b}$ is a vector of "forward function parameters" which are quantities that affect the radiative transfer but which are not being retrieved. The error term is given by the vector $\boldsymbol{\epsilon_y}$ with covariance matrix $\mathbf{S_y}$ and includes measurement noise. The forward model, $\mathbf{f}$, is used to calculate synthesized radiances, $\hat{\mathbf{y}}$, and can be represented by,

$$\hat{\mathbf{y}} = \mathbf{f}(\hat{\mathbf{x}}, \hat{\mathbf{b}}) \tag{44}$$

where $\hat{\mathbf{x}}$ and $\hat{\mathbf{b}}$ are estimation vectors for the state and model parameters, respectively. This represents an approximation to the true forward transfer process and the resulting forward model error is discussed in Section 3.5.1.

3.4.1.5   Inverse model.   The inverse model, I, relates the retrieved state to the true state and can be represented formally by,

$$\hat{\mathbf{x}} = I(\mathbf{y}, \hat{\mathbf{b}}, \mathbf{x_a}, \mathbf{c}) \tag{45}$$

where $\mathbf{x_a}$ is a vector of a priori data corresponding to the state vector and $\mathbf{c}$ are other data not explicitly included in the forward model e.g. the starting guess vector for $\mathbf{x}$.

3.4.1.6   Weighting functions.   The state vector is defined on a geometric altitude grid and the radiances are labelled according to the same grid. Then the definition of a weighting function is :

$$K_{hl} = \frac{dR_h}{dx_l} \tag{46}$$

where dR_h is the change in radiance at the satellite, originating along the ray path labelled by the geometric altitude, h, due to a change in the quantity, dx_l, at the geometric altitude, l.

3.4.1.7   Solution.   The process we use to obtain a solution for $\mathbf{x}$ is an optimal estimation algorithm [*Rodgers* (1976), *Rodgers* (1990)]. The scalar cost function, constructed assuming Gaussian errors for both the a priori estimate and measurements, is given by,

$$\Phi(\mathbf{x}) = (\mathbf{x} - \mathbf{x_a})^{\mathrm{T}} \mathbf{S_{x_a}^{-1}}(\mathbf{x} - \mathbf{x_a}) + (\mathbf{y} - \mathbf{f}(\mathbf{x}))^{\mathrm{T}} \mathbf{S_y^{-1}}(\mathbf{y} - \mathbf{f}(\mathbf{x})) \tag{47}$$

The first term of Eqn 47 is a penalty function which constrains the solution to the a priori state with a weighting dependent on the a priori covariances. The second term is the familiar χ^2-statistic which evaluates the "distance" between the measured and the synthesized radiances with a weighting dependent on the measurement error covariances. The maximum likelihood solution is obtained by minimizing the cost function with respect to $\mathbf{x}$,

$$\nabla_{\mathbf{x}}\Phi(\mathbf{x}) = 0 = \mathbf{S_{x_a}^{-1}}(\mathbf{x} - \mathbf{x_a}) - \mathbf{K}^{\mathrm{T}}\mathbf{S_y^{-1}}(\mathbf{y} - \mathbf{f}(\mathbf{x})) \tag{48}$$

where

$$\mathbf{K} = \frac{\partial \mathbf{f}(\mathbf{x})}{\partial \mathbf{x}} \tag{49}$$

is the weighting function matrix $(m \times n)$ which represents the sensitivity of the forward model to the retrieved quantities. Rearranging Eqn 48 yields the following nonlinear equation for $\hat{\mathbf{x}}$,

$$\hat{\mathbf{x}} = \mathbf{x_a} + \mathbf{S_{x_a}}\mathbf{K}^{\mathrm{T}}\mathbf{S_y^{-1}}(\mathbf{y} - \mathbf{f}(\hat{\mathbf{x}})) \tag{50}$$

We seek an efficient numerical method of obtaining the solution to Eqn 50 and a Newtonian iteration scheme may be employed if the system is only moderately non-linear and the initial guess value of the state vector is in the vicinity of the solution,

$$\mathbf{x}^{(i+1)} = \mathbf{x}^{(i)} - [\mathbf{H}(\mathbf{x}^{(i)})]^{-1}\nabla_{\mathbf{x}}\Phi(\mathbf{x}^{(i)}) \tag{51}$$

where the second derivative of the cost function is known as the Hessian matrix,

$$\mathbf{H}(\mathbf{x}) = \nabla_{\mathbf{x}}^2\Phi(\mathbf{x}) \approx \mathbf{S_{x_a}^{-1}} + \mathbf{K}^{\mathrm{T}}\mathbf{S_y^{-1}}\mathbf{K} \tag{52}$$

and the iteration scheme is called the inverse Hessian method. If $\Phi(\mathbf{x})$ is exactly a quadratic form then Eqn 51 gives the solution in one step.

On substituting Eqns 48 and 52 into Eqn 51 we obtain the iteration equation for $\hat{\mathbf{x}}$, where $\mathbf{x}^{(i)} \rightarrow \hat{\mathbf{x}}$ as the iteration proceeds,

$$\mathbf{x}^{(i+1)} = \mathbf{x}^{(i)} + (\mathbf{S_{x_a}^{-1}} + \mathbf{K}^{\mathrm{T}}\mathbf{S_y^{-1}}\mathbf{K})^{-1}(\mathbf{K}^{\mathrm{T}}\mathbf{S_y^{-1}}[\mathbf{y} - \mathbf{f}(\mathbf{x}^{(i)})] - \mathbf{S_{x_a}^{-1}}(\mathbf{x}^{(i)} - \mathbf{x_a})) \tag{53}$$

The solution covariance including the a priori and measurement noise terms is given by (see Section 3.5.3.5),

$$\mathbf{S_x} = (\mathbf{S_{x_a}^{-1}} + \mathbf{K}^{\mathrm{T}}\mathbf{S_y^{-1}}\mathbf{K})^{-1} \tag{54}$$

However, we must consider situations where an initial estimate of the state vector is so far from the solution that a quadratic hypersurface is not a good approximation to the shape of the cost function. The simple method of steepest descent is then more appropriate,

$$\mathbf{x}^{(i+1)} = \mathbf{x}^{(i)} - \gamma^{-1} \nabla_{\mathbf{x}} \Phi(\mathbf{x}^{(i)}) \tag{55}$$

where γ determines the step size in the search for the minimum.

The Marquardt-Levenberg method combines the inverse Hessian and steepest descent approaches,

$$\mathbf{x}^{(i+1)} = \mathbf{x}^{(i)} - [\mathbf{H}(\mathbf{x}^{(i)}) + \gamma \mathbf{I}_n]^{-1} \nabla_{\mathbf{x}} \Phi(\mathbf{x}^{(i)}) \tag{56}$$

The value of γ controls the search strategy, for $\gamma \to 0$ the inverse Hessian method dominates and for $\gamma \to \infty$ the steepest descent dominates with a small step size. The prescription for changing the value of γ is dependent on the convergence behaviour. If $\Phi(\mathbf{x}^{(n+1)}) > \Phi(\mathbf{x}^{(n)})$ then reject $\mathbf{x}^{(n+1)}$ and increase γ, whereas if $\Phi(\mathbf{x}^{(n+1)}) < \Phi(\mathbf{x}^{(n)})$ then accept $\mathbf{x}^{(n+1)}$ and decrease γ. In general, the search procedure starts out as a slow steepest descent method and, as the iteration proceeds and the solution is approached more closely, the search turns to the faster inverse Hessian method.

3.4.1.8 Convergence criterion. The iteration process must be stopped at a suitable point which prevents (i) over-running the iteration, resulting in time-wasting computational effort, and (ii) under-running the iteration and therefore not converging on an answer lying within a negligible difference from the optimal solution. A practical convergence test is to stop the iteration when the maximum difference between the last two iterates for all elements of the state vector is smaller than a pre-defined tolerance, ϵ, i.e. $\mid x^{(n)} - x^{(n-1)} \mid < \epsilon$. An upper limit must obviously be set on the maximum number of iterations allowed to curtail "runaway" retrievals which never converge.

3.4.1.9 Retrieval quality control. If the retrieval converges then a number of tests are carried out including :

(i) Consistency of the retrieval with the measurements and a priori data. The standard χ^2-test is applied to Eqn 47 to determine whether there is a statistically significant deviation which indicates an abnormally poor fit. This should follow a χ^2 distribution with m degrees of freedom since there are $n + m$ measurements (the a priori data are considered as virtual measurements) to which n parameters have been fitted. The retrieval is accepted as successful if the value of the χ^2-statistic satisfies, for example, the 99.9 % confidence level.

(ii) Consistency of the retrieval with the a priori data.

The retrieved state vector is compared to the a priori state vector. A poor fit in this case may be indicative of an anomalous atmospheric event in progress i.e. the atmospheric variability has exceed that specified by the a priori covariance.

It is useful to record and examine the χ^2-distribution for a complete set of retrievals accumulated over a processing period.

3.5 Retrieval Characterization and Error Analysis

In this section we discuss (a) the sensitivity of the retrieval to the true state (characterization) and (b) how the various error sources are propagated into the retrieved product (error analysis). This approach to diagnostic information allows one to quantify the effect of the a priori state on the retrieved state and to decompose the various sources of error so that the effect of each on the retrieved state can be appreciated.

3.5.1 Characterization

The relationship of the retrieved state to the true state is given by the inverse model in Eqn 45. We must approximate the true forward transfer function in Eqn 43 by replacing it with the forward model in Eqn 44 and including a "forward model error" term, $\Delta \mathbf{f}(\mathbf{x}, \mathbf{b})$ to represent the resulting uncertainty,

$$\mathbf{y} = \mathbf{f}(\mathbf{x}, \mathbf{b}) + \Delta \mathbf{f}(\mathbf{x}, \mathbf{b}) + \boldsymbol{\epsilon}_y \tag{57}$$

$$\Delta \mathbf{f}(\mathbf{x}, \mathbf{b}) = f(\mathbf{x}, \mathbf{b}) - \mathbf{f}(\mathbf{x}, \mathbf{b}) \tag{58}$$

Introducing the forward model error term into the retrieval allows for the fact that the measurements may be known to a much higher accuracy than the expected accuracy of the forward model. The inverse and forward models in Eqns 45 and 44 can be linearized about the a priori state, $\mathbf{x_a}$, and model parameter estimate, $\hat{\mathbf{b}}$, to give,

$$\hat{\mathbf{x}} - \mathbf{x_a} = [I(\mathbf{y_a}, \hat{\mathbf{b}}, \mathbf{x_a}, \mathbf{c}) - \mathbf{x_a}] + \mathbf{D_y}(\mathbf{y} - \hat{\mathbf{y}}_a)$$

$$\mathbf{y} - \hat{\mathbf{y}}_a = \mathbf{K}(\mathbf{x} - \mathbf{x_a}) + \mathbf{K_b}(\mathbf{b} - \hat{\mathbf{b}}) + \Delta \mathbf{f}(\mathbf{x}, \mathbf{b}) + \boldsymbol{\epsilon}_y \tag{59}$$

where

$$\hat{\mathbf{y}}_a = \mathbf{f}(\mathbf{x_a}, \hat{\mathbf{b}}) \tag{60}$$

is the vector of synthesized radiances corresponding to the a priori state,

$$\mathbf{D_y} = \frac{\partial \hat{\mathbf{x}}}{\partial \mathbf{y}} \tag{61}$$

is the contribution function matrix (sensitivity of the retrieval to the measurement vector),

$$\mathbf{K} = \frac{\partial \mathbf{f}}{\partial \mathbf{x}} \tag{62}$$

is the weighting function matrix discussed in Appendix A (sensitivity of the forward model radiances to the state vector), and

$$\mathbf{K_b} = \frac{\partial \mathbf{f}}{\partial \mathbf{b}} \tag{63}$$

is the sensitivity of the forward model radiances to the forward model parameters.

The term in square brackets in Eqn 59 measures the consistency of the inversion process and is zero for a properly designed retrieval scheme i.e. in the absence of noise the a priori state must be reproduced exactly, $\hat{\mathbf{x}} = \mathbf{x_a}$, if the retrieval is made to operate on the measurement vector defined by $\mathbf{y} = \hat{\mathbf{y}}_a$.

We can rearrange Eqn 59 to illustrate that the retrieved state can be expressed as a weighted mean of the true and a priori states and the noise contribution,

$$\hat{\mathbf{x}} = \mathbf{A}\mathbf{x} + (\mathbf{I} - \mathbf{A})\mathbf{x_a} + \mathbf{D_y}[\mathbf{K_b}(\mathbf{b} - \hat{\mathbf{b}}) + \Delta \mathbf{f}(\mathbf{x}, \mathbf{b}) + \boldsymbol{\epsilon}_y] \tag{64}$$

where $\mathbf{I}$ is the unit vector,

$$\mathbf{D_a} = \mathbf{I} - \mathbf{A} = \frac{\partial \hat{\mathbf{x}}}{\partial \mathbf{x_a}} \tag{65}$$

is the a priori contribution function matrix (sensitivity of the retrieval to the a priori vector), and

$$\mathbf{A} = \mathbf{D_y}\mathbf{K} = \frac{\partial \hat{\mathbf{x}}}{\partial \mathbf{x}} \tag{66}$$

is the averaging kernel matrix which represents the sensitivity of the retrieved state to perturbations of the true state. Ideally, $\mathbf{A} = \mathbf{I}$ so that changes at one level in the real profile are only observed at the same level in the retrieved profile. The rows of the matrix $\mathbf{A}$ indicate how the retrieval smoothes the true profile, and the width of these peaked functions can be interpreted as a qualitative measure of the vertical resolution intrinsic to the inversion process. The sum of the matrix rows or the "averaging kernel area" is a measure of the information obtained from the measurements rather than from the a priori. Values close to unity indicate that the retrieval is dominated by measurement information.

3.5.2 Matrix Derivatives.

The required matrix derivatives may be obtained by numerically perturbing the forward model and retrieval method or by analytic differentiation of the appropriate equations. The perturbation technique is slow as the number of operations required to calculate a row of the weighting function matrix scales as $O(N^2)$ where N is the number of profile levels and hence the analytic method is preferred where this is feasible.

3.5.2.1 Weighting functions. The weighting functions, $\mathbf{K} = \frac{\partial \mathbf{f}}{\partial \mathbf{x}}$, are required during the iterative retrieval process and constraints on processing speed require that either they be available as tabulated data or can be computed as analytical derivatives. The analytical derivation of weighting functions is discussed in Appendix A.

3.5.2.2 Model parameter derivatives. The model parameter derivatives, $\mathbf{K_b} = \frac{\partial \mathbf{f}}{\partial \mathbf{b}}$, are required only in the error analysis as part of the diagnostics. They will be calculated by a perturbation method.

3.5.2.3 Contribution function matrix. Differentiation of Eqn 50 with respect to $\mathbf{y}$ yields,

$$\mathbf{D_y} = \frac{\partial \hat{\mathbf{x}}}{\partial \mathbf{y}} = \left(\mathbf{S_{x_a}^{-1}} + \mathbf{K^T}\mathbf{S_y^{-1}}\mathbf{K}\right)^{-1}\mathbf{K^T}\mathbf{S_y^{-1}} \tag{67}$$

3.5.2.4 A Priori contribution function matrix. Differentiation of Eqn 50 with respect to $\mathbf{x_a}$ yields,

$$\mathbf{D_a} = \frac{\partial \hat{\mathbf{x}}}{\partial \mathbf{x_a}} = \left(\mathbf{S_{x_a}^{-1}} + \mathbf{K^T}\mathbf{S_y^{-1}}\mathbf{K}\right)^{-1}\mathbf{S_{x_a}^{-1}} \tag{68}$$

Additionally, differentiation of Eqn 64 with respect to $\mathbf{x_a}$ yields,

$$\mathbf{D_a} = \mathbf{I} - \mathbf{A} \tag{69}$$

3.5.2.5 Averaging kernel matrix. Differentiation of Eqn 50 with respect to $\mathbf{x}$ yields,

$$\mathbf{A} = \frac{\partial \hat{\mathbf{x}}}{\partial \mathbf{x}} = \left(\mathbf{S_{x_a}^{-1}} + \mathbf{K^T}\mathbf{S_y^{-1}}\mathbf{K}\right)^{-1}\mathbf{K^T}\mathbf{S_y^{-1}}\mathbf{K} = (\mathbf{I} - \mathbf{D_a}) = \mathbf{D_y}\mathbf{K} \tag{70}$$

3.5.3 Retrieval Error Analysis

We can rearrange the terms in Eqn 59 to yield,

$$
\begin{aligned}
\hat{\mathbf{x}} - \mathbf{x} = (\mathbf{A} - \mathbf{I})(\mathbf{x} - \mathbf{x_a}) &\quad \ldots \text{ smoothing error} \ldots \; \epsilon_s \\
+ \mathbf{D_y}\mathbf{K_b}(\mathbf{b} - \hat{\mathbf{b}}) &\quad \ldots \text{ model parameter error} \ldots \; \epsilon_b \\
+ \mathbf{D_y}\Delta\mathbf{f}(\mathbf{x}, \mathbf{b}) &\quad \ldots \text{ forward model error} \ldots \; \epsilon_f \\
+ \mathbf{D_y}\epsilon_y &\quad \ldots \text{ retrieval noise} \ldots \; \epsilon_n
\end{aligned}
\tag{71}
$$

3.5.3.1 Smoothing error. The smoothing error (a priori error) is given by

$$\epsilon_s = (\mathbf{A} - \mathbf{I})(\mathbf{x} - \mathbf{x_a}) \tag{72}$$

However, because the true state is unknown the smoothing error can only be estimated from a representative ensemble of states about a mean state and so the error covariance is written as,

$$\mathbf{S}_{\epsilon_s} = \mathcal{E}\left\{\epsilon_s \epsilon_s^{\mathrm{T}}\right\} = (\mathbf{A} - \mathbf{I})\mathbf{S_e}(\mathbf{A} - \mathbf{I})^{\mathrm{T}} \tag{73}$$

where $\mathbf{S_e}$ is a covariance matrix which represents the statistics of an ensemble of states about the true state. In the case where the a priori state is a genuine representation of the variability of the true state at all spatial scales (e.g. derived from previous measurements or from a realistic atmospheric model) then we may set $\mathbf{S_e} = \mathbf{S_{x_a}}$. On the other hand if the a priori state is invented simply to provide a useful constraint for the retrieval it will not contain the fine structure necessary to derive an estimate of the smoothing error. In the latter case [*Rodgers, in preparation*] recommends an alternative approach in which the retrieval is regarded as an estimate of a smoothed state.

3.5.3.2 Model parameter error. The model parameter error is,

$$\epsilon_b = \mathbf{D_y}\mathbf{K_b}(\mathbf{b} - \hat{\mathbf{b}}) \tag{74}$$

and the retrieval error covariance contribution is,

$$\mathbf{S}_{\epsilon_b} = \mathcal{E}\left\{\epsilon_b \epsilon_b^{\mathrm{T}}\right\} = \mathbf{D_y}\mathbf{K_b}\mathbf{S_b}\mathbf{K_b^{\mathrm{T}}}\mathbf{D_y^{\mathrm{T}}} \tag{75}$$

where $\mathbf{S_b} = \mathcal{E}\left\{(\mathbf{b} - \hat{\mathbf{b}})(\mathbf{b} - \hat{\mathbf{b}})^{\mathrm{T}}\right\}$ is the error covariance of the model parameters, $\mathbf{b}$.

3.5.3.3 Forward model error. The forward model error is,

$$\epsilon_f = \mathbf{D_y}\Delta\mathbf{f} \tag{76}$$

and the retrieval error covariance contribution is,

$$\mathbf{S}_{\epsilon_f} = \mathcal{E}\left\{\epsilon_f \epsilon_f^{\mathrm{T}}\right\} = \mathbf{D_y}\mathbf{S_f}\mathbf{D_y^{\mathrm{T}}} \tag{77}$$

where $\mathbf{S_f} = \mathcal{E}\left\{\Delta f \Delta f^{\mathrm{T}}\right\}$ is the error covariance of f. An estimate of the error in the operational forward model will be obtained by comparison with line-by-line models.

3.5.3.4 Retrieval noise. The retrieval noise is given by

$$\epsilon_n = \mathbf{D_y}\epsilon_y \tag{78}$$

and the retrieval error covariance contribution is,

$$\mathbf{S}_{\epsilon_n} = \mathcal{E}\left\{\epsilon_n \epsilon_n^{\mathrm{T}}\right\} = \mathbf{D_y}\mathbf{S_y}\mathbf{D_y^{\mathrm{T}}} \tag{79}$$

3.5.3.5 Solution covariance. The full solution covariance is given by the sum of the error covariance matrices,

$$\begin{aligned}
\mathbf{S_x} &= \mathbf{S}_{\epsilon_n} + \mathbf{S}_{\epsilon_s} + \mathbf{S}_{\epsilon_b} + \mathbf{S}_{\epsilon_f} \\
&= \mathbf{D_y}\mathbf{S_y}\mathbf{D_y^{\mathrm{T}}} + \mathbf{D_a}\mathbf{S_{x_a}}\mathbf{D_a^{\mathrm{T}}} + \mathbf{D_y}\mathbf{K_b}\mathbf{S_b}\mathbf{K_b^{\mathrm{T}}}\mathbf{D_b^{\mathrm{T}}} + \mathbf{D_y}\mathbf{S_f}\mathbf{D_y^{\mathrm{T}}} \\
&= \left(\mathbf{S_{x_a}^{-1}} + \mathbf{K^{\mathrm{T}}}\mathbf{S_y^{-1}}\mathbf{K}\right)^{-1} + \mathbf{D_y}\mathbf{K_b}\mathbf{S_b}\mathbf{K_b^{\mathrm{T}}}\mathbf{D_b^{\mathrm{T}}} + \mathbf{D_y}\mathbf{S_f}\mathbf{D_y^{\mathrm{T}}}
\end{aligned} \tag{80}$$

3.5.3.6 Pre-launch retrieval testing and error analysis. The pre-launch retrieval testing consists of making simulated data retrievals corresponding to expected atmospheric conditions which are derived either from model data or previous measurements. The error analyses will incorporate estimates of the error sources shown in Table 4 obtained from instrument calibration and test data (Section 6).

Random errors include instrument, detector and electronic noise, which we consider together to form the radiometric measurement noise. These are quoted as the noise equivalent radiances (NER) in Table 2. Line of sight pointing jitter also makes an important radiometric random noise contribution.

Systematic errors occur due to the instrument model (field of view response, detector misalignment, spectral filter response, calibration gain and off-set), ancillary data (climatological contaminant species abundances), spectroscopy (line shape, line mixing and continuum emission) and the forward model (transmittance approximations, retrieved temperature/pressure values).

3.5.3.7 Post-launch error analysis. The post-launch error analysis is concerned with internal data validation (Section 6) and is able to make use of the information from in-flight instrument performance studies e.g. estimates of uncorrected scan dependent stray radiances from satellite pitch-up events, time-series of space and black-body views, and profile-to-profile / orbit-to-orbit repeatability measurements.

Retrieval Error Term	Error Source	
Smoothing error	Intrinsic resolution	
Forward model parameter error	Ancilliary data error	Contaminant species
	Instrument error	Calibration
		Field-of-view
		Pointing jitter
		Detector misalignment
		Spectral filter
	Spectroscopy error	Line shape, line mixing, continuum
Forward model error	Temperature/pressure error	
	Approximations	
Measurement error	Instrument noise	

Table 4: Error terms and sources.

3.5.4 Level-2 Product Errors

The reporting of correlated errors in the Level-2 product poses something of a problem. The diagonal terms of a covariance matrix are the familiar error variances which are normally reported in the retrieved product as standard deviations ($1\ \sigma$). However, these provide no information on the nature of the correlated errors. Additional data quality indicators should be available in the Level-2 product to allow the assessment of the influence of the a priori on the retrieved quantity. This could be achieved in a similar way to that used by some UARS instrument teams whereby a negative sign in the error value is used to flag the altitudes where most of the information comes from the a priori. Alternatively, the information could be supplied as a separate profile consisting of the areas of the averaging kernels corresponding to each given altitude as described by Marks and Rodgers (1993). It is also possible to provide e.g. the significant error patterns along with a diagonal matrix to represent the insignificant ones [*Rodgers* (1990)].

3.6 Retrieval Schemes

The retrieval scheme defines the sequence in which the retrievals are carried out and paramount is the retrieval of temperature and pressure. Table 5 shows a possible configuration for the retrieval of all catalogued Level-2 products. Table 6 provides a key to terminology used in the retrieval/contaminant tables shown in the following

	Target	Contaminants						Channels			
1	T/p	CO_2	O_3	N_2O			Aerosol	2	3	4	5
2	Aerosol	H_2O	N_2O	CO_2	O_3		HNO_3	CH_4	1	6	13	19
3	O_3	CO_2	H_2O	N_2O	CFC12		Aerosol	10	11	12	
4	H_2O	CH_4	O_2				Aerosol	18	20		
5	NO_2	H_2O	CH_4	O_2			Aerosol	21			
6	HNO_3	H_2O	CO_2	O_3			Aerosol	8			
	CFC11							7			
	CFC12							9			
7	N_2O_5	H_2O	CO_2	HNO_3	CF_4		Aerosol	14			
	N_2O							15			
	$ClONO_2$							16			
	CH_4							17			

Table 5: HIRDLS retrieval scheme showing (a) the retrieval sequence 1–7, (b) contaminants, (c) radiance channels and (d) grouping of multiple retrieval products. Two complete passes through the retrieval sequence are required to correct for line of sight gradients (Section 3.6.4).

sections. The target gas(es) is (are) the species to be retrieved from a radiance channel or combination of channels. Contaminants are the species specified as contributing to the emission within a radiance channel but which are not being retrieved at the current retrieval step. These may be fixed gases (denoted by F), or taken from the climatology data (denoted by C), or obtained from data retrieved independently from other radiance channels at an earlier processing stage (denoted by R). In the joint retrieval schemes R* indicates that a retrieval target of one channel is also a contaminant in one or more of the other channels. For all of the schemes the retrieval is a well-posed problem i.e. the number of retrieved products is less than or equal to the number of radiance channels.

The retrieval sequence consists of 7 steps, a two-stage process being used to achieve the line of sight gradient correction (Section 3.6.4). Each product that is retrieved is 3-D gridded and the gridded data used to generate line of sight gradients (Section 3.6.4) which are used in the second pass of the retrieval sequence. R1 and R2 are used to denote contaminants derived from uncorrected and corrected LOS gradient data, respectively. Joint retrievals are specified for the products with significant cross-channel contamination.

Here we only consider the radiance data obtained during a single up or down scan which is pre-processed (Section 3.2) to produce a vertical profile for each channel. The flexibility of the HIRDLS instrumentation allows more complex observation modes and retrieval schemes to be devised in which the horizontal variability along the line of sight may be probed in greater detail.

An overview of the Level-2 retrieval flow is shown in Figure 19. The instrument data input is via the Level-1 product which consists of geolocated and time-stamped vertical profiles of limb radiances. Ancilliary data, such as the climatology data, transmittance data etc. are also required inputs to the Level-2 processor (Section 5).
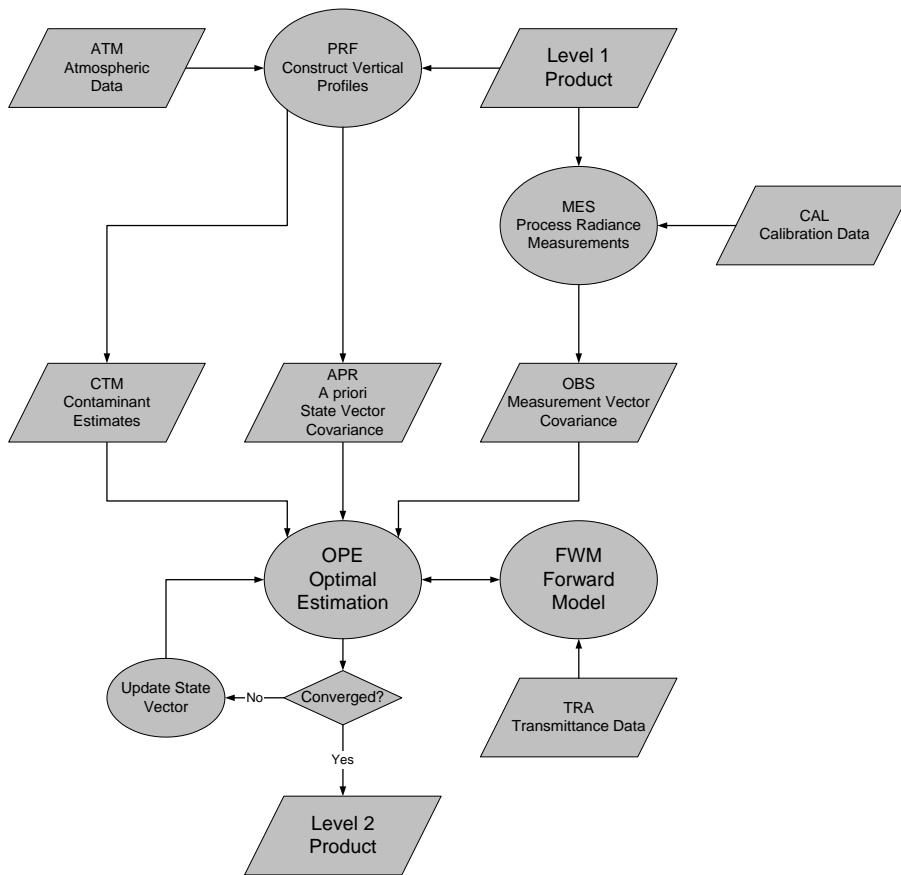
Figure 19: HIRDLS Level-2 retrieval flow. Some intermediate stages and associated input/output operations have been omitted for clarity.

3.6.1 Upper Troposphere.

We have described the baseline retrieval scheme which is in consideration for the engineering version software delivery. In order to retrieve into the upper troposphere, more elaborate schemes involving further grouping of products into joint retrievals is envisaged e.g. temperature/pressure, constituents and aerosol products, since for some contaminants, notably water vapor, the use of climatological values in the initial retrieval step will be unable to capture accurately their rapid increase in concentration and their variable nature in this region. One approach

Target	Channels	Contaminants
Species to be retrieved.	Radiance channel(s)	Contaminant source codes:
		N = not used
		F = fixed gas
		C = climatology
		R1 = retrieved at stage 1 (no LOS gradient correction)
		R2 = retrieved at stage 2 (LOS gradient correction)
		R* = contaminant is also retrieval target

Table 6: Key to the retrieval target/contaminant tables. Contaminants are species specified as contributing to the emission within a radiance channel. They are either taken from a climatology or from data retrieved from other radiance channels at an earlier processing stage. In the joint retrieval schemes an R* indicates that a retrieval target of one channel is also a contaminant in one or more of the other channels. For all of the schemes the retrieval is a well-posed problem i.e. the number of retrieved products is less than or equal to the number of radiance channels.

to this problem is to conduct a first-pass retrieval for the upper troposphere retrieval using optimal onion-peeling starting at the bottom range of the stratospheric vector-vector retrieval. The final stage will employ a complete vector-vector retrieval for upper troposphere and stratosphere combined.

The development of the HIRDLS retrieval scheme for the upper troposphere region is outlined in Table 7.

3.6.2   Climatological Data.

Climatological data are required for each contaminant species in the HIRDLS channels and are conveniently stored as gridded data on standard pressure surfaces. The spatial and temporal gridding resolution depends on the variability of the particular species, i.e. 1-D profiles are adequate for well-mixed gases such as CO_2, but 2-D zonal mean spatial distributions will be required for most species. Some species will only require a single fixed distribution in time, while others will be represented as seasonal or monthly distributions. Diurnally varying species will require special treatment to factor in the change as a function of solar zenith angle or local time as appropriate. These ancilliary data are denoted by C for climatology and F for fixed gases in the retrieval tables.

3.6.3   A priori Data.

The a priori data consist of a profile and covariance matrix for each of the HIRDLS target species. They are required to constrain the retrieval (Section 3.4) and may not necessarily be derived from the climatological data. As discussed in Section 3.5.3.1 the a priori data should be constructed with regard for the atmospheric fine scale variability.

3.6.4   Gridded Data and Line-of-sight Gradients.

Gradients in temperature, pressure and constituent mixing ratios invalidate the assumption of spherical symmetry of the limb-path. The LOS gradient can be represented as $\partial q_l/\partial \psi$ where q_l is the quantity of interest at level, l, and ψ is the LOS great-arc angle. A simple line-of-sight gradient (LOS) correction can be implemented in a two-stage process. An initial pass of the retrieval, without regard to LOS gradients, is used to produce 3-D gridded data. Figure 20 shows how the HIRDLS measurements made in a first retrieval iteration can be used to obtain information of the variation along the line of sight. The LOS central difference gradients are calculated for each profile location and used in the second pass of the retrieval to obtain the required quantities along the LOS i.e. $q_s = q_l + \Delta\psi_s \partial q_l/\partial \psi$, where s is the LOS element index and $\Delta\psi_s$ is the LOS angle between the s and the tangent point. The gridded data will also be used in subsequent retrievals wherever a retrieved product can be used in place of climatology for a contaminant (denoted by R in the retrieval tables).

- Upper Troposphere
  - more variability than in stratosphere
    - climatologies
      - probably inadequate for use as contaminants
      - possibly unable to provide a close enough initial guess
  - Optimal onion-peeling joint retrieval
    - start in lower stratosphere and work down
    - use reference pressure level determined in stratosphere
      - extrapolation from levels above gives initial guess for current level
        - Temperature (02, 03)
        - H_2O (18)
        - N_2O (15)
        - CH_4 (17)
        - O_3 (12)
        - Aerosol (6)
- Overall View
  - Retrieve
    - stratosphere (vector-vector)
    - upper troposphere (onion peeling)
  - Merge upper tropospheric and stratospheric profiles
  - Update initial guess
  - Retrieve
    - stratosphere and upper troposphere (vector-vector)
  - Construct LOS gradients
  - Update initial guess
  - Retrieve
    - stratosphere and upper troposphere (vector-vector)

Table 7: Development of the HIRDLS retrieval scheme for the upper troposphere region. A first pass consisting of an optimal onion peeling retrieval will be performed starting at the bottom range of the stratospheric vector-vector retrievals. The final stage will employ a complete vector-vector retrieval for upper troposphere and stratosphere combined.

3D Gridded Data on Constant Altitude Surfaces

Altitude

State Vector
Location

LOS Direction

Latitude

Longitude

2D Vertical
Cross-
Section
Along LOS

Centre of Radius of
Curvature of Geoid

ψ
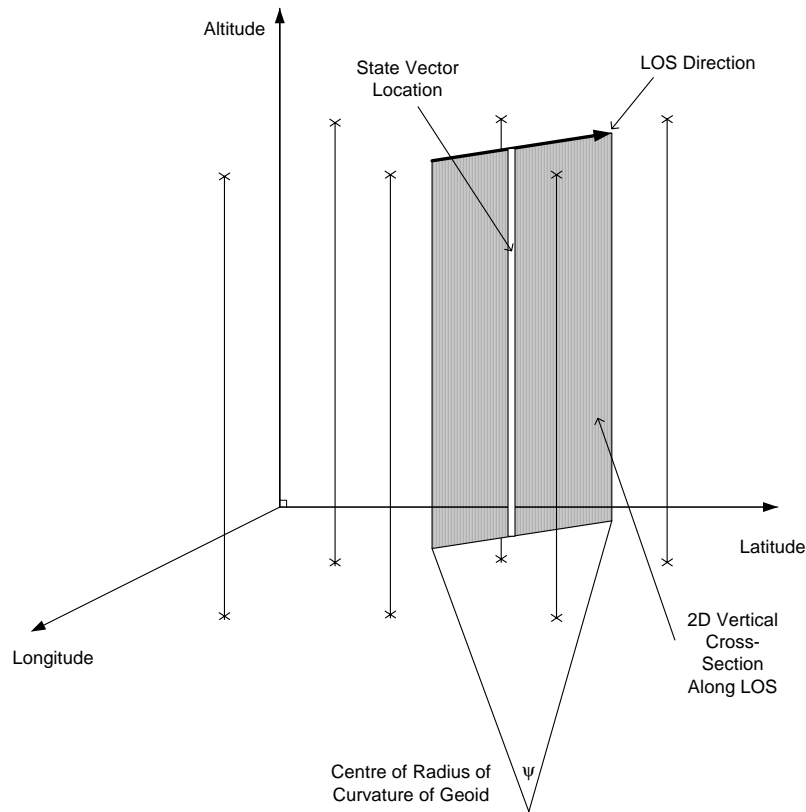
HIRDLS Global mode 5degx5deg spacing will only provide 1st order gradient information along LOS.

Finer resolution modes will generate higher order LOS variation.

3D Gridded Data Fields are interpolated to generate 2D Vertical Cross-Sections Along LOS.

Figure 20: Line of sight gradient information obtained from HIRDLS measurements.

Field	Temporal	Spatial
CO_2	Fixed	1-D Profile
O_3	Monthly	2-D Zonal Mean
H_2O	Monthly	2-D Zonal Mean
NO_2	Monthly, Diurnal	2-D Zonal Mean
CFC11	Monthly	2-D Zonal Mean
HNO_3	Monthly	2-D Zonal Mean
CFC12	Monthly	2-D Zonal Mean
N_2O_5	Monthly, Diurnal	2-D Zonal Mean
N_2O	Monthly	2-D Zonal Mean
$ClONO_2$	Monthly, Diurnal	2-D Zonal Mean
CH_4	Monthly	2-D Zonal Mean
CF_4	Monthly	2-D Zonal Mean
O_2	Fixed	1-D Profile
Aerosol	Background to Volcanic	2-D Zonal Mean
Temperature	Monthly	2-D Zonal Mean
Height	Monthly	2-D Zonal Mean

Table 8: HIRDLS climatological data indicating the required temporal and spatial resolutions.

3.6.5   Multiple Product Retrievals.

The retrieval of multiple products simultaneously from multiple sounding channels is achieved using the generality of the retrieval algorithm which allows the state and measurement vectors to be composed of the concatenation of the individual product profiles and channel radiances, respectively. The measurement error covariance, a priori vector and covariance matrix, and weighting function matrix must also be composed accordingly. The simultaneous retrieval is most effective for the products which have significant contamination in several sounding channels.

3.6.6   Retrieval of Temperature and Pressure

The retrieval of temperature and pressure will be performed jointly on a relative height grid from 4 channels (2,3,4,5) and is summarized in Table 9. The retrieval is designed to be flexible so that in the mesosphere, for example, in place of the fine grid spacing used in the following sections a coarser grid spacing may be used to improve precision. The retrieval does not require absolute pointing knowledge of the line-of-sight. However, the relative altitudes of the retrieval grid must be known to high precision. A reference pressure, $p_0(z_0)$, is chosen corresponding to an altitude surface in the lower stratosphere where the sensitivity, $\partial R/\partial T$, is highest. The temperature is retrieved on the measurement tangent altitudes by making use of the ideal gas equation to relate temperature, T, density, ρ, and pressure, p,

$$p = \frac{\rho}{M_r}RT \tag{81}$$

where R is the gas constant and M_r is the relative molecular mass of air. The hydrostatic equation is integrated to obtain the pressure profile,

$$\ln p(z) = \ln p_0(z_0) + \int_{z_0}^{z} \frac{M_r g(z)}{RT(z)} dz \tag{82}$$

The state vector for this retrieval contains the reference pressure, $\ln p_0(z_0)$, and the temperature profile, $T(z)$.

Target	Channels	Contaminants				
T/p	2	CO_2	O_3	N_2O	Aerosol	
		F	C	C	N	
		F	R1	R1	R1	
		F	R2	R2	R2	
	3	CO_2	O_3	Aerosol		
		F	C	N		
		F	R1	R1		
		F	R2	R2		
	4	CO_2	O_3	Aerosol		
		F	C	N		
		F	R1	R1		
		F	R2	R2		
	5	CO_2	O_3	Aerosol		
		F	C	N		
		F	R1	R1		
		F	R2	R2		

Table 9: Joint retrieval of temperature/pressure from 4 channels (2,3,4,5). A 3-stage process is shown here which uses LOS gradient corrected retrieved contaminants in the final stage. In the contaminant column, the contaminant species are listed for each radiance channel and for each of the 3 processing stages the source of the contaminant data is specified according to the key in Table 6.

All Level-2 products will be interpolated onto a standard pressure surface grid [mb] given by,

$$p(i) = 1000 \times 10^{-i/24} \quad \text{where } 0 \leq \text{i} \leq 144 \text{ is the surface number} \tag{83}$$

A retrieval characterization and error analysis has been performed for the HIRDLS temperature sounding channels (2,3,4,5) for the AFGL tropical atmospheric temperature profile shown in Figure 21. For illustration we have lumped together random error sources apart from the measurement error into a single "forward model error" term consisting of 0.3 % of the channel radiances. Detailed information on individual error components will become available during the HIRDLS calibration and testing phases and these will be used in the final assessments. The diagonal elements of the a priori covariance matrix, $S_{x_a}^{ii}$ were set at $(20\ K)^2$ and the off-diagonal elements were calculated using a $l = 10$ km correlation length,

$$S_{x_a}^{ij} = \sqrt{S_{x_a}^{ii} S_{x_a}^{jj}} \ \exp\bigl(-(z_i - z_j)^2/l^2\bigr) \tag{84}$$

Figures 22–24 show the results of calculations of radiance profiles, weighting functions, averaging kernels and random error contributions. The random error contributions, consisting of the measurement error, forward model error and a priori error, are the square roots of the diagonals of the respective covariance matrices. The forward model error dominates the errors on the retrieved temperature profile from 10–55 km; above 55 km the measurement noise and a priori error have an increasing contribution.
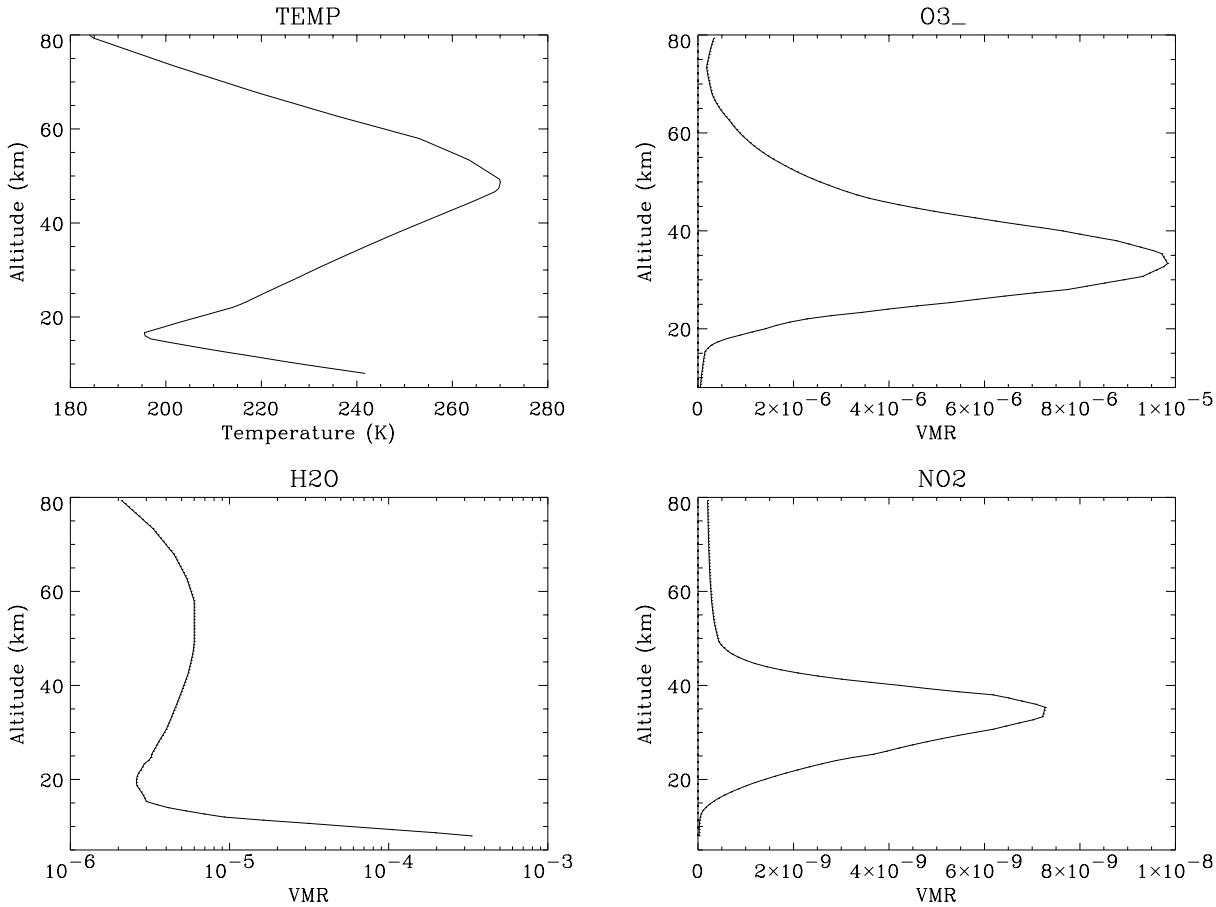
Figure 21: (a) Temperature (K), (b) ozone, (c) water vapor and (d) nitrogen dioxide volume mising ratio (ppv) profiles for the AFGL tropical atmosphere.
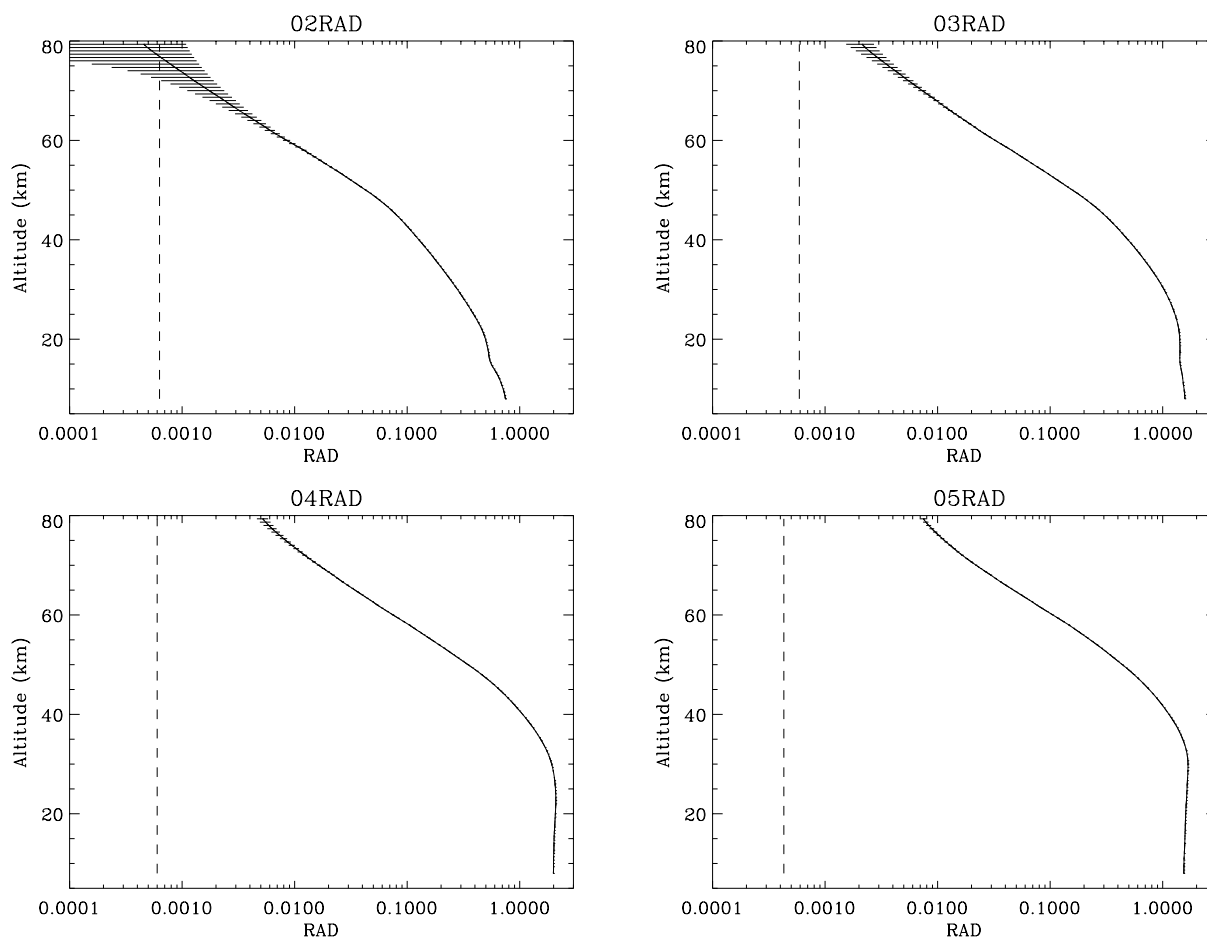
Figure 22: Radiance profiles (Wm^{-2}sr^{-1}) for the HIRDLS temperature sounding channels (2,3,4,5) calculated for the AFGL tropical atmosphere. The vertical lines and error bars are the channel noise estimates of Table 2.
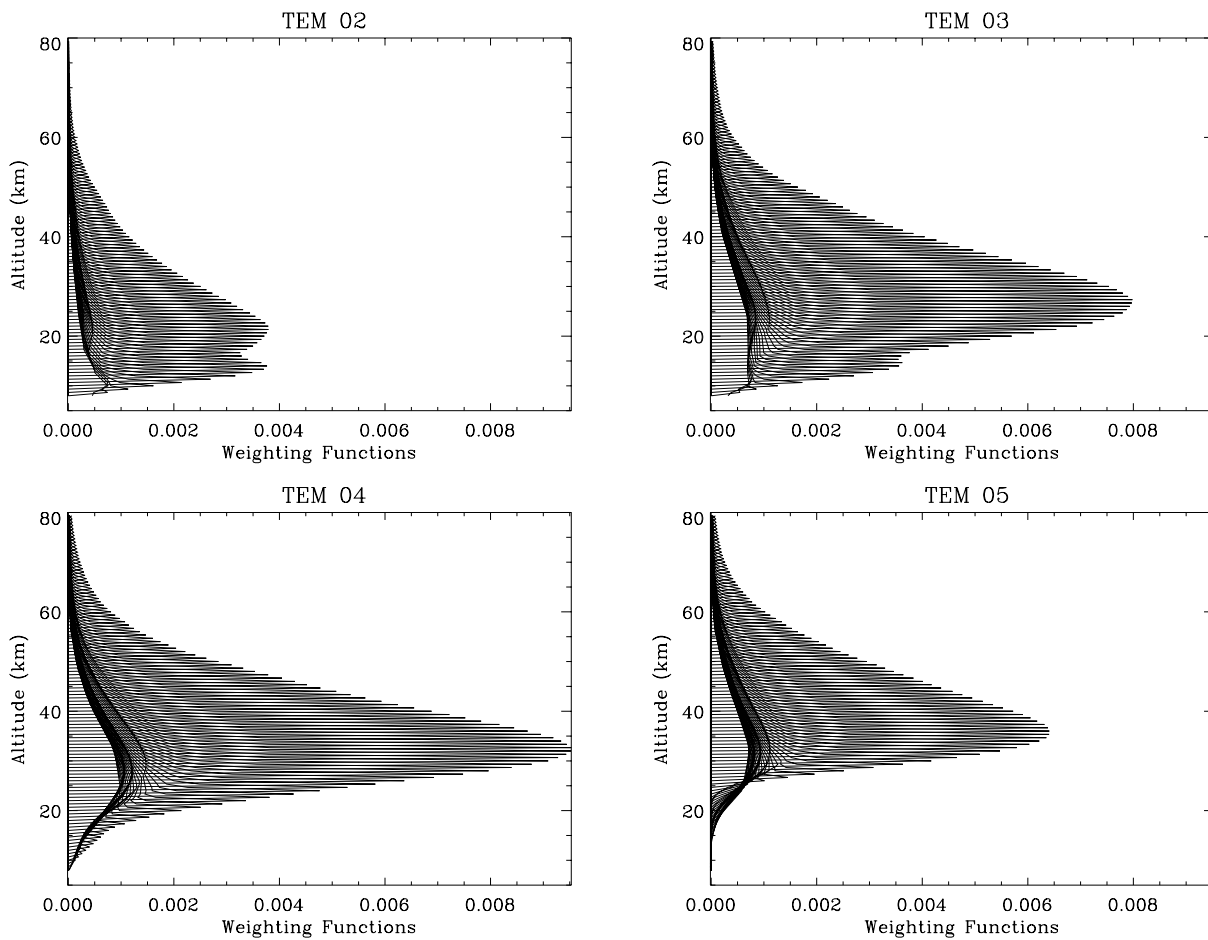
Figure 23: Weighting functions, $\partial R/\partial T$, for the HIRDLS temperature sounding channels (2,3,4,5) calculated for the AFGL tropical atmosphere using a perturbation method and displayed on an approximate altitude scale.
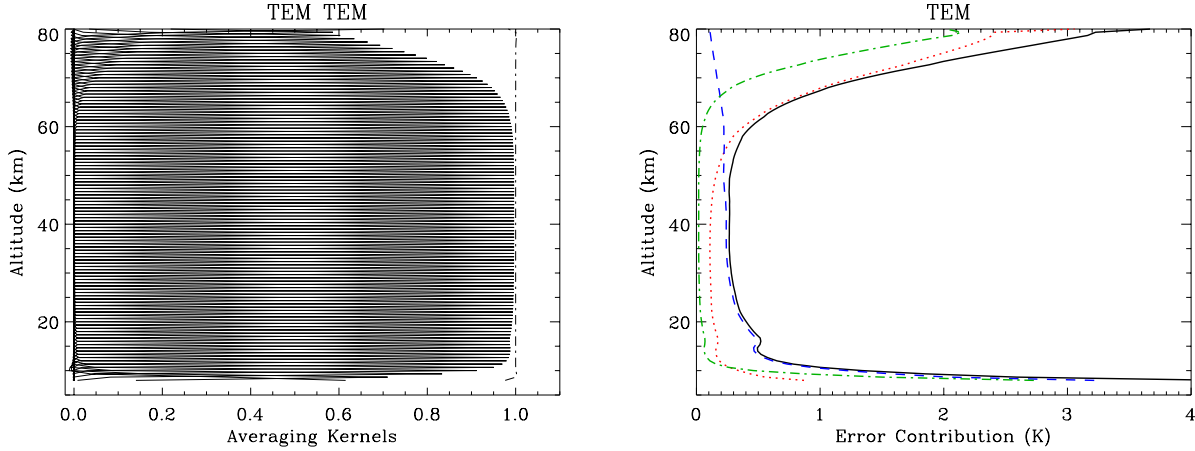
Figure 24: (a) Averaging kernels and (b) random error contributions for the HIRDLS temperature sounding channels calculated for the AFGL tropical atmosphere. The dot-dash line in (a) represents the sum of the averaging kernel rows. In (b) the solid line represents the total error and the dotted, dashed and dot-dashed lines represent the measurement noise, forward model and a priori error contributions, respectively.

3.6.7 Aerosol Retrieval and Correction Schemes

We outline below the separate schemes for aerosol retrieval and correction. It is expected that case (i) will be used to retrieve aerosol and that aerosol contamination of the gaseous sounding channels will be handled by case (iii).

3.6.7.1 Incorporating aerosol extinction in the HIRDLS retrievals.   The HIRDLS retrieval scheme will be implemented using two approaches for dealing with aerosols which address the need (A) to retrieve gaseous species by adequately accounting for the aerosol contamination, and (B) to obtain spectral information on aerosols. For case (A) we will use the most recent laboratory information on the properties of aerosols to construct a spectral model which relates the aerosol extinction observed in one HIRDLS channel to another. Case (A) may be subdivided into (i) retrieval of aerosol extinction/effective radius, (ii) a joint retrieval of temperature/pressure, constituents and aerosol extinction/effective radius and (iii) an aerosol contamination correction. However, we recognize that the spectral model used in (i) and (ii) may be inadequate under certain circumstances (e.g. for dense PSC's and cirrus) and that for aerosol studies it is necessary to retain the capability to retrieve the aerosol extinction without reference to any imposed spectral model. Hence, for case (B) we will have a separate retrieval for aerosol extinction for each of the HIRDLS aerosol channels.

3.6.7.1.1 Aerosol retrieval (case (i)).   This is the default case. The retrieval of aerosol extinction (at the reference wavelength) and effective radius will be performed using the 4 channels (1,6,13,19) as summarized in Table 10. The underlying assumption is that the aerosol type (e.g. sulfate, PSC, etc.) is known, and the composition is predicted based on temperature, water vapor and nitric acid concentrations. The spectral model given by Eqn 7 provides a constraint on the retrieval from which we which will obtain (i) the best estimate of the aerosol extinction, β^0, at a single reference wavelength (chosen to be channel 6 at $\lambda_0 = 12 \ \mu$m) and (ii) the aerosol effective particle radius, r_e (see Figure 25). These quantities are included in the retrieval state vector for altitudes at which aerosol correction is important. We must also supply a priori data for the extinction and effective radius. The forward model provides weighting functions $\partial \mathbf{y}/\partial \beta^0$ and $\partial \mathbf{y}/\partial \mathbf{r}_e$ and all the radiance channels that are included in the measurement vector, $\mathbf{y}$, contribute to the estimated extinction and effective radius. The retrieval starts with an initial estimate of β^0 and r_e (contained in the state vector) and calculates β_c from Eqn 7. These channel extinctions are converted to aerosol optical depths (Eqn 3) and combined with the gaseous optical depths in the radiative transfer code. The values of β^0 and r_e are adjusted as part of the state vector during the retrieval process described in Section 3.4. The covariances of β^0 and $\mathbf{r}_e$ are obtained from the error analysis treatment
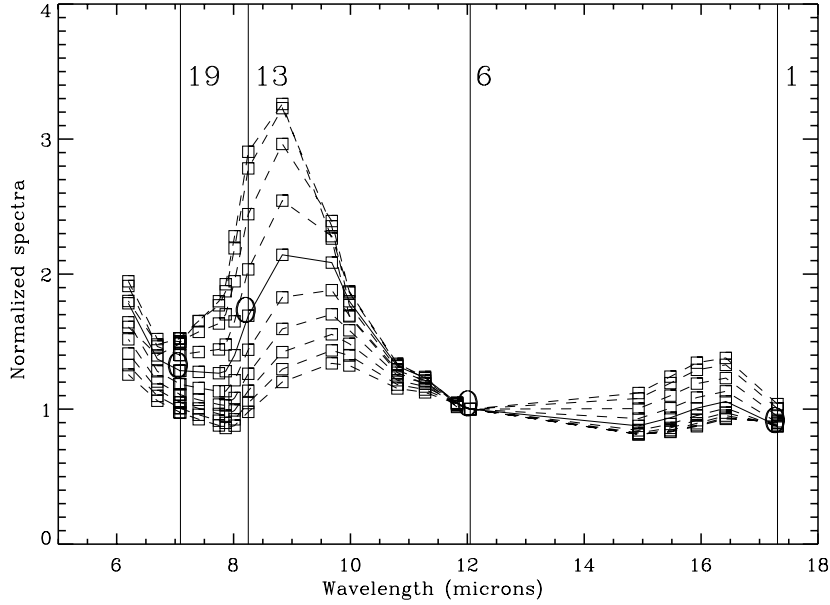
Figure 25: A family of sulfate aerosol extinction spectra for a 50 % H_2SO_4 composition, normalized to unity for HIRDLS Channel 6, calculated for various particle size distributions spanning an effective radius range of $0.1 < r_e < 2.0$ μm. These curves are a graphical representation of Eqn 6 for a fixed composition. The four HIRDLS aerosol channels are labelled. The solid line is an illustration of a curve obtained from retrieved values of β^0 and r_e.

Target	Channels	Contaminants				
Aerosol	1	N_2O	H_2O	CO_2		
		C	C	C		
		R1	R1	C		
	6	CO_2	O_3	H_2O		
		F	C	C		
		F	R1	R1		
	13	CH_4	CO_2	N_2O	HNO_3	O_3
		C	C	C	C	C
		R1	C	R1	R1	R1
	19	H_2O				
		C				
		R1				

Table 10: Joint retrieval of aerosol extinction and effective radius from 4 channels (1,6,13,19) (case (i)).

given in Section 3.5.

3.6.7.1.2 Aerosol retrieval (case (ii)). This is an extension of case (i) and may be used in later iterations. Here we implement an aerosol retrieval and correction scheme which uses knowledge of the aerosol spectral model, but applies the algorithm to all channels, so that solutions are obtained simultaneously for temperature/pressure, and the aerosol parameters.

3.6.7.1.3 Aerosol contamination correction (case (iii)). This is a simplification of case (ii), in which we use knowledge of the spectral variation of the aerosol extinction, perhaps obtained from previous measurements or from other sources, and determine the magnitude of the extinction in all channels based on the extinction at the reference wavelength.

3.6.7.1.4 Aerosol spectral retrieval (case (iv)). The aerosol retrieval schemes discussed above (cases (i) and (ii)) preclude obtaining unanticipated spectral variation of the aerosol extinction because of the imposition of the spectral model. Therefore, as necessary, perhaps mainly as a research activity, we will implement single channel aerosol retrievals to determine extinction at each of the wavelengths of the aerosol-sensitive channels.

3.6.8 Trace Gas Single Product Retrievals

3.6.8.1 Retrieval of O_3. The retrieval of O_3 will be performed using 3 channels (10,11,12) and is summarized in Table 11.

Target	Channels	Contaminants				
O_3	10	CO_2	Aerosol			
		F	R1			
		F	R2			
	11	CO_2	Aerosol			
		F	R1			
		F	R2			
	12	N_2O	CFC12	H_2O	Aerosol	
		C	C	C	R1	
		R1	R1	R1	R2	

Table 11: Retrieval of O_3 from 3 channels (10,11,12).

A retrieval characterization and error analysis has been performed for the HIRDLS O_3 sounding channels (10,11,12) for the AFGL tropical atmosphere O_3 profile shown in Figure 21. The diagonal elements of the a priori covariance matrix, $S_{x_a}^{ii}$ were set at $(75 \% VMR(O_3))^2$ and the off-diagonal elements were calculated using a $l = 10$ km correlation length (Eqn 84). Figures 26–28 show the results of calculations of radiance profiles, weighting functions, averaging kernels and random error contributions for the O_3 sounding channels. The forward model error dominates the errors on the retrieved O_3 profile from 20–50 km, below 20 km and above 50 km the measurement noise and a priori error have an increasing contribution.

3.6.8.2 Retrieval of H_2O. The retrieval of H_2O will be performed using 2 channels (18,20) and is summarized in Table 12.

A retrieval characterization and error analysis has been performed for the HIRDLS H_2O sounding channels (18,20) for the AFGL tropical atmosphere H_2O profile shown in Figure 21. The diagonal elements of the a priori covariance matrix, $S_{x_a}^{ii}$ were set at $(75 \% VMR(H_2O))^2$ and the off-diagonal elements were calculated using a $l =$
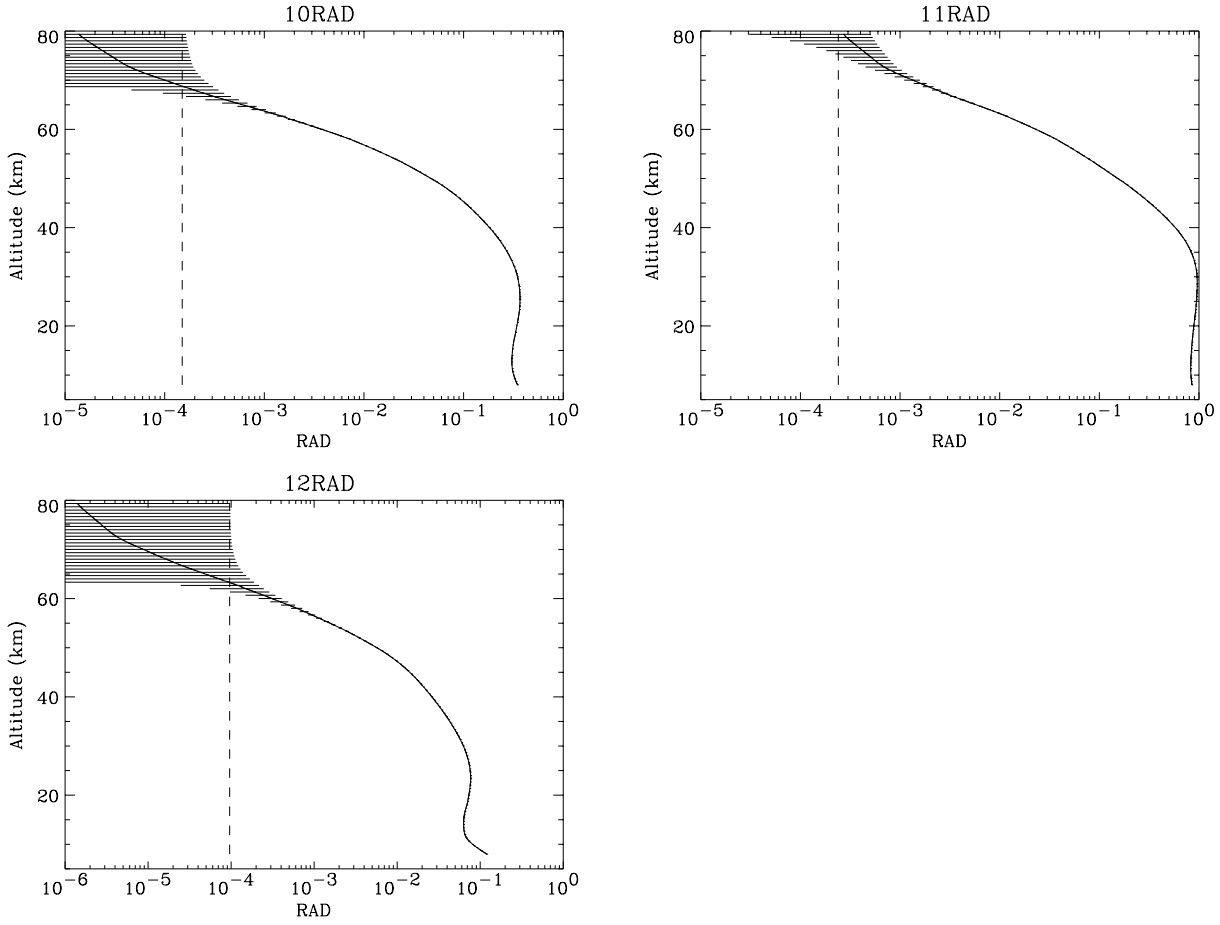
Figure 26: Radiance profiles ($Wm^{-2}sr^{-1}$) for the HIRDLS O_3 sounding channels (10,11,12) calculated for the AFGL tropical atmosphere. The vertical lines and error bars are the channel noise estimates of Table 2.

Target	Channels	Contaminants				
H_2O	18	CH_4	O_3	O_2	CO_2	Aerosol
		C	R1	F	F	R1
		R1	R2	F	F	R2
	20	CH_4	O_3	Aerosol		
		C	R1	R1		
		R1	R2	R2		

Table 12: Retrieval of H_2O from 2 channels (18,20).
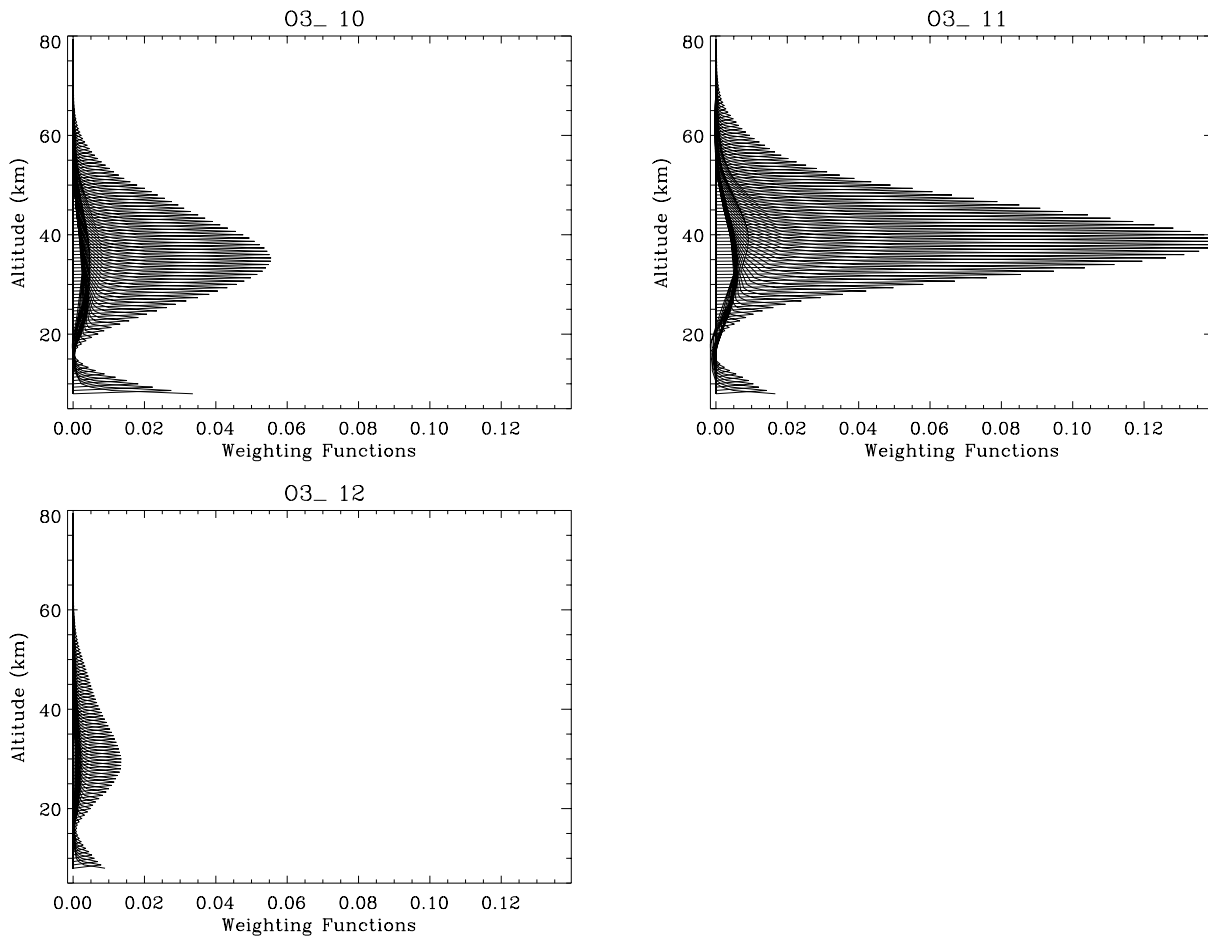
Figure 27: Weighting functions, $\partial R / \partial \ln(O_3)$, for the HIRDLS O_3 sounding channels (10,11,12) calculated for the AFGL tropical atmosphere using a perturbation method and displayed on an approximate altitude scale.
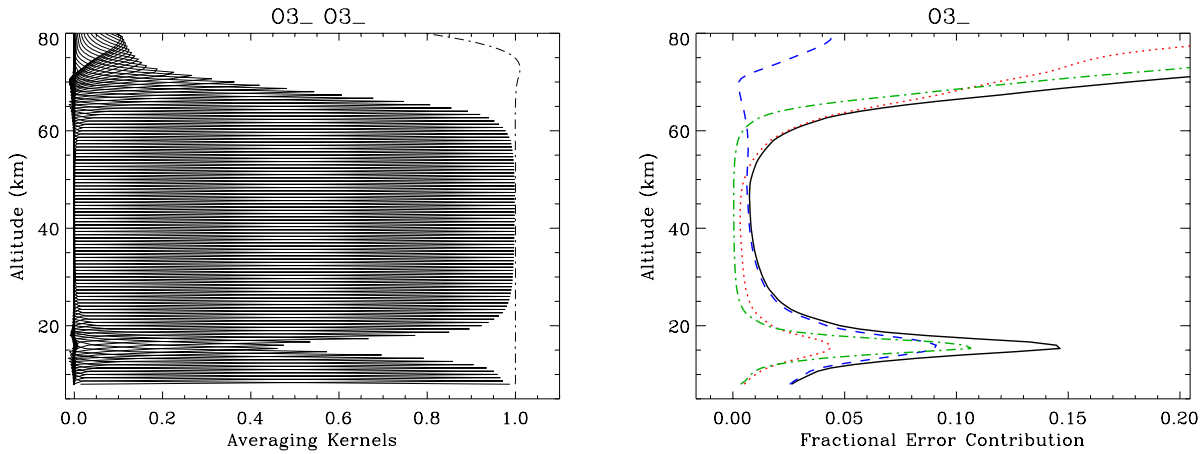
Figure 28: (a) Averaging kernels and (b) fractional random error contributions for the HIRDLS O_3 sounding channels calculated for the AFGL tropical atmosphere. The dot-dash line in (a) represents the sum of the averaging kernel rows. In (b) the solid line represents the total fractional error and the dotted, dashed, dot-dashed lines represent the measurement noise, forward model, and a priori fractional error contributions, respectively.

10 km correlation length (Eqn 84). Figures 29–31 show the results of calculations of radiance profiles, weighting functions, averaging kernels and random error contributions for the H_2O sounding channels. The measurement noise dominates the errors on the retrieved H_2O profile from 15–60 km, below 15 km and above 60 km the forward model error and a priori error have an increasing contribution.
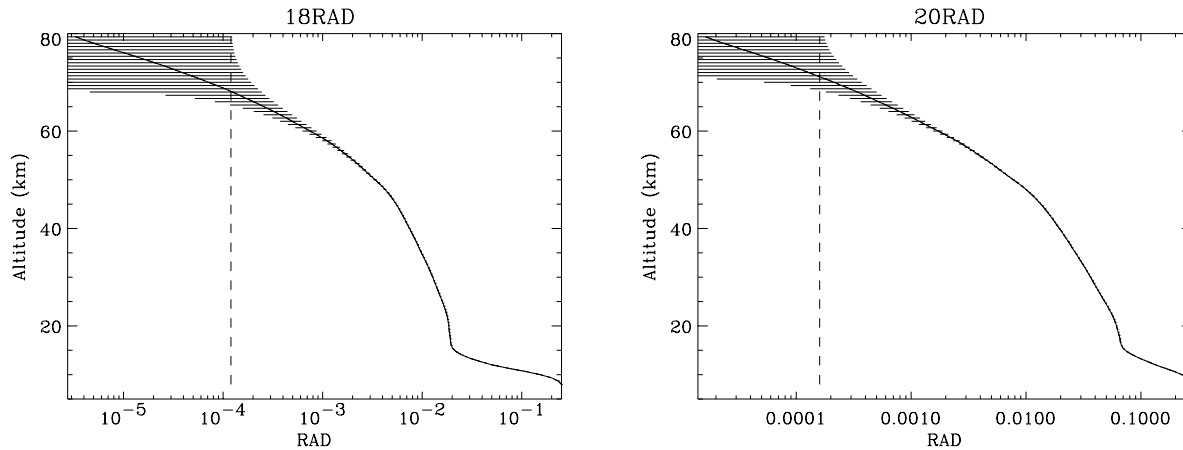
Figure 29: Radiance profiles ($Wm^{-2}sr^{-1}$) for the HIRDLS H_2O sounding channels (18,20) calculated for the AFGL tropical atmosphere. The vertical lines and error bars are the channel noise estimates of Table 2.

3.6.8.3 Retrieval of NO$_2$. The retrieval of NO_2 will be performed using a single channel (21) and is summarized in Table 13.

A retrieval characterization and error analysis has been performed for the HIRDLS sounding channel (21) for the AFGL tropical atmosphere NO_2 profile shown in Figure 21. The diagonal elements of the a priori covariance matrix, $S_{x_a}^{ii}$ were set at $(75\ \%VMR(NO_2))^2$ and the off-diagonal elements were calculated using a $l = 10$ km correlation length (Eqn 84). Figures 32–34 show the results of calculations of radiance profiles, weighting
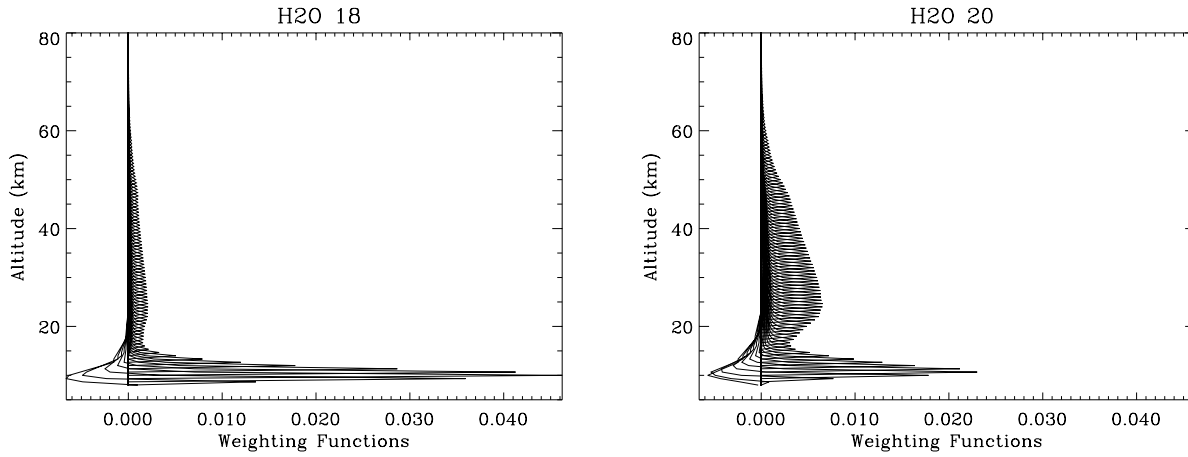
Figure 30: Weighting functions, $\partial R/\partial \ln(H_2O)$, for the HIRDLS H_2O sounding channels (18,20) calculated for the AFGL tropical atmosphere using a perturbation method and displayed on an approximate altitude scale.
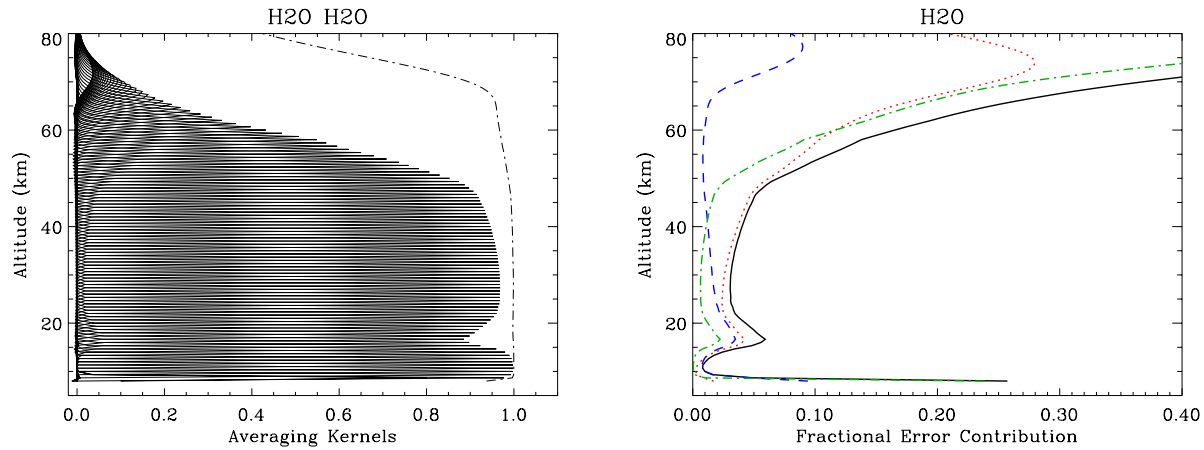
Figure 31: (a) Averaging kernels and (b) fractional random error contributions for the HIRDLS H_2O sounding channels calculated for the AFGL tropical atmosphere. The dot-dash line in (a) represents the sum of the averaging kernel rows. In (b) the solid line represents the total fractional error and the dotted, dashed, dot-dashed lines represent the measurement noise, forward model, and a priori fractional error contributions, respectively.

Target	Channels	Contaminants				
		H_2O	CH_4	O_2	Aerosol	
NO_2	21	R1	C	F	R1	
		R2	R1	F	R2	

Table 13: Retrieval of NO_2 from a single channel (21).

functions, averaging kernels and random error contributions for the NO_2 sounding channel. The measurement noise dominates the errors on the retrieved NO_2 profile from 22–44 km, below 22 km and above 44 km the a priori error has an increasing contribution.
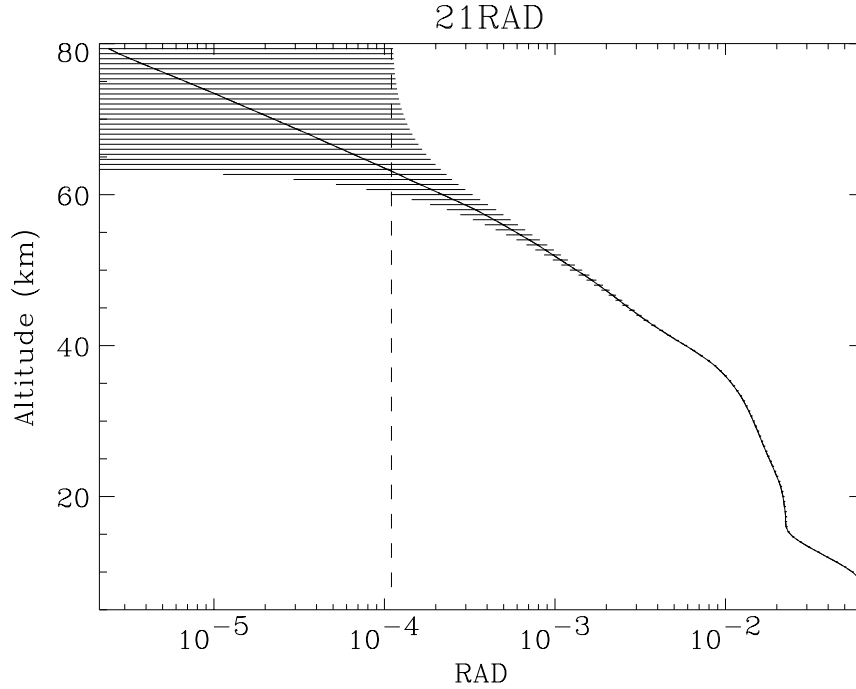
Figure 32: Radiance profile $(Wm^{-2}sr^{-1})$ for the HIRDLS NO_2 sounding channel (21) calculated for the AFGL tropical atmosphere. The vertical lines and error bars are the channel noise estimates of Table 2.

3.6.9 Trace Gas Multiple Product Retrievals: CFCl$_3$, CF$_2$Cl$_2$, HNO$_3$

The retrieval of CFCl$_3$, CF$_2$Cl$_2$, and HNO$_3$ will be performed jointly from 3 channels (7,8,9) and is summarized in Table 14.

3.6.10 Trace Gas Multiple Product Retrievals: N$_2$O, N$_2$O$_5$, ClONO$_2$, CH$_4$

The retrieval of N$_2$O, N$_2$O$_5$, ClONO$_2$, and CH$_4$ will be performed jointly from 4 channels (7,8,9) and is summarized in Table 15.

A retrieval characterization and error analysis has been performed for the HIRDLS sounding channels (14,15,16,17) for the AFGL tropical atmosphere profile shown in Figure 35. The diagonal elements of the a priori covariance matrix, $S_{x_a}^{ii}$ were set at $(75 \% VMR(O_3))^2$ and the off-diagonal elements were calculated using a $l = 10$ km correlation length (Eqn 84). Figures 36–39 show the results of calculations of radiance profiles, weighting functions, averaging kernels and random error contributions for the C14 – C17 sounding channels.

3.6.11 Cloud Tops

The location of cloud tops will be performed in the Level-2 pre-processing stage (Section 3.2).
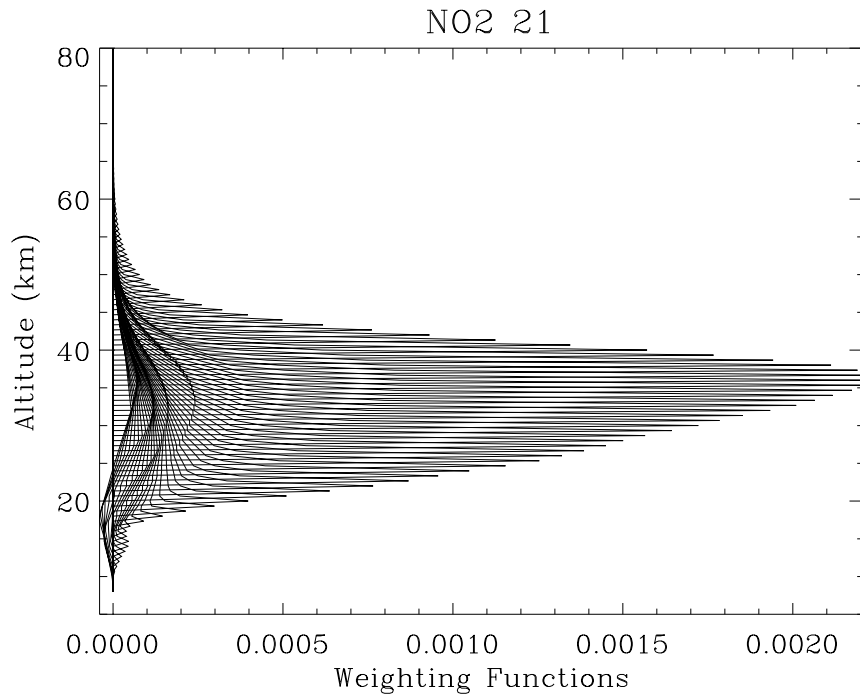
Figure 33: Weighting functions, $\partial R/\partial \ln(H_2O)$, for the HIRDLS NO_2 sounding channel (21) calculated for the AFGL tropical atmosphere using a perturbation method and displayed on an approximate altitude scale.
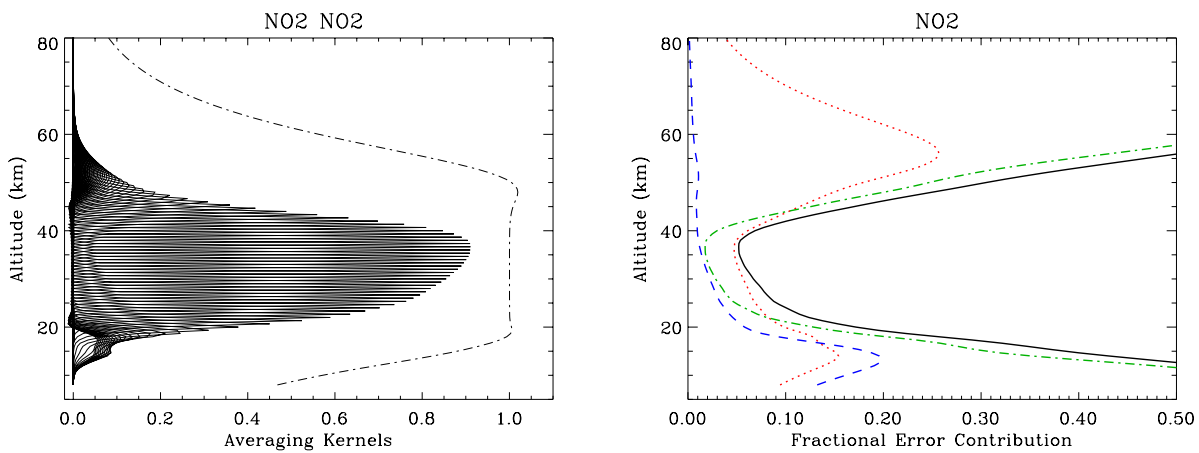
Figure 34: (a) Averaging kernels and (b) fractional random error contributions for the HIRDLS NO_2 sounding channel calculated for the AFGL tropical atmosphere. The dot-dash line in (a) represents the sum of the averaging kernel rows. In (b) the solid line represents the total fractional error and the dotted, dashed, dot-dashed lines represent the measurement noise, forward model, and a priori fractional error contributions, respectively.

Target	Channels	Contaminants				
CFC11	7	HNO_3	CO_2	O_3	Aerosol	
		R^*	F	R1	R1	
		R^*	F	R2	R2	
HNO_3	8	CFC11	CFC12	H_2O	Aerosol	
		R^*	R^*	R1	R1	
		R^*	R^*	R2	R2	
CFC12	9	HNO_3	CO_2	H_2O	Aerosol	
		R^*	F	R1	R1	
		R^*	F	R2	R2	

Table 14: Joint retrieval of HNO_3, CFC11 and CFC12 from 3 channels (7,8,9).

Target	Channels	Contaminants						
N_2O_5	14	CH_4	N_2O	H_2O	CO_2	Aerosol		
		R^*	R^*	R1	F	R1		
		R^*	R^*	R2	F	R2		
N_2O	15	CH_4	HNO_3	$ClONO_2$	H_2O	CO_2	CF_4	Aerosol
		R^*	R1	R^*	R1	F	C	R1
		R^*	R2	R^*	R2	F	C	R2
$ClONO_2$	16	CH_4	N_2O	HNO_3	CF_4	H_2O	Aerosol	
		R^*	R^*	R	C	R1	R1	
		R^*	R^*	R	C	R2	R2	
CH_4	17	H_2O	HNO_3	N_2O	CO_2	Aerosol		
		R1	R1	R^*	F	R1		
		R2	R2	R^*	F	R2		

Table 15: Joint retrieval of N_2O_5, N_2O, $ClONO_2$ and CH_4 from 4 channels (14,15,16,17).
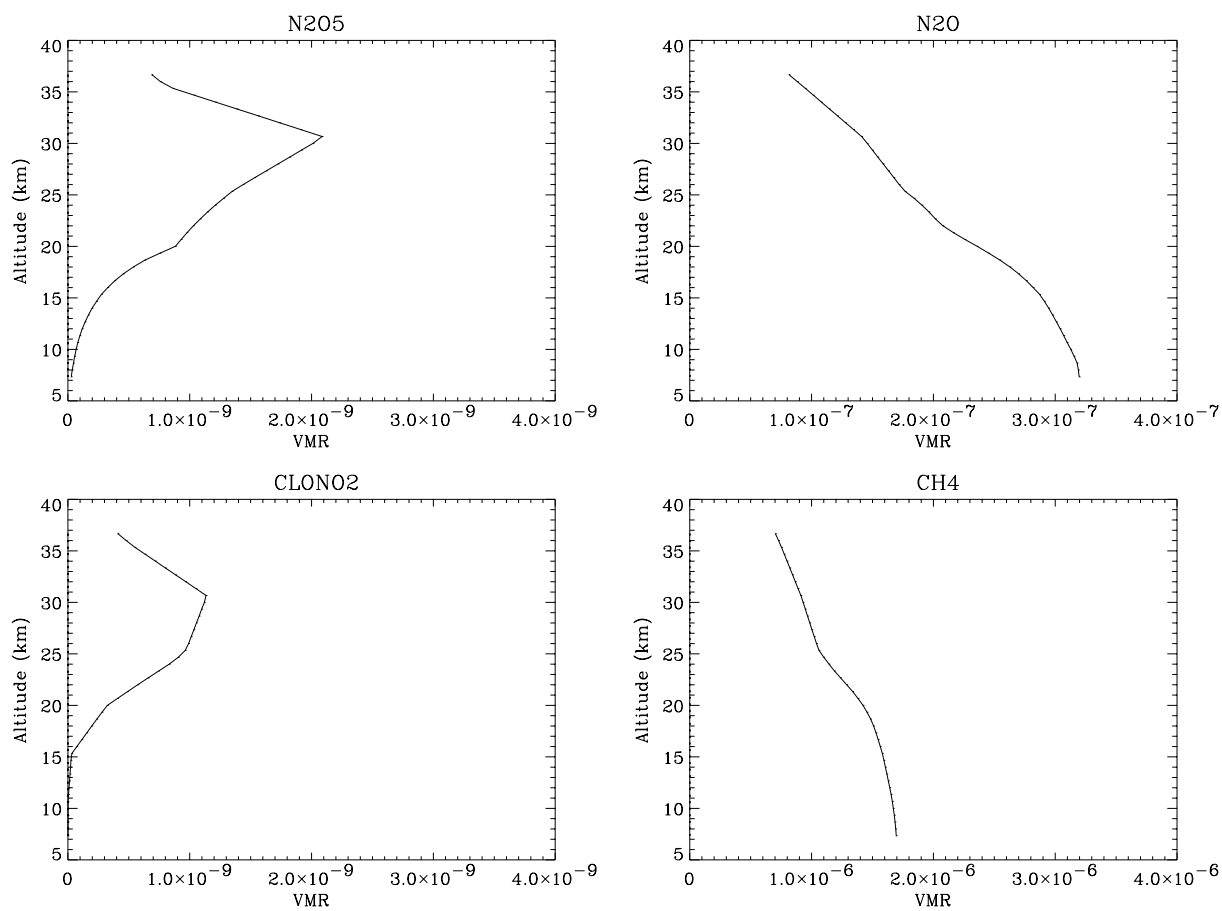
Figure 35: (a) Dinitrogen pentoxide, (b) nitrous oxide, (c) chlorine nitrate and (d) methane volume mising ratio (ppv) profiles for the AFGL tropical atmosphere.
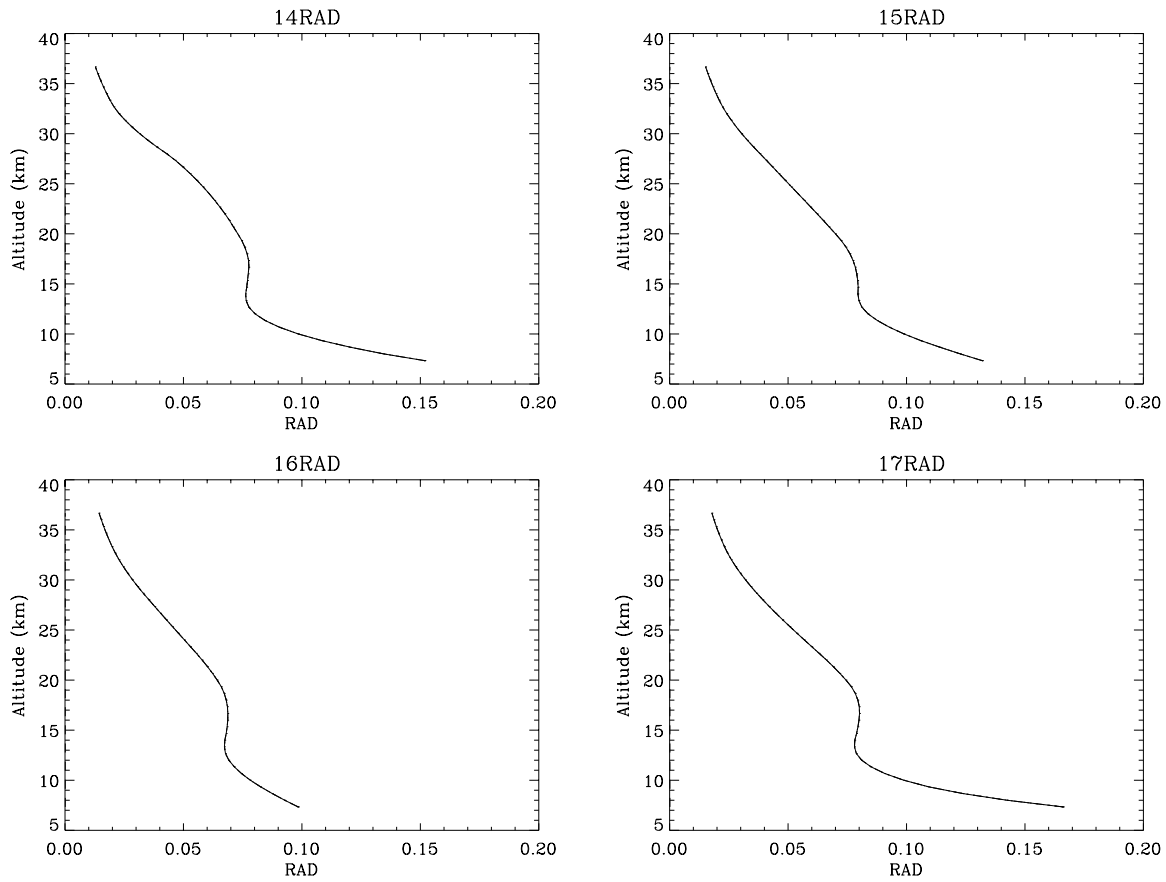
Figure 36: Radiance profiles (Wm^{-2}sr^{-1}) for the HIRDLS sounding channels (14,15,16,17) calculated for the AFGL tropical atmosphere. The vertical lines and error bars are the channel noise estimates of Table 2.
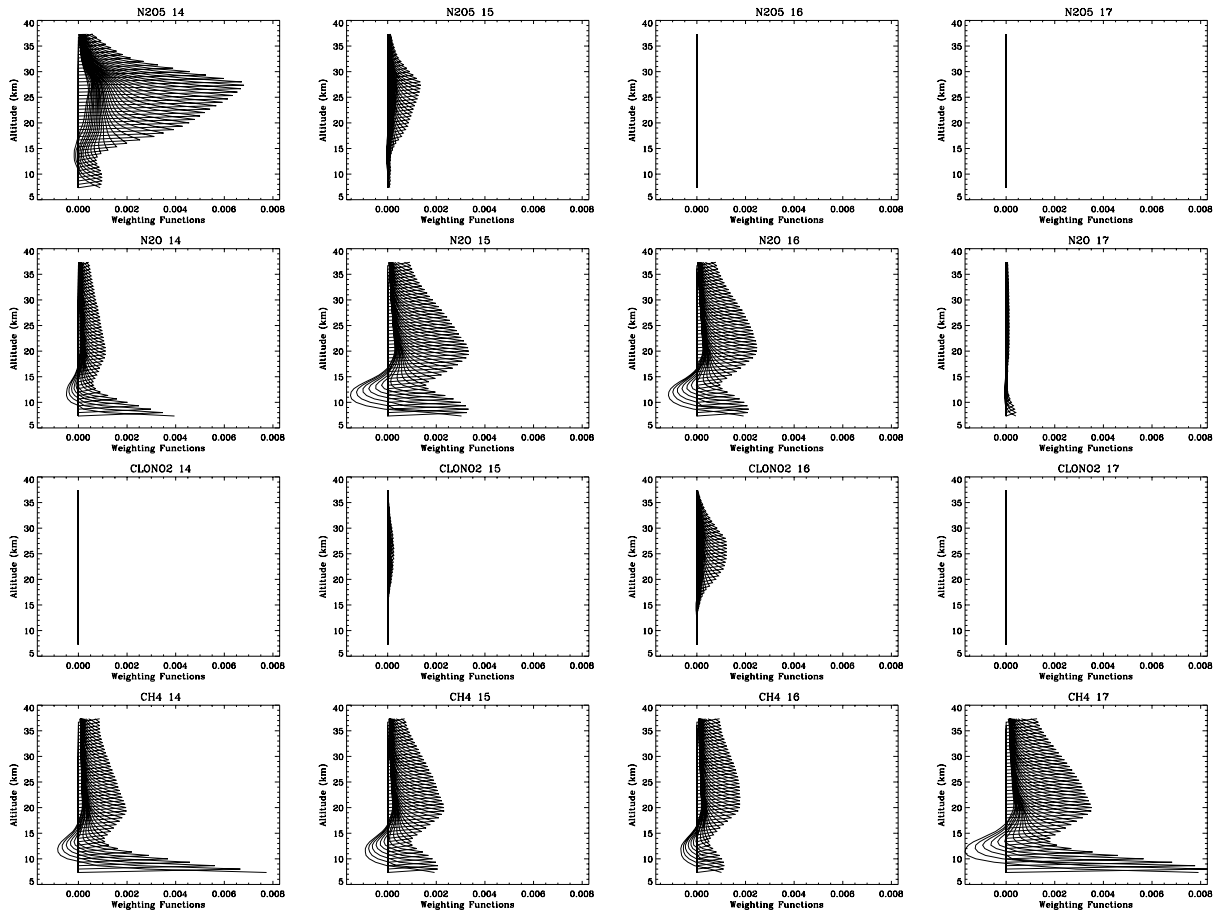
Figure 37: Weighting functions, $\partial R/\partial \ln(VMR)$, for the HIRDLS sounding channels (14,15,16,17) calculated for the AFGL tropical atmosphere using a perturbation method and displayed on an approximate altitude scale.
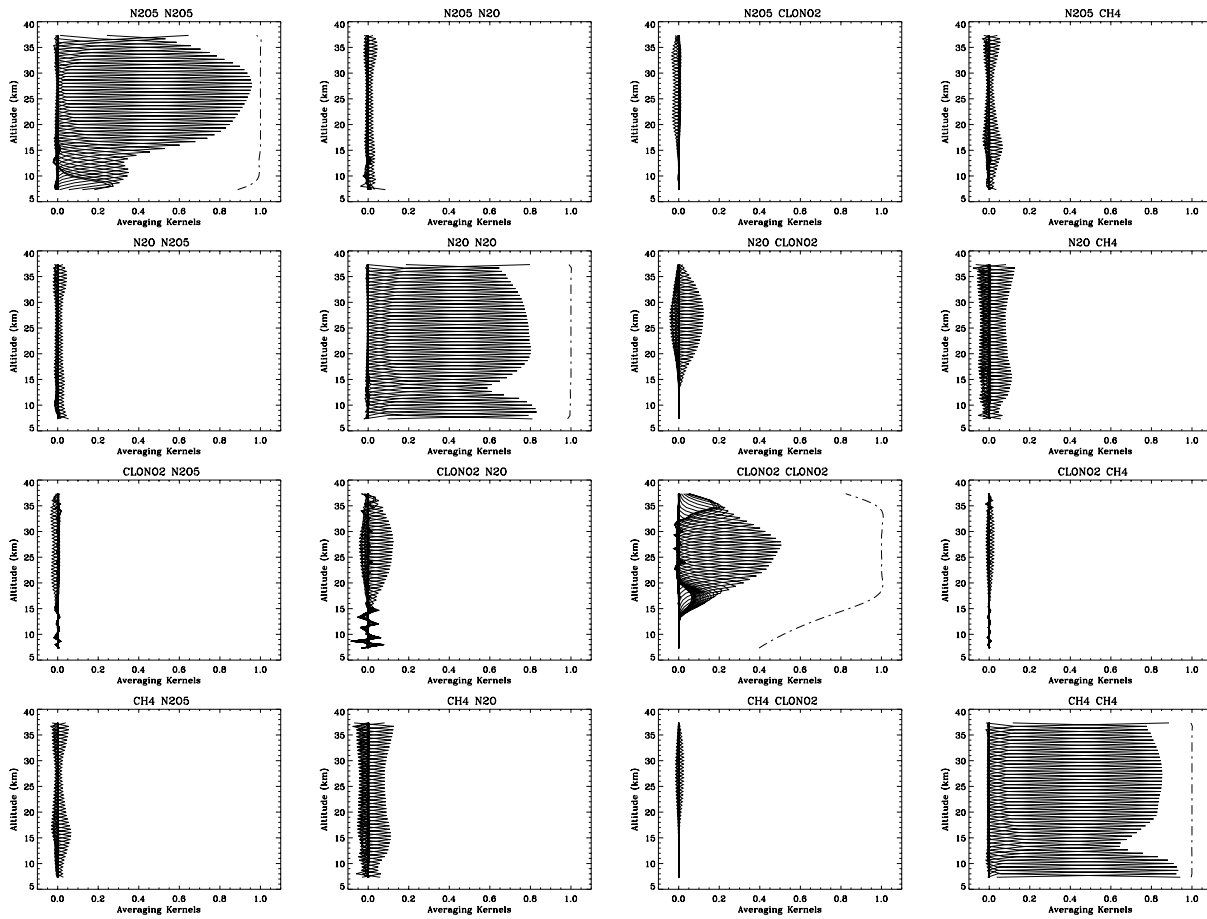
Figure 38: Averaging kernels for the joint retrieval of N_2O, N_2O_5, $ClONO_2$, and CH_4 from the HIRDLS sounding channels (14,15,16,17) calculated for the AFGL tropical atmosphere. The dot-dash line represents the sum of the averaging kernel rows.
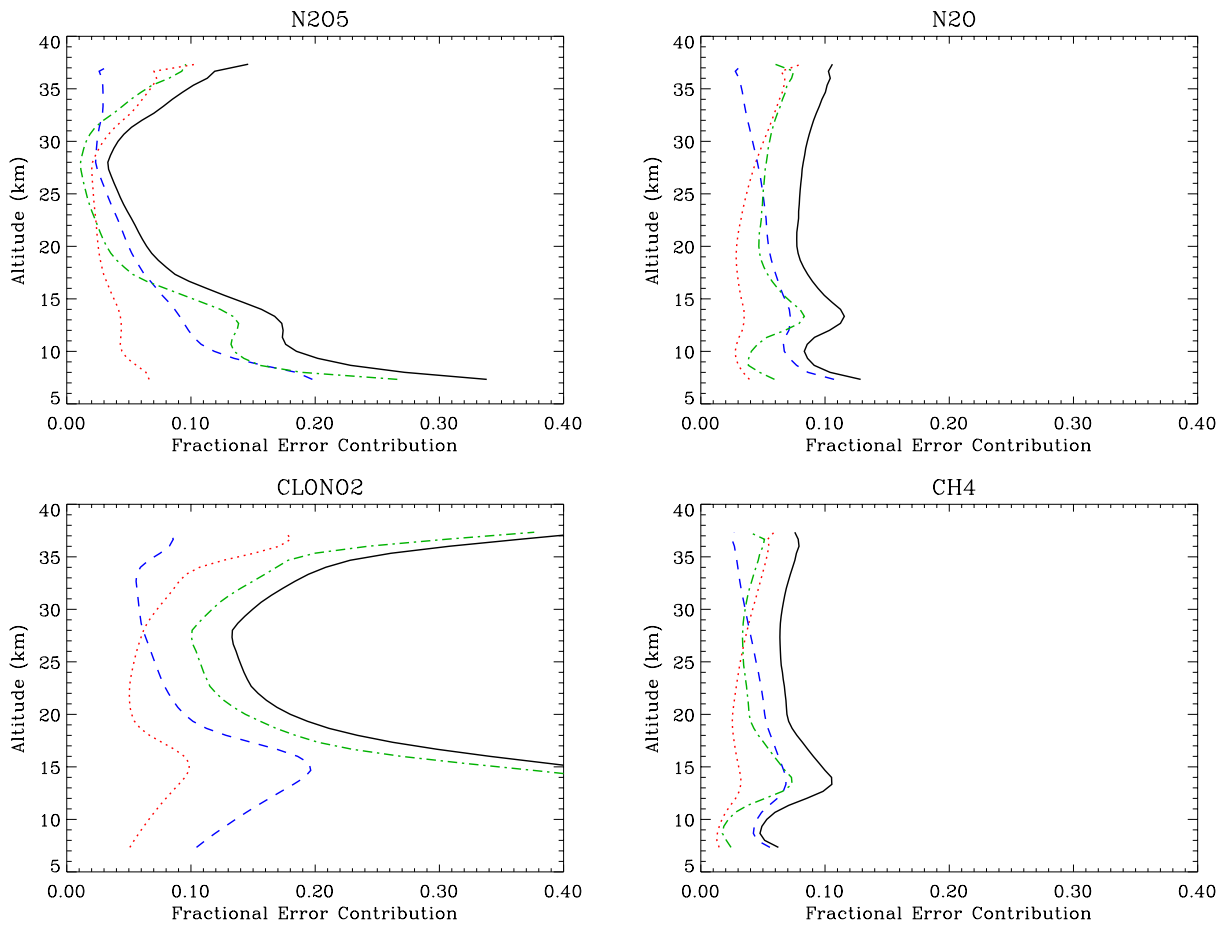
Figure 39: Fractional random error contributions for the joint retrieval of N_2O, N_2O_5, $ClONO_2$, and CH_4 from the HIRDLS sounding channels (14,15,16,17) calculated for the AFGL tropical atmosphere. The solid line represents the total fractional error and the dotted, dashed, dot-dashed lines represent the measurement noise, forward model, and a priori fractional error contributions, respectively.

4 Evaluation and Testing

The evaluation and testing of HIRDLS science algorithms is an on-going process that commenced with early exploratory studies and will continue through post-launch data product validation. These activities extend beyond the computer codes themselves into the application of the tools and the conclusions drawn from them.

Somewhat different approaches to testing are utilized depending on the type of algorithm and the context in which it is employed. It is important to recognize that in many cases, the same algorithm may exist within different applications and is thus implicitly tested in a variety of ways. An example is the retrieval algorithm suite included in research codes (used for error analysis and sensitivity studies); in prototype retrieval codes (for processor engineering and development activities); and in delivered production software (for data product creation).

It is also important to remember that often a hierarchy of algorithms may exist to do the same type of computation. This is particularly true in the area of the forward radiative transfer model where algorithms range from very accurate physical models necessary for precise calculations to computationally fast, highly parameterized codes for use in production processing. Intercomparisons between the various members of the hierarchy provide important verifications as to the accuracy and robustness of science algorithms within the production environment.

In the pre-launch period and at times during the post-launch period, data simulation provides an important mechanism by which algorithms can be evaluated with known, controlled inputs. Simulation must be carried out carefully, however. Often the complexity of the simulators approach the complexity of the codes which they are to test and it can become difficult to determine if the problems lie in the science code; the simulator or both.

Finally, when possible the use of existing measurements from previous missions may provide an ultimate test for algorithms. Unfortunately, the planned configuration and operation of the new instrument may differ significantly from the previous experiment to the point that it is difficult to test the desired algorithm configuration completely.

4.1 Test Configurations

This section describes the configurations within which evaluation and testing of HIRDLS science algorithms most often occur. The focus of testing and the criteria for evaluation vary considerably depending on the context.

Research codes represent the initial application of most science algorithms. It is within this context that potential algorithms are evaluated and tradeoffs are made. Thus research applications most often possess a degree of generality not always found in production algorithms. It is often the case that large amounts of additional intermediate and diagnostic information describing the performance of the algorithms are computed as well. This additional information provides part of the evaluation criteria along with theoretical expectations and scientific exactness. Research applications are frequently utilized to answer "what if" questions, to carry out sensitivity studies, to perform error analyses and to assist in instrument design trade-off studies.

Prototype production algorithms represent a step toward a more constrained, science data processing environment. In most cases they are the result of a selection process involving research applications. However, much of the generality of research codes may be absent from production prototypes. In the HIRDLS context, science algorithms delivered by the Science Development Group to the Data Product Development Group are considered prototypes. These codes may not possess all of the attributes of final production codes and may fail to conform to language standards, coding standards and error handling requirements. In addition, the codes may not have undergone significant optimization by the science developers. Prior to delivery, prototypes are to be verified as scientifically correct by the Science Development Group. The Data Product Development Group will test the codes for functional correctness within the context of the production environment.

The Data Product Development Group will re-engineer the science prototypes into production codes as necessary. Evaluation and testing will encompass the entire processor units of which science algorithms are components. Evaluation criteria will emphasize functional correctness, completeness, robustness and efficiency. Testing will require a variety of simulated input data sets in the correct formats and with content appropriate to the goals of the various tests.

4.2 Simulated Observations

The various test approaches discussed in the previous section imply requirements for different types of simulated data. Research codes can often suffice with simple parametric data simulators. These may be off-line or in some cases are built directly into the research application. Detailed testing of production processors on the other hand require comprehensive simulators which can produce data streams that appropriately mimic the flow of actual data from the ground system. The construction of these comprehensive simulators often requires significant effort and can rival the processors themselves in complexity.

The needs for comprehensive simulated data sets arise from requirements additional to the development of production software components (they are deliverable with each version of production processors) and include:

- verifying functional correctness and exception handling in the production environment.

- tuning processor performance and verifying resource utilization.

- performing end-to-end testing of the overall ground system.

- developing auxiliary software to support quality assurance and validation efforts.

Certain realities must be considered when developing a test and simulation philosophy. While real data from an instrument are valuable for testing front-end components of the system, they are almost always inadequate for testing higher level science data processors due to the difficulties in producing realistic observing conditions in the instrument test and calibration facility.

As pointed out above, a comprehensive simulator can be very complicated and as a consequence potentially becomes a source of error itself. Each production processor has its own unique pathological scenarios. Thus observational situations which are difficult for the Level-2 processor may present no problems for the Level-1 processor. It becomes unduly complicated to attempt to build all of the pathological cases for all levels of processing into a Level-0 simulator. It is simpler and more cost effective to develop individual simulators for each data product level and thus provide test data that realistically represent situations stressful to the algorithms. This requires that the data interfaces be well defined, maintained and verified to assure that end-to-end flow through the processor chain will be successful.

The HIRDLS team will produce a hierarchy of data simulators as part of the Science Data Product development activity. This hierarchy is shown in Figure 40. A key activity is the assimilation of a variety of global scale atmospheric state parameters to be sampled at HIRDLS measurement points. This requires a simulator that can emulate the CHEM spacecraft orbit as well as the HIRDLS scan pattern. The resulting atmospheric parameter profiles can then be used to calculate simulated observed radiance profiles in a Level-1 product simulator or formatted directly into a simulated Level-2 data product. Finally, the Level-1 product can be reverse-engineered into simulated Level-0 data. Assuming that appropriate care is taken, the various data products will be consistent and will allow processors to be tested individually or in an end-to-end manner.

4.3 Application to Real Data: Limb Infrared Monitor of the Stratosphere (LIMS) Observations

The Limb Infrared Monitor of the Stratosphere (LIMS) instrument that flew on the Nimbus-7 spacecraft in, 1978, was a precursor to the HIRDLS concept (Gille and Russell, 1984). It utilized a focal plane of fixed detectors that were scanned across the limb in the same manner as HIRDLS. Data were collected in 2 channels in the 15 micron band, 1 channel in the 9.6 micron O_3 band, 1 channel in the 11.3 micron HNO_3 band, 1 channel in the 6.2 micron NO_2 band and 1 channel in the 6.3 micron H_2O band. While not identical, these channels are in close proximity to a subset of the HIRDLS channels. Corresponding channels are compared in Table 16.

While the LIMS data cannot be used to test the HIRDLS Level-2 production processors directly, certain of the HIRDLS science algorithms can be tested in modified form. Among these are the forward radiance model methodology, the retrieval methodology and the method of correction for horizontal gradients in the atmosphere.

An additional benefit to applying the HIRDLS algorithms to LIMS observations would be the creation of a consistent data set for comparison of important atmospheric parameters between 1978 and 2003. Such a data
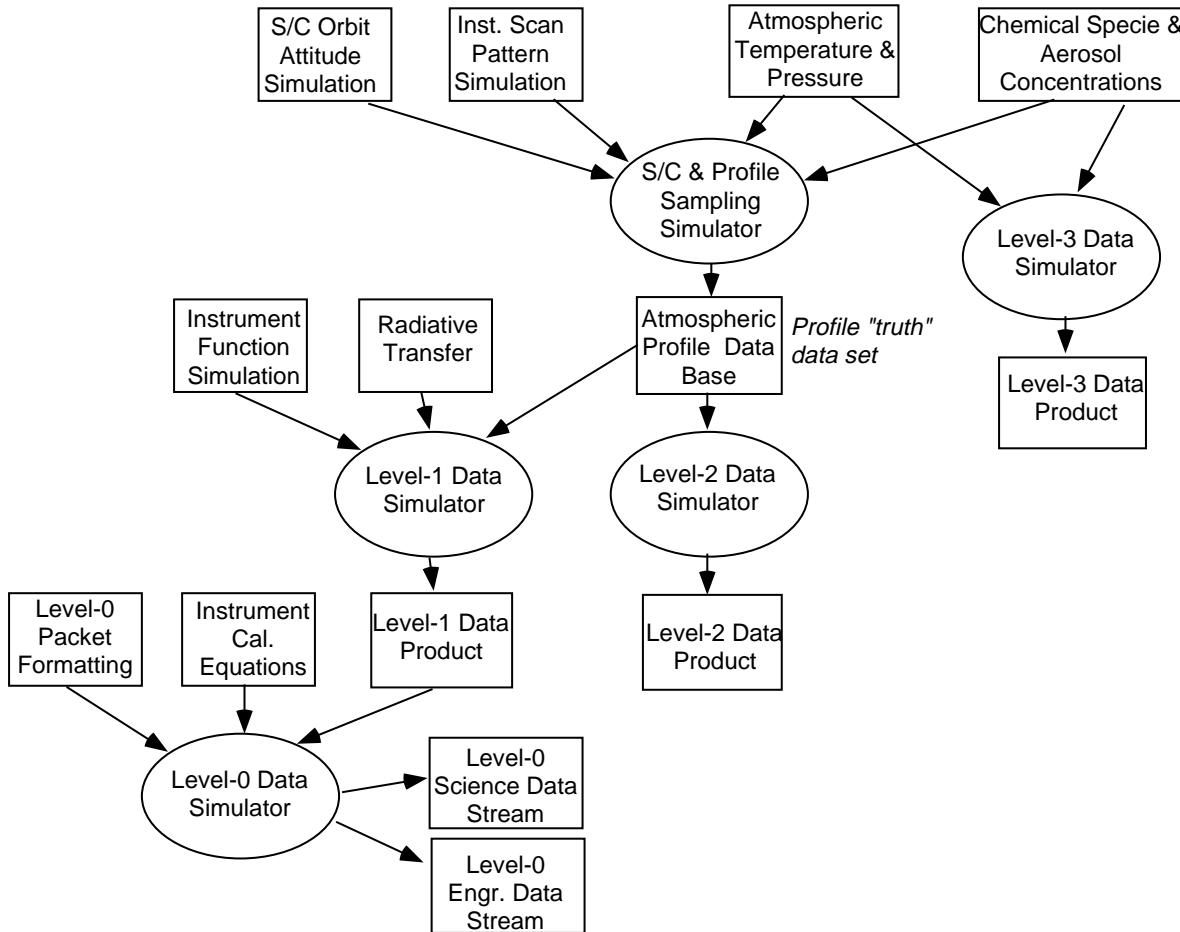
Figure 40: HIRDLS Data Simulator Hierarchy

LIMS Channel Number	Emitting Gas	LIMS Bandpass (cm^{-1})	HIRDLS Channel Number	HIRDLS Bandpass (cm^{-1})
1	NO_2	1560–1630	21	1585.5–1630.5
2	H_2O	1379–1560	20	1837.0–1435.0
3	O_3	926–1141	10	991.0–1009.0
			11	1011.0–1046.5
4	HNO_3	844–917	8	861.5–903.5
5	CO_2	579–755	3	600.5–639.5
6	CO_2	637–673	5	626.0–660.0

Table 16: Comparison of corresponding LIMS–HIRDLS channels.

set would be extremely valuable for validation as well as scientific investigations of human induced stratospheric changes.

Level 2 Processing
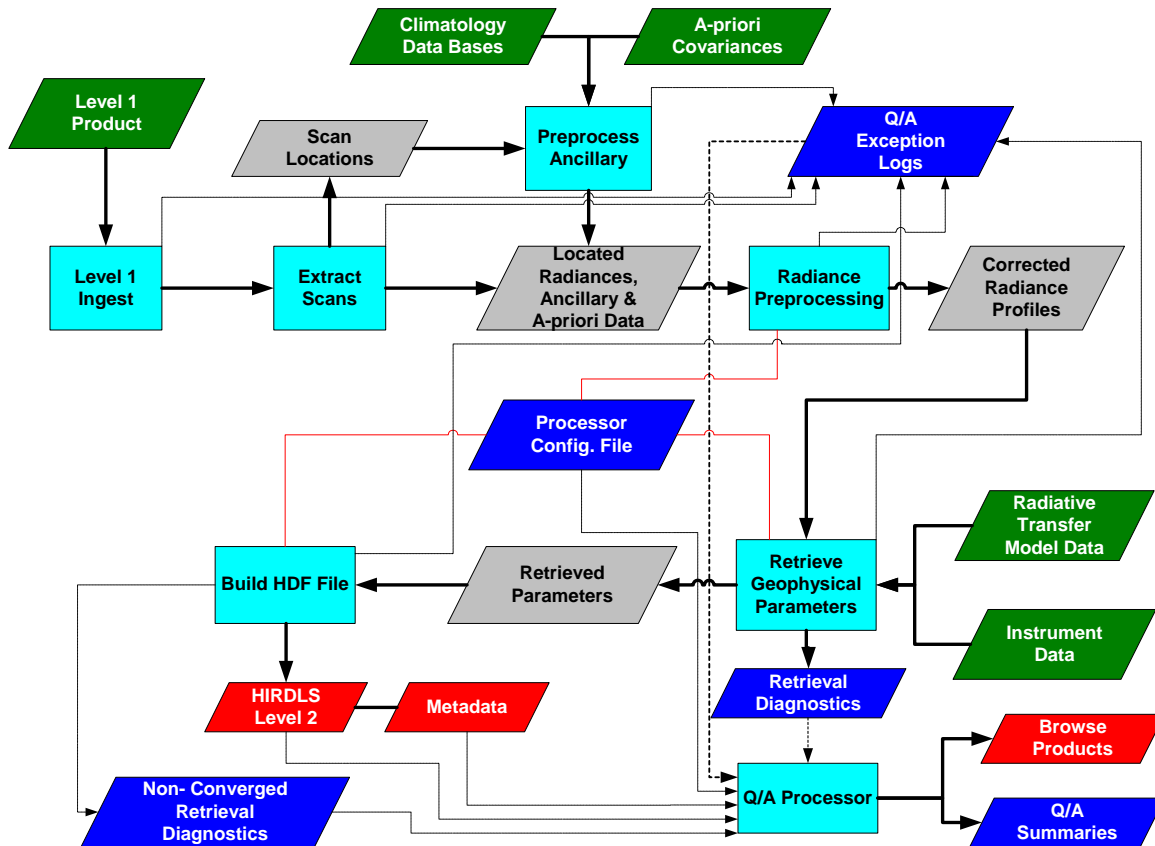
Figure 41: HIRDLS Level-2 processor schematic

4.4 Software Life-cycle

The development of HIRDLS Science Software (from design through testing) will depend, in part, on a close working relationship between the "science" and "product" development groups. To help this relationship, HIRDLS is adopting an incremental software development life-cycle (technically a modified waterfall with sub-projects), and frequent, informal progress reviews. Both of these strategies encourage quick feedback and help to prevent disconnects between the two groups.

5 Practical Considerations

5.1 Computation Considerations

5.1.1 SDP Tool Kit

The Science Data Processing Tool-kit is designed to insulate the science code itself from the burdens of the production environment, and also to standardize various widely used calculations such as geolocation. HIRDLS an-

ticipates the need to use the toolkit for input and output operations including HDF-EOS and ancillary data access, geolocation calculations and time/date calculations.

5.1.2 Input Data

Input data that are expected to be required for HIRDLS level-2 processing is shown in Table 17.

Mnemonic	Description
LV1	Level-1 Data (calibrated radiances + attitude data)
DRV	Driver File (processing control)
BBF	Planck Function Table (21 channels)
TRA	Transmission Data (for each absorber in each channel)
SRD	Spectral Response Data (21 channels))
FIR	FIR Filter Coefficients (21 channels)
FOV	Field of View (21 detectors)
FME	Forward Model Error (21 channels)
APR	A priori (for each target retrieved)
APE	A priori covariance (for each target retrieved)
CLI	Climatologies (for each absorber)
GRD	Gridded fields (e.g. EOS-CHEM data)
GAD	Gridded advected fields (e.g. EOS-CHEM data)
LOS	Line of sight gradients
NLT	Non-LTE source function parameterized data

Table 17: Level-2 Processing Required Input Data Sets

5.1.3 Metadata

The primary purpose of metadata is to assist with the efficient distribution (e.g. via easy access) and subsequent analysis of data sets. Since data volumes are so large, information about the data (metadata) is used to represent the data to search engines or data base queries, rather than searching the data itself. It is the intent of the HIRDLS Science Data Processing System to follow ECS guidelines regarding metadata.

5.1.4 Browse Data

Strictly speaking browse data is used in the ECS model as a quick look at a data granule in order to help a data user make a decision about ordering the associated data. An example would be a 16 km water vapor global (false color representation) map rendering for a given day. Generally, browse data could take on any format that allows a quick and concise summary of data, instrument activities and data quality. As part of HIRDLS data quality assurance activities, browse data become an integral component in the overall effort of improving data user information and data quality.

5.1.5 Data Processing Requirements

Table 18 shows a summary of Level-2 CPU and disk space requirements for HIRDLS data processing. Level-1 and higher levels are shown for completeness and comparison. The values for CPU were derived from UARS ISAMS software timings, which used computationally similar algorithms. The units in column two represent the MFLOPs (million floating-point operations per second) required to process one day of data. Here MFLOPS is defined as the power needed to process 24 hours of data in 24 hours. To process 24 hours of data, and not fall behind the data acquisition rate would require a 2800 MFLOPs machine. For comparison an eight-processor SGI Origin 2000 (300 Mhz) is rated at around 4000 MFLOPs (with perfect parallellization).

Product	CPU (MFLOP)	Disk (MBytes)
Level-1	12	710
Level-2	2280	175
Level-3	<1	80
Level-4(GPH)	<1	1

Table 18: Standard Data Product Processing and Disk Space Requirements.

5.2   Parallel Coding

There are various ways to approach developing code for a parallel processing computer system. Typically these techniques are applied individually, or in combination, to different architectures and software configurations to maximize performance. The most straightforward approach is to use compiler directives to schedule do-loop iterations on different processors. Just behind this in order of complexity is high-level script scheduling which uses a scripting language such as Perl to schedule jobs on specific processors via the network and operating system. Although both methods can be effective, the do-loop level scheduling is the easiest to implement for a given day of data, and offers the most flexibility and control over which operations can be scheduled. The scripting approach can be problematic when attempting to split (and later reassemble) data granules into independent smaller granules that can then be assigned to processors. However, for reprocessing efforts that require no sub-setting, the scripting approach will be evaluated to determine its viability. In either case the overall goal is the simultaneous execution of individual components.

Based upon preliminary test data from MOPITT using an SGI Origin 2000 six-processor system, the plan for HIRDLS standard data product generation software is to use high level do-loop scheduling. These tests indicate that this technique should provide a doubling of data throughput going from one processor to two, and a subsequent gain of triple data throughput going to four processors. The advantage of this approach is minimal administrative overhead, straightforward down-stream implementation, and relatively good performance.

5.3   Exception Handling

The exact nature of processing environment for the EOS-CHEM platform has not yet been identified as of this writing. However, whether in a SIPS or DAAC based processing environment certain generic exception handling characteristics can be identified even though the exact mechanisms have yet to be defined. Generally an exception is an event triggered by the data processing code that prevents continuation. Exceptions can range from nonexistent input data to logical programming errors that force the process to stop. Currently there are five areas of exception handling that we have identified for potential implementation. Table 19 lists these exception categories.

Category	Description
Resource	Missing input data files
Logic	Programming error (including unidentified errors)
Instrument	Instrument state precludes normal operation
System	External condition (I/O, disk space)
User	User set-up prevents normal execution

Table 19: Exception Categories

When events are triggered they must somehow be captured and acted upon. This is typically accomplished through a system of language specific statements, followed by a standard library call depending on the type of exception.

5.4 Diagnostic Software

Diagnostic software tools are needed in order to investigate and resolve problems and generally bring visibility to processes and their related data. The HIRDLS Science Data Processing team is planning to use a suite of diagnostic tools that was developed for use on the UARS/HALOE project. The tools and underlying data format were used extensively for diagnostic analysis and routine visualization and generation of browse products. The software, built around the Interactive Data Language, a standard data format and Perl, allow developers and scientists to quickly build access, analysis and display scenarios. An access tool is currently under construction that will allow HIRDLS HDF-EOS files to be interfaced to the HALOE tool suite. The core functionality of the tools include: selection, display (color cross sections and line plots), comparisons (coincidence finding and statistics).

6 Calibration and Validation

6.1 Pre-launch Calibration Plan

The accuracy and precision of retrieved science data depends critically on knowledge of the instrument response to incident radiation. It is the purpose of pre-launch instrument testing and calibration to quantify the response of the instrument over a range of operating conditions to very precise levels. The details of the instrument calibration and testing can be found in the Pre-launch Calibration Plan (TP-HIR-007) and in the HIRDLS Proto-Flight Model Instrument Test Plan (TP-LOC-204). An overview of the calibration and testing plan is presented below.

Instrument level functional and performance testing at the instrument integrator's facility will include tests to verify the instrument performs to the required levels and that the instrument response is stable and repeatable. Measurements of the relative FOV response, the positions of detector FOV, out-of-field response, radiometric response and spectral response will be made over the entire range of elevation and azimuth angles. In addition, the scan mirror encoders, and mirror temperature sensor will be characterized and calibrated at the subsystem level.

Formal instrument calibration will be performed at the Oxford University test and calibration facility. The instrument will be in a thermal-vacuum chamber with the instrument surrounded by temperature controlled walls and mounted on an optical table along with radiometric test equipment, and isolated from mechanical vibrations. Testing will be performed under operations conditions that closely simulate the expected on-orbit environment.

The absolute radiometric response to a known laboratory source, varied over a range of source temperatures, will be measured. A separate test of response linearity will be made using a linearity mask to characterize small-scale departures from a linear response. In addition, the in-flight calibrator will be calibrated against a standard laboratory source. Precise knowledge of the relative spectral response of each of the 21 science channels to the 1% level is necessary for inclusion in the data processing algorithms. Measurements by a vacuum compatible monochromator will be made to the required sensitivity. A lower resolution search for out-of-band spectral leaks of the order of 0.1% of the peak in-band response will be made.

The spectral modeling study in Section 2.4.1 assumes the channel filter spectral responses obtained from the Infrared Multilayer Laboratory at the University of Reading. The actual end to end channel responses will need to be accurately characterized in the testing and calibration phase. This is to ensure that the passbands are accurately known to within the specifications determined in the Instrument Requirements Document and therefore can be used to achieve the HIRDLS measurement goals. The frequency at which the response is measured must be known to $0.2 \ \mathrm{cm}^{-1}$, and the relative spectral response to unpolarized radiation, between those frequencies at which it falls to 1%, must be known at about the one percent level. The out-of-band response of the filter is also an important consideration. This is defined as the total integrated response outside of the points where the relative spectral response is 0.2 %. When viewing the atmosphere, it is desirable that the out-of-band radiance not be more than about a percent of the in-band radiance or of the same order as the NER, whichever is greater. In conclusion, it will be very important that any out-of-band spectral leaks, response asymmetries, 'shoulders' or 'notches' in the instrument channel response, are determined and accounted for in the forward modeling used in the data analysis. Measurements will be made to the required sensitivity to detect out-of-band spectral leaks of the order of 0.1 % of the peak in-band response.

Knowledge of the relative vertical spatial response is necessary for inclusion in the data processing algorithms and therefore, the spatial response of each of the 21 spectral channels will be measured using a narrow slit with an

accuracy of ± 0.5 % of the peak response and with adequate angular resolution to resolve small-scale variations in the response. The relative positions of the detector fields-of-view will be mapped. Response to radiation occurring at off-axis angles will be characterized.

6.2   Science Data Validation Plan

The goal of the validation effort is to determine the accuracy and precision of the various HIRDLS science data, and consequently the appropriateness of their use in future scientific investigations. Post-launch activities include refinement of data processing algorithms, and uncertainty estimates based on in-flight instrument analyses and comparisons with correlative data. A brief summary of the validation approach is presented here; details of the validation plan are given in the HIRDLS Scientific Data Product Validation Plan (SC-HIR-022).

Pre-launch validation activities involve the pre-launch calibration and testing of the instrument which includes measuring the spectral, spatial, and absolute radiometric response of each of the HIRDLS 21 spectral channels over a range of operating conditions and over the range of scan angles. These data are a required input to the Level-2 data processing algorithms. In addition, calibration and test data will be used to develop an instrument model to be used in end-to-end simulations of the measurement and retrieval process to test and validate the data processing procedures. Using the end-to-end simulations, an objective analysis can be used to determine the expected on-orbit instrument performance and the magnitude of expected errors in retrieved quantities to be compared with post-launch analyses.

The purpose of the post-launch validation activities is to gather the necessary information to provide meaningful estimates of the uncertainties associated with the HIRDLS science data products. In order to begin the validation process, the on-orbit characteristics of the HIRDLS instrument must be well understood. This will be accomplished by analysis of the raw instrument counts, referred to as Level-0 data, and engineering data. The first level of processed data, the calibrated and geo-located radiance profiles (Level-1) will be validated in a variety of ways to assure that the observed radiances are correct and internally self consistent.

After the measurement process and its uncertainties are well understood, early validation studies will be conducted in regions where the signals are largest and where contributions from interfering gases and aerosols are minimal. Thus, comparisons of temperature, ozone and water vapor in the stratosphere and mesosphere will allow an early search for any anomalies in the instrument or retrieval algorithms. Since these may affect the retrievals of species with smaller signals, this is also a necessary precursor step. The validation effort will then be extended to include the lower stratosphere and upper troposphere where contributions from aerosols and other interfering species become significant. This will require the aerosol channels to be validated first and then their affects on other channels quantified. Finally, the validation study will be extended to include a range of atmospheric and observational conditions.

The validation of the retrieved temperature and constituent profiles will include a detailed estimation of errors from all sources, examination for spatial and temporal consistency of the retrieved profiles, comparison of retrieved profiles with climatological data, and a comparison of retrieved profiles with simultaneous correlative measurements. Comparison will be made, wherever possible, with data from MLS and TES, on the same spacecraft, and looking at the same atmosphere at close to the same times. These coincident observations have the advantages that they allow comparisons at all latitudes and longitudes. Additionally, comparisons will be made with other correlative data sources such as radiosondes, lidars, infrared and microwave instruments at NDSC and other ground-based sites.

It is recognized that validation of HIRDLS observations in the upper troposphere and lower stratosphere will be challenging because of the presence of aerosols and other interfering species in many of the HIRDLS spectral channels, and because of the strong horizontal gradients along the line-of-sight. This region will require comparisons of HIRDLS data with aircraft measurements. There are currently several instruments flying on airborne platforms that can provide correlative data for the HIRDLS instrument. For example UV photometer, chemiluminescence, and lidar instruments are available for measuring ozone from aircraft. Additionally, TDL absorption techniques can be used to measure water vapor, CH_4, N_2O, HNO_3 and NO_2 from aircraft. Aerosols and cloud particle parameters can be derived from CN counters, FCAS, FSSP, MASP and wire impactors.

7 Quality Control and Diagnostics

The EOS Data Quality Panel has defined data product quality assurance as the process by which data granule content is determined to meet expected standards of accuracy and flagged in instances where standards are not met. Quality assurance (Q/A) procedures are expected to take place within the operational time window of EOS standard product generation and may take place at the Product Generation Facility or at the instrument SCF. Thus, Q/A can best be thought of as activities which take place shortly after the creation of an individual data product granule whereas validation covers a wider scope of effort taking place over longer periods of time and applies to entire collections of granules.

In addition to data product quality assurance, the Data Panel has identified 3 other areas of data product quality control which are strongly related and have synergistic coupling to the data processing required to meet quality assurance goals. These areas include a) instrument calibration, b) instrument performance monitoring and c) data product validation. A HIRDLS Q/A Plan will be developed to both meet the goals for data product quality assurance and to provide sources of information necessary to supplement activities in the other three areas.

Although the Data Quality Panel has drawn a distinction between calibration, instrument monitoring, data product quality assurance and data product validation, the activities are interrelated and have some common requirements in terms of basic information that must be acquired and analyzed to support each. The activities "upstream" of product generation (instrument calibration and on-orbit instrument operation and performance) have a direct bearing on the suitability of data products for use by researchers and must be considered in the overall product quality assessment.

7.1 Quality Assurance Requirements

In order for the goals stated in the previous section to be met, it will be necessary for the HIRDLS team to develop a Data Product Q/A Plan. This plan can best be prepared after the details of data product content have been finalized. For the purpose of this document, only requirements for the Level-2 product will be considered.

No formal EOS list of requirements for quality assurance exists at present. However, within a broad context the following may be deduced from the Draft ESDIS Project Q/A Plan (Lutz, 1995):

- Q/A of data products is an Instrument Team (IT) responsibility. Thus it is up to ITs to determine how each of their products should be handled.

- Instrument Teams are to prepare a Q/A Plan and submit it to ESDIS for approval.

- Specific, standard metadata items identified within the ECS data model must reflect the Q/A status for each granule.

- Instrument teams may elect to provide separate Q/A products to be associated with corresponding data products.

- Instrument teams may elect to include product specific metadata attributes within the data product to convey Q/A information to end-users.

- Q/A activities are to be completed within an "operational time window" of a few hours following data granule creation.

7.2 Quality Assurance Approach

HIRDLS quality assurance will be performed by a combination of automated procedures within the Product Generation Executables (PGEs) running at the Product Generation Facility and by human assessment of processing summaries, assisted by software tools, at the HIRDLS Science Computing Facility (SCF). During the PGE execution various limit and exception checking is done on inputs and intermediate results within the main processor modules during data product generation. Exceptions are logged in temporary files for use during the Q/A phase of the PGE. The PGE Q/A phase generates various summary diagnostics from these exception logs and extracts other

information from the data product that has just been produced and at the same time creates any browse products that might be required. Information from both sources is formatted in a manner appropriate for display and review by SCF personnel who will monitor product generation routinely. Following review by SCF personnel, appropriate granule level metadata are entered into the system. During normal working hours, it is expected that SCF review can be completed in less than 4 hours. The steps are illustrated in Figure 42.
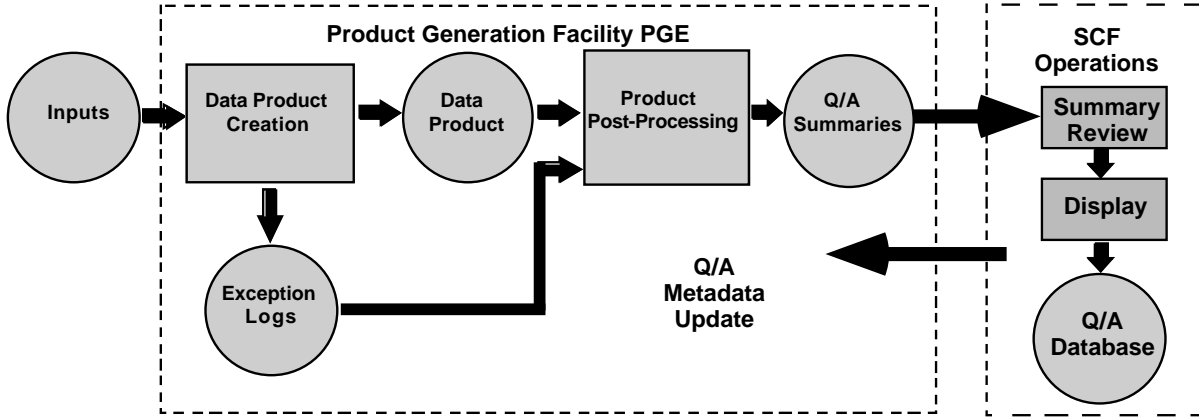
Figure 42: HIRDLS Level-2 Q/A Data Flow

The amount of Q/A information returned to the SCF can be controlled by configuration files for the PGE. It is expected that more information will be required in the immediate post-launch period while confidence in the Q/A summaries is gradually developed. During nominal operations, the volume of Q/A diagnostics can be reduced. However, if instrument on-orbit anomalies occur or if peculiarities in the data products are seen, the more verbose forms of diagnostic information may be re-invoked. The exception log files used in the granule Q/A summary generation will be retained at the Product Generation Facility for a few days after processing in case it is necessary for SCF staff to retrieve them for more detailed Q/A analysis.

Q/A summaries will contain both graphical and tabular data. Graphical data will include standard browse products as well as additional displays showing spatial and temporal representations of selected diagnostics. Tabular data will include statistics of various parameters as well as summaries of various algorithm and data exceptions. Selected Q/A diagnostics will be entered into a Q/A database maintained at the SCF in order that long-term trends may be monitored. It is expected that these trends will assist the HIRDLS instrument team in assessing instrument performance characteristics and the science team in carrying out data product validation activities.

These procedures will be applied to all standard product data granules produced at the DAAC. In addition, selected data granules will be examined in detail at science team facilities as part of the data product validation effort. Problems uncovered during these activities may alter subsequent Q/A procedures by requiring that additional parameters be examined or diagnostics be defined. However, data validation inspections will take place apart from Q/A operations and will not affect the timeliness of data product availability.

A   Radiance and Weighting Function Calculations

A.1   Radiance calculation

The ray path in Figure A.1 is defined by the line-of-sight coordinate index, j, which increases from $j = 0$ closest to the instrument to $j = n$ at space. The atmospheric transmittance through element, j, is denoted by $\Delta\tau_j$ and the
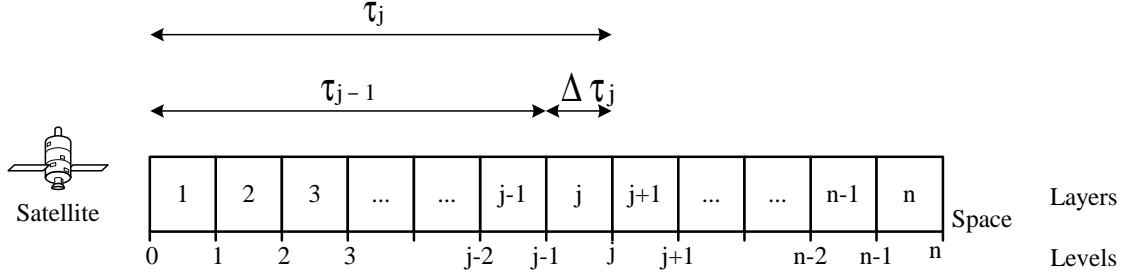
Figure A.1: Line-of-sight coordinates.

LTE emission from the element is $B_j(1 - \Delta\tau_j)$.

$$
\begin{aligned}
\tau_j^s &= \text{transmittance of path from level } j \text{ to level } s \\
\tau_j = \tau_j^0 &= \text{transmittance of path from level } j \text{ to satellite at } j = 0 \\
\chi_j &= \text{optical depth of path from level } j \text{ to satellite at } j = 0 \\
\Delta\tau_j &= \text{transmitance of element, } j \\
\Delta\chi_j &= \text{optical depth of element, } j \\
\Delta\tau_j &= \tau_j/\tau_{j-1} \\
D\tau_j &= \tau_{j-1} - \tau_j = \tau_{j-1}(1 - \Delta\tau_j) \\
\kappa_{kj} &= \text{absorption coefficient } [m^2 \; mol^{-1}] \text{ of absorber, } k, \text{ in element, } j \\
u_{kj} &= \text{column amount } [mol \; m^{-2}] \text{ of absorber, } k, \text{ in element, } j \\
u_{ks} &= \int v_{ks}\frac{\rho_s}{M_r}ds = \int v_{ks}\frac{p_s}{RT_s} \\
T_j &= \text{temperature,} [K], \text{ at level, } j \\
\bar{T}_{kj} &= \text{Curtis-Godson mean layer temperature, } [K], \text{ for absorber, } k, \text{ in element, } j \\
&= \frac{1}{u_{kj}}\int \frac{\partial u(s)}{\partial s} \, T(s) \, ds \\
\bar{T}_j &= \text{optical depth weighted mean layer temperature, } [K], \text{ of element, } j \\
&= \frac{\sum_k \Delta\chi_{kj} \, \bar{T}_{kj}}{\sum_k \Delta\chi_{kj}} \\
B_j &= B(\bar{T}_j), \quad \text{Planck function for element, } j \\
p_j &= \text{pressure,} [mb], \text{ at level, } j \\
\bar{p}_{kj} &= \text{Curtis-Godson mean layer pressure, } [mb], \text{ for absorber, } k, \text{ in element, } j \\
&= \frac{1}{u_{kj}}\int \frac{\partial u(s)}{\partial s} \, p(s) \, ds \\
\bar{p}_j &= \text{mean layer pressure, } [mb], \text{ of element, } j
\end{aligned}
\tag{A.1}
$$

The radiance emerging from the element boundary closer to the instrument, L_{j-1}, is obtained from the transmission of the radiation incident on the element, L_j, and the emission within the element, which leads to a recurrence relation,

$$
L_{j-1} = L_j \Delta\tau_j + B_j(1 - \Delta\tau_j)
\tag{A.2}
$$

We want to calculate the radiance, L_s, at an arbitrary level, s (n.b. the radiance at the instrument is $R = L_0$).

$B_0 = B_{n+1} = 0$ i.e. cold space at beginning and end of path

$\Delta\tau_0 = \Delta\tau_{n+1} = 1$ i.e. transparent at beginning and end of path

$L_n = 0$ i.e. cold space radiance

$L_{n-1} = L_n \Delta\tau_n + B_n(1 - \Delta\tau_n)$

$L_{n-2} = L_{n-1}\Delta\tau_{n-1} + B_{n-1}(1 - \Delta\tau_{n-1})$
$\quad\ = B_n(1 - \Delta\tau_n)\Delta\tau_{n-1} + B_{n-1}(1 - \Delta\tau_{n-1})$

$L_{n-3} = L_{n-2}\Delta\tau_{n-2} + B_{n-2}(1 - \Delta\tau_{n-2})$
$\quad\ = [B_n(1 - \Delta\tau_n)\Delta\tau_{n-1} + B_{n-1}(1 - \Delta\tau_{n-1})]\Delta\tau_{n-2} + B_{n-2}(1 - \Delta\tau_{n-2})$
$\quad\ = B_n(1 - \Delta\tau_n)\Delta\tau_{n-1}\Delta\tau_{n-2} + B_{n-1}(1 - \Delta\tau_{n-1})\Delta\tau_{n-2} + B_{n-2}(1 - \Delta\tau_{n-2})$

$\vdots$

$$L_s = B_n(1 - \Delta\tau_n)\Delta\tau_{n-1}\Delta\tau_{n-2}\ldots\Delta\tau_{s+1} \tag{A.3}$$
$$\qquad + B_{n-1}(1 - \Delta\tau_{n-1})\Delta\tau_{n-2}\Delta\tau_{n-3}\ldots\Delta\tau_{s+1} + \ldots + B_{s+1}(1 - \Delta\tau_{s+1})$$
$$= B_n\left(\prod_{i=s+1}^{n-1}\Delta\tau_i - \prod_{i=s+1}^{n}\Delta\tau_i\right) + B_{n-1}\left(\prod_{i=s+1}^{n-2}\Delta\tau_i - \prod_{i=s+1}^{n-1}\Delta\tau_i\right) + \ldots + B_{s+1}(1 - \Delta\tau_{s+1})$$
$$= \sum_{j=s+2}^{n} B_j\left(\prod_{i=s+2}^{j}\Delta\tau_{s-1} - \prod_{i=s+1}^{j}\Delta\tau_s\right) + B_{s+1}(1 - \Delta\tau_{s+1})$$
$$= \sum_{j=s+2}^{n} B_j(\tau_{j-1}^{s} - \tau_j^{s}) + B_{s+1}(\tau_s^{s} - \tau_{s+1}^{s}) \quad \text{where} \quad \tau_j^{s} = \prod_{i=s+1}^{j}\Delta\tau_i \quad \text{and} \quad \tau_s^{s} = 1$$
$$= \sum_{j=s+1}^{n} B_j(\tau_{j-1}^{s} - \tau_j^{s}) = \sum_{j=s+1}^{n} B_j D\tau_j$$

Hence, the radiance at the instrument (i.e. for $s = 0$) can be written as (dropping the superscripts so that $\tau_j = \tau_j^0$),

$$R = L_0 = \sum_{j=1}^{n} B_j(\tau_{j-1} - \tau_j) = \sum_{j=1}^{n} B_j D\tau_j \quad \text{where} \quad \tau_j = \prod_{i=1}^{j}\Delta\tau_i \tag{A.4}$$

It will be convenient to work with an equivalent formulation,

$$R = \sum_{j=0}^{n} b_j\tau_j \quad \text{where } \tau_0 = 1, B_0 = B_{n+1} = 0$$
$$b_j = \begin{cases} B_1 & j = 0 \\ (B_{j+1} - B_j) & 1 \le j \le n - 1 \\ -B_n & j = n \end{cases} \tag{A.5}$$

We will also make use of a partial sum evaluated at a particular level, s, along the line-of-sight,

$$P_s = \sum_{j=s}^{n} b_j\tau_j = \tau_s^0 \sum_{j=s}^{n} b_j\tau_j^{s} = \tau_s(L_s - B_s) \tag{A.6}$$

A.2   Derivatives

We require the derivatives of the radiance at the instrument with respect to several atmospheric parameters. It is convenient to work with layer quantities, $\bar{q}$, and to convert the derivatives to level quantities, q, using,

---

$$\frac{\partial R}{\partial q_l} = \sum_i \frac{\partial R}{\partial \bar{q}_i} \frac{\partial \bar{q}_i}{\partial q_l} \tag{A.7}$$

The transmittance of the path, τ_j, from $s = 0$ to $s = j$, is given by the product of the transmittances of the individual absorbers, τ_{kj},

$$\tau_j = \prod_k \tau_{kj} \quad \text{where } \tau_{k0} = 1 \tag{A.8}$$

We define the following coefficients,

$$a_{kj} = \frac{\partial \tau_j}{\partial \tau_{kj}} = \prod_{k' \neq k} \tau_{k'j} \tag{A.9}$$

$$t_{kj} = b_j \, a_{kj}$$

which allows us to write the radiance at the instrument as,

$$R = \sum_{j=0}^n b_j \, \tau_j = \sum_{j=0}^n t_{kj} \, \tau_{kj} \tag{A.10}$$

From Eqn A.10 we obtain the derivative with respect to a change in the total transmittance of the path from $s = 0$ to $s = j$,

$$\frac{\partial R}{\partial \tau_j} = b_j \tag{A.11}$$

and the derivative with respect to a change in the transmittance of the path from $s = 0$ to $s = j$ due to a single absorber, k,

$$\frac{\partial R}{\partial \tau_{kj}} = t_{kj} \tag{A.12}$$

The total optical depth of the path, χ_j, from $j' = 0$ to $j' = j$, is the sum of the optical depth contributions, χ_{kj}, due to the individual absorbers, k,

$$\chi_j = \sum_k \chi_{kj}$$

$$\chi_{kj} = \sum_{j'=0}^j \Delta \chi_{kj'} \tag{A.13}$$

$$\Delta \chi_{ks} = \kappa_{ks} \, u_{ks}$$

where $\Delta \chi_{ks}$ is the optical depth of the path element, s, the absorption coefficient is κ_{ks} and the column amount of absorber, k, is u_{ks}. The total transmittance of the path, τ_j, from $s = 0$ to $s = j$, is given by,

$$\tau_j = \exp(-\chi_j) \quad ; \quad \frac{\partial \tau_j}{\partial \chi_j} = -\tau_j \tag{A.14}$$

and similarly the contribution to the transmittance of the path, τ_{kj}, by absorber, k, is given by,

$$\tau_{kj} = \exp(-\chi_{kj}) \quad ; \quad \frac{\partial \tau_{kj}}{\partial \chi_{kj}} = -\tau_{kj} \tag{A.15}$$

Consider a perturbation to a layer quantity, $\bar{q}_s$ or $\bar{q}_{ks}$, within a single line-of-sight element, s. Then from Eqn A.10 we obtain the resulting change in the radiance due to a change in the line-of-sight element quantity,

$$\frac{\partial R}{\partial \bar{q}_s} = \sum_{j=0}^{n} \left(\frac{\partial R}{\partial b_j} \frac{\partial b_j}{\partial \bar{q}_s} + \frac{\partial R}{\partial \tau_j} \frac{\partial \tau_j}{\partial \bar{q}_s} \right)$$

$$\frac{\partial R}{\partial \bar{q}_{ks}} = \sum_{j=0}^{n} \left(\frac{\partial R}{\partial t_{kj}} \frac{\partial t_{kj}}{\partial \bar{q}_{ks}} + \frac{\partial R}{\partial \tau_{kj}} \frac{\partial \tau_{kj}}{\partial \bar{q}_{ks}} \right) \tag{A.16}$$

In Eqn A.16 we require the following derivatives with respect to layer absorber amount, $\bar{q}_{ks} = u_{ks}$, and layer temperature, $\bar{q}_s = \bar{T}_s$, (using Eqn A.13),

$$\frac{\partial \tau_{kj}}{\partial u_{ks}} = \frac{\partial \tau_{kj}}{\partial \chi_{kj}} \frac{\partial \chi_{kj}}{\partial u_{ks}}$$

$$\frac{\partial \chi_{kj}}{\partial u_{ks}} = \begin{cases} \kappa_{ks} & j \geq s \\ 0 & j < s \end{cases} \tag{A.17}$$

and

$$\frac{\partial \tau_j}{\partial \bar{T}_s} = \frac{\partial \tau_j}{\partial \chi_j} \left(\frac{\partial \chi_j}{\partial \bar{T}_s} + \frac{\partial \chi_j}{\partial \bar{p}_j} \frac{\partial \bar{p}_j}{\partial \bar{T}_s} \right)$$

$$\frac{\partial \chi_j}{\partial \bar{T}_s} = \begin{cases} \sum_k \left(u_{ks} \frac{\partial \kappa_{ks}}{\partial \bar{T}_s} + \kappa_{kj} \frac{\partial u_{kj}}{\partial \bar{T}_s} \right) & j \geq s \\ \sum_k \left(\kappa_{kj} \frac{\partial u_{kj}}{\partial \bar{T}_s} \right) & j < s \end{cases}$$

$$\frac{\partial \chi_j}{\partial \bar{p}_j} = \sum_k \left(u_{kj} \frac{\partial \kappa_{kj}}{\partial \bar{p}_j} + \kappa_{kj} \frac{\partial u_{kj}}{\partial \bar{p}_j} \right) \tag{A.18}$$

A.2.1 Volume mixing ratio derivative

We calculate the derivative of the radiance with respect to a logarithmic change in the layer amount, $\ln u_{ks}$, of the absorber, k, in a line-of-sight element, s.
Since,

$$\frac{\partial R}{\partial \ln u_{ks}} = u_{ks} \frac{\partial R}{\partial u_{ks}} \tag{A.19}$$

multiplying Eqn A.16 by u_{ks} and noting from Eqn A.9 that $\partial t_{kj}/\partial u_{ks} = 0$ we obtain,

$$u_{ks} \frac{\partial R}{\partial u_{ks}} = u_{ks} \sum_{j=0}^{n} \frac{\partial R}{\partial \tau_{kj}} \frac{\partial \tau_{kj}}{\partial u_{ks}} \tag{A.20}$$

Hence substituting from Eqns A.12, A.15 and A.17 we have,

$$
\begin{aligned}
u_{ks}\frac{\partial R}{\partial u_{ks}} &= u_{ks}\sum_{j=0}^{n}\frac{\partial R}{\partial \tau_{kj}}\frac{\partial \tau_{kj}}{\partial \chi_{kj}}\frac{\partial \chi_{kj}}{\partial u_{ks}} \\
&= u_{ks}\sum_{j=s}^{n}t_{kj}.(-\tau_{kj}).\kappa_{ks} \\
&= -\kappa_{ks}u_{ks}\sum_{j=s}^{n}t_{kj}\ \tau_{kj} \\
&= -\Delta\chi_{ks}\sum_{j=s}^{n}b_j\ \tau_j \\
&= -\Delta\chi_{ks}P_s
\end{aligned}
\tag{A.21}
$$

Therefore,

$$
\frac{\partial R}{\partial \ln u_{ks}} = -\Delta\chi_{ks}P_s = \Delta\chi_{ks}\tau_s\left(B_s - L_s\right)
\tag{A.22}
$$

The derivatives corresponding to the volume mixing ratio defined on levels are obtained from Eqn A.7,

$$
\frac{\partial R}{\partial \ln v_{ks}} = \sum_i \frac{\partial R}{\partial \ln u_{ki}}\frac{\partial \ln u_{ki}}{\partial \ln v_{ks}}
\tag{A.23}
$$

A.2.2   Temperature derivative

We calculate the derivative of the radiance with respect to a change in the layer temperature, $\bar{T}_s$, in a line-of-sight element, s. From Eqn A.16,

$$
\frac{\partial R}{\partial \bar{T}_s} = \sum_{j=0}^{n}\frac{\partial R}{\partial b_j}\ \frac{\partial b_j}{\partial \bar{T}_s} + \sum_{j=0}^{n}\frac{\partial R}{\partial \tau_j}\ \frac{\partial \tau_j}{\partial \bar{T}_s}
\tag{A.24}
$$

Substituting from Eqn A.11 and using the definition of b_j from Eqn A.5 and additionally noting that $B_0 = B_{n+1} = 0$, we can rewrite the first term of Eqn A.24 as,

$$
\begin{aligned}
\sum_{j=0}^{n}\frac{\partial R}{\partial b_j}\ \frac{\partial b_j}{\partial \bar{T}_s} &= \sum_{j=0}^{n}\tau_j\frac{\partial b_j}{\partial \bar{T}_s} = \sum_{j=0}^{n}\tau_j\left(\frac{\partial B_{j+1}}{\partial \bar{T}_s} - \frac{\partial B_j}{\partial \bar{T}_s}\right) \\
&= (\tau_{s-1} - \tau_s)\frac{\partial B_s}{\partial \bar{T}_s}\quad\text{since }\frac{\partial B_j}{\partial \bar{T}_s}=0\text{ if }j\neq s \\
&= D\tau_s\frac{\partial B_s}{\partial \bar{T}_s} = \tau_{s-1}(1-\Delta\tau_s)\frac{\partial B_s}{\partial \bar{T}_s}
\end{aligned}
\tag{A.25}
$$

Substituting Eqn A.25 into Eqn A.24 and using Eqns A.11, A.14 and A.18 we have,

$$\frac{\partial R}{\partial \bar{T}_s} = D\tau_s \frac{\partial B_s}{\partial \bar{T}_s} + \sum_{j=0}^{n} \frac{\partial R}{\partial \tau_j} \frac{\partial \tau_j}{\partial \chi_j} \left(\frac{\partial \chi_j}{\partial \bar{T}_s} + \frac{\partial \chi_j}{\partial \bar{p}_j} \frac{\partial \bar{p}_j}{\partial \bar{T}_s} \right)$$

$$= D\tau_s \frac{\partial B_s}{\partial \bar{T}_s} - \sum_{j=0}^{n} b_j \tau_j \frac{\partial \chi_j}{\partial \bar{T}_s} - \sum_{j=0}^{n} b_j \tau_j \frac{\partial \chi_j}{\partial \bar{p}_j} \frac{\partial \bar{p}_j}{\partial \bar{T}_s}$$

$$= D\tau_s \frac{\partial B_s}{\partial \bar{T}_s}$$

$$\quad - \sum_{j=s}^{n} b_j \tau_j \sum_k \left(u_{ks} \frac{\partial \kappa_{ks}}{\partial \bar{T}_s} \right)$$

$$\quad - \sum_{j=s}^{n} b_j \tau_j \sum_k \left(\kappa_{kj} \frac{\partial u_{kj}}{\partial \bar{T}_s} \right) \tag{A.26}$$

$$\quad - \sum_{j=0}^{n} b_j \tau_j \sum_k \left(u_{ks} \frac{\partial \kappa_{ks}}{\partial \bar{p}_j} \right) \frac{\partial \bar{p}_j}{\partial \bar{T}_s}$$

$$\quad - \sum_{j=0}^{n} b_j \tau_j \sum_k \left(\kappa_{kj} \frac{\partial u_{kj}}{\partial \bar{p}_j} \right) \frac{\partial \bar{p}_j}{\partial \bar{T}_s}$$

$$= D\tau_s \frac{\partial B_s}{\partial \bar{T}_s} - P_s \sum_k \left(u_{ks} \frac{\partial \kappa_{ks}}{\partial \bar{T}_s} \right) - P_s \sum_k \left(\kappa_{ks} \frac{\partial u_{ks}}{\partial \bar{T}_s} \right)$$

$$\quad - \sum_{j=0}^{n} b_j \tau_j \sum_k \left(u_{ks} \frac{\partial \kappa_{ks}}{\partial \bar{p}_j} \right) \frac{\partial \bar{p}_j}{\partial \bar{T}_s} - \sum_{j=0}^{n} b_j \tau_j \sum_k \left(\kappa_{kj} \frac{\partial u_{kj}}{\partial \bar{p}_j} \right) \frac{\partial \bar{p}_j}{\partial \bar{T}_s}$$

The Planck function and its temperature derivative are given by

$$B(T) = \frac{c_1 \nu^3}{e^x - 1}$$
$$\frac{\partial B}{\partial T} = B(T) \left(\frac{x}{T} \right) \frac{1}{1 - e^{-x}}$$
$$\text{where} \quad x = \frac{c_2 \nu}{T} \tag{A.27}$$
$$c_1 = 2hc^2 = 1.19104 \times 10^{-8} \quad \text{W/(m}^2\text{.sr.cm}^{-4})$$
$$c_2 = hc/k = 1.439 \quad \text{K/cm}^{-1}$$

where h, k and c are the Planck constant, Boltzmann constant and speed of light, respectively.
The derivatives corresponding to the temperature defined on levels are obtained from Eqn A.7,

$$\frac{\partial R}{\partial T_s} = \sum_i \frac{\partial R}{\partial \bar{T}_i} \frac{\partial \bar{T}_i}{\partial T_s} \tag{A.28}$$

A.2.3 Aerosol derivatives

The aerosol spectral factor which relates the extinction in a channel at wavelength, λ^c, to the extinction at a reference wavelength, λ^0, for a given composition, η, and effective radius, r_e, is,

$$F^c(\lambda^c, \eta, r_e) \tag{A.29}$$

For gas, k, the absorber amount, u_{ks} $[mol \ m^{-2}]$ in the line-of-sight element, s, is given by,

$$u_{ks} = \int v_{ks} \frac{\rho}{M_r} ds \qquad (A.30)$$

where v_{ks} is the volume mixing ratio, $\rho/M_r \; [mol \; m^{-3}]$ is the molar air density and the optical depth is,

$$\Delta\chi = \kappa_{ks} \, u_{ks} \qquad (A.31)$$

where $\kappa_{ks} \; [m^2 \; mol^{-1}]$ is the absorption coefficient.
We can treat aerosols in an analogous manner if we define the aerosol extinction, $\beta \; [m^{-1}]$ as,

$$\beta_{\lambda^0 s} = v'_{\lambda^0 s} \frac{\rho}{M_r} \qquad (A.32)$$

where $v'_{\lambda^0 s} \; [m^2 \; mol^{-1}]$ is the aerosol extinction cross-section at the reference wavelength. The optical depth at the reference wavelength, λ_0, is,

$$u'_{\lambda^0 s} = \int \beta_{\lambda^0 s} ds = \int v'_{\lambda^0 s} \frac{\rho}{M_r} ds \qquad (A.33)$$

The optical depth for a particular channel wavelength, λ_c is,

$$\Delta\chi_{\lambda^c s} = \kappa'_{\lambda^c s} u'_{\lambda^0 s} \qquad (A.34)$$

where $\kappa'_{\lambda^c s}$ is the dimensionless aerosol spectral factor used to convert from the reference wavelength to the channel wavelength,

$$\kappa'_{\lambda^c s} = F^c(\lambda^c, \eta_s, r_{e_s}) \qquad (A.35)$$

The derivatives required to calculate the weighting functions are obtained from Eqns A.13 and A.34,

$$\frac{\partial \chi_{\lambda^c j}}{\partial u'_{\lambda^0 s}} = \kappa'_{\lambda^c s}$$

$$\frac{\partial \chi_j}{\partial \bar{T}_s} = \left[u'_{\lambda^0 s} \frac{\partial \kappa'_{\lambda^c s}}{\partial \bar{T}_s} + \kappa'_{\lambda^c j} \frac{\partial u'_{\lambda^0 j}}{\partial \bar{T}_s} \right] \qquad (A.36)$$

$$\frac{\partial \chi_j}{\partial \bar{r}_{e_s}} = \left[u'_{\lambda^0 s} \frac{\partial \kappa'_{\lambda^c s}}{\partial \bar{r}_{e_s}} + \kappa'_{\lambda^c s} \frac{\partial u'_{\lambda^0 s}}{\partial \bar{r}_{e_s}} \right]$$

These equations are analogous to those for gases in Eqns A.17 and A.18. Following the analyses of Sections A.2.1 and A.2.2 we obtain,

$$\frac{\partial R}{\partial \ln u'_{\lambda^c s}} = -\Delta \chi_{\lambda^c s} \, P_s$$

$$\begin{aligned}
\frac{\partial R}{\partial \bar{T}_s} &= D\tau_s \frac{\partial B_s}{\partial \bar{T}_s} \\
&\quad - P_s \sum_k \left(u_{ks} \frac{\partial \kappa_{ks}}{\partial \bar{T}_s} \right) - \sum_{j=0}^n b_j \tau_j \sum_k \left(\kappa_{kj} \frac{\partial u_{kj}}{\partial \bar{T}_s} \right) \\
&\quad - \sum_{j=0}^n b_j \tau_j \sum_k \left(u_{ks} \frac{\partial \kappa_{ks}}{\partial \bar{p}_j} \right) \frac{\partial \bar{p}_j}{\partial \bar{T}_s} - \sum_{j=0}^n b_j \tau_j \sum_k \left(\kappa_{kj} \frac{\partial u_{kj}}{\partial \bar{p}_j} \right) \frac{\partial \bar{p}_j}{\partial \bar{T}_s} \\
&\quad - P_s \left(u'_{\lambda^0 s} \frac{\partial \kappa'_{\lambda^0 s}}{\partial \bar{T}_s} \right) - \sum_{j=0}^n b_j \tau_j \left(\kappa'_{\lambda^0 j} \frac{\partial u'_{\lambda^0 j}}{\partial \bar{T}_s} \right) \\
&\quad - \sum_{j=0}^n b_j \tau_j \left(u'_{\lambda^0 j} \frac{\partial \kappa'_{\lambda^0 j}}{\partial \bar{p}_j} \right) \frac{\partial \bar{p}_j}{\partial \bar{T}_s} - \sum_{j=0}^n b_j \tau_j \left(\kappa'_{\lambda^0 j} \frac{\partial u'_{\lambda^0 j}}{\partial \bar{p}_j} \right) \frac{\partial \bar{p}_j}{\partial \bar{T}_s}
\end{aligned} \tag{A.37}$$

$$\frac{\partial R}{\partial \bar{r}_{e_s}} = -P_s \left(u'_{\lambda^0 s} \frac{\partial \kappa'_{\lambda^0 s}}{\partial \bar{r}_{e_s}} + \kappa'_{\lambda^0 s} \frac{\partial u'_{\lambda^0 s}}{\partial \bar{r}_{e_s}} \right)$$

The conversion to derivatives defined on levels is carried out using Eqn A.7.

A.3 Limb-view weighting function calculations
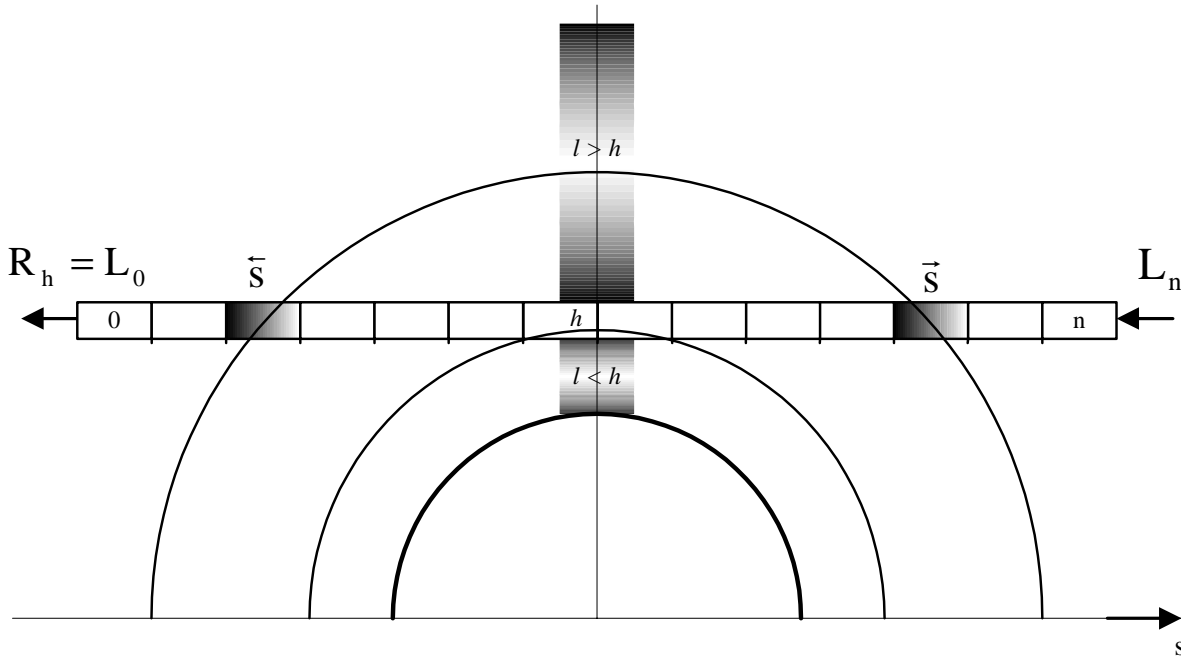
Figure A.2: Line-of-sight Schematic for weighting function calculations.

So far we have obtained the radiance derivatives for a change in a single line-of-sight element. Now we calculate the weighting functions for the limb-view case where the change in a vertical layer, l, is manifest in two line-of-sight elements on either side of the tangent point at $\overleftarrow{s}$ and $\overrightarrow{s}$ (Figure A.2). Hence, the weighting function matrix for layer defined quantities, $\bar{K}_{hl}$, is given by,

$$\bar{K}_{hl} = \frac{\partial R_h}{\partial \bar{q}_l} = \frac{\partial R_h}{\partial \bar{q}_{\overleftarrow{s}}} + \frac{\partial R_h}{\partial \bar{q}_{\overrightarrow{s}}} \tag{A.38}$$

where R_h is the radiance at tangent height, h.

The weighting function matrix, K_{hl}, for a state vector quantity, q, defined on levels, where R_h is the radiance at tangent height, h, and l is the vertical perturbation level is given by,

$$K_{hl} = \frac{\partial R_h}{\partial q_l} \tag{A.39}$$

These are related to the layer defined quantities, $\bar{q}$, by,

$$K_{hl} = \sum_i \frac{\partial R_h}{\partial \bar{q}_i} \frac{\partial \bar{q}_i}{\partial q_l} = \sum_i \bar{K}_{hi} \frac{\partial \bar{q}_i}{\partial q_l} \tag{A.40}$$

A.3.1 Volume mixing ratio layer weighting functions

$$\bar{K}_{hl} = \frac{\partial R_h}{\partial \ln u_{kl}} = -\left[\Delta\chi_{k\overleftarrow{s}} P_{\overleftarrow{s}} + \Delta\chi_{k\overrightarrow{s}} P_{\overrightarrow{s}} \right]$$

$$\tag{A.41}$$

$$= 0 \quad \text{if } l < h$$

A.3.2 Aerosol cross-section layer weighting functions

$$\bar{K}_{hl} = \frac{\partial R_h}{\partial \ln u'_{kl}} = -\left[\Delta\chi_{\lambda^c \overleftarrow{s}} P_{\overleftarrow{s}} + \Delta\chi_{\lambda^c \overrightarrow{s}} P_{\overrightarrow{s}} \right]$$

$$\tag{A.42}$$

$$= 0 \quad \text{if } l < h$$

A.3.3 Aerosol effective radius layer weighting functions

$$\bar{K}_{hl} = \frac{\partial R_h}{\partial \bar{r}_{e_l}}$$

$$= -\left[P_{\overleftarrow{s}} \left(u'_{\lambda^0 \overleftarrow{s}} \frac{\partial \kappa'_{\lambda^c \overleftarrow{s}}}{\partial \bar{r}_{e_{\overleftarrow{s}}}} + \kappa'_{\lambda^c \overleftarrow{s}} \frac{\partial u'_{\lambda^0 \overleftarrow{s}}}{\partial \bar{r}_{e_{\overleftarrow{s}}}} \right) \right.$$

$$\left. + P_{\overrightarrow{s}} \left(u'_{\lambda^0 \overrightarrow{s}} \frac{\partial \kappa'_{\lambda^c \overrightarrow{s}}}{\partial \bar{r}_{e_{\overrightarrow{s}}}} + \kappa'_{\lambda^c \overrightarrow{s}} \frac{\partial u'_{\lambda^0 \overrightarrow{s}}}{\partial \bar{r}_{e_{\overrightarrow{s}}}} \right) \right] \tag{A.43}$$

$$= 0 \quad \text{if } l < h$$

A.3.4 Temperature layer weighting functions

$$\bar{K}_{hl} = \frac{\partial R_h}{\partial \bar{T}_l} \quad \text{For} \quad l \geq h \quad \dots$$

$$= \left[D\tau_{\overleftarrow{s}} \frac{\partial B_{\overleftarrow{s}}}{\partial \bar{T}_{\overleftarrow{s}}} + D\tau_{\overrightarrow{s}} \frac{\partial B_{\overrightarrow{s}}}{\partial \bar{T}_{\overrightarrow{s}}} \right]$$

$$- \left[P_{\overleftarrow{s}} \sum_k \left(u_{k\overleftarrow{s}} \frac{\partial \kappa_{k\overleftarrow{s}}}{\partial \bar{T}_{\overleftarrow{s}}} \right) + P_{\overrightarrow{s}} \sum_k \left(u_{k\overrightarrow{s}} \frac{\partial \kappa_{k\overrightarrow{s}}}{\partial \bar{T}_{\overrightarrow{s}}} \right) \right.$$

$$+ \sum_{j=0}^{n} b_j \tau_j \sum_k \left(u_{k\overleftarrow{s}} \frac{\partial \kappa_{k\overleftarrow{s}}}{\partial \bar{p}_j} \right) \frac{\partial \bar{p}_j}{\partial \bar{T}_{\overleftarrow{s}}} + \sum_{j=0}^{n} b_j \tau_j \sum_k \left(\kappa_{kj} \frac{\partial u_{kj}}{\partial \bar{p}_j} \right) \frac{\partial \bar{p}_j}{\partial \bar{T}_{\overleftarrow{s}}}$$

$$+ \sum_{j=0}^{n} b_j \tau_j \sum_k \left(u_{k\overrightarrow{s}} \frac{\partial \kappa_{k\overrightarrow{s}}}{\partial \bar{p}_j} \right) \frac{\partial \bar{p}_j}{\partial \bar{T}_{\overrightarrow{s}}} + \sum_{j=0}^{n} b_j \tau_j \sum_k \left(\kappa_{kj} \frac{\partial u_{kj}}{\partial \bar{p}_j} \right) \frac{\partial \bar{p}_j}{\partial \bar{T}_{\overrightarrow{s}}}$$

$$\left. + \sum_{j=0}^{n} b_j \tau_j \sum_k \kappa_{kj} \frac{\partial u_{kj}}{\partial \bar{T}_l} \right]$$

$$\text{(A.44)}$$

$$- \left[P_{\overleftarrow{s}} u'_{\lambda^0 \overleftarrow{s}} \frac{\partial \kappa'_{\lambda^c \overleftarrow{s}}}{\partial \bar{T}_{\overleftarrow{s}}} + P_{\overrightarrow{s}} u'_{\lambda^0 \overrightarrow{s}} \frac{\partial \kappa'_{\lambda^c \overrightarrow{s}}}{\partial \bar{T}_{\overrightarrow{s}}} \right.$$

$$+ \sum_{j=0}^{n} b_j \tau_j \left(u'_{\lambda^0 \overleftarrow{s}} \frac{\partial \kappa'_{\lambda^0 \overleftarrow{s}}}{\partial \bar{p}_j} \right) \frac{\partial \bar{p}_j}{\partial \bar{T}_{\overleftarrow{s}}} + \sum_{j=0}^{n} b_j \tau_j \left(\kappa'_{\lambda^0 j} \frac{\partial u_{kj}}{\partial \bar{p}_j} \right) \frac{\partial \bar{p}_j}{\partial \bar{T}_{\overleftarrow{s}}}$$

$$+ \sum_{j=0}^{n} b_j \tau_j \left(u'_{\lambda^0 \overrightarrow{s}} \frac{\partial \kappa'_{\lambda^0 \overrightarrow{s}}}{\partial \bar{p}_j} \right) \frac{\partial \bar{p}_j}{\partial \bar{T}_{\overrightarrow{s}}} + \sum_{j=0}^{n} b_j \tau_j \left(\kappa'_{\lambda^0 j} \frac{\partial u'_{\lambda^0 j}}{\partial \bar{p}_j} \right)$$

$$\left. + \sum_{j=0}^{n} b_j \tau_j \, \kappa'_{\lambda^c j} \frac{\partial u'_{\lambda^0 j}}{\partial \bar{T}_l} \right]$$

$$\bar{K}_{hl} = \frac{\partial R_h}{\partial \bar{T}_l} \quad \text{For} \quad l < h \quad \dots$$

$$= - \left[\sum_{j=0}^{n} b_j \tau_j \sum_k \kappa_{kj} \frac{\partial u_{kj}}{\partial \bar{T}_l} + \sum_{j=0}^{n} b_j \tau_j \, \kappa'_{\lambda^c j} \frac{\partial u'_{\lambda^0 j}}{\partial \bar{T}_l} \right]$$

A.3.5 Reference pressure level

In addition to the weighting functions we have obtained with respect to constituent mixing ratio and temperature we must also calculate the weighting functions, $\partial R / \partial \zeta_r$, with respect to the reference pressure level, $\zeta_r = -\ln p$. The vertical gradient of the radiance in terms of the derivatives of the state vector is given by,

$$\frac{dR}{dz} = \sum_l \left(\frac{\partial R}{\partial q_l} \frac{\partial q_l}{\partial z} \right) + \sum_l \sum_k \left(\frac{\partial R}{\partial q_{kl}} \frac{\partial q_{kl}}{\partial z} \right) \quad \text{(A.45)}$$

Expanding this we obtain,

$$
\begin{aligned}
\frac{dR}{dz} = &\ \frac{\partial R}{\partial \zeta_r} \frac{\partial \zeta_r}{\partial z} \\
&+ \sum_l \left(\frac{\partial R}{\partial T_l} \frac{\partial T_l}{\partial z} \right) \\
&+ \sum_l \sum_k \left(\frac{\partial R}{\partial \ln v_{kl}} \frac{\partial \ln v_{kl}}{\partial z} \right) \\
&+ \sum_l \left(\frac{\partial R}{\partial \ln v'_{\lambda^\circ l}} \frac{\partial \ln v'_{\lambda^\circ l}}{\partial z} \right)
\end{aligned}
\tag{A.46}
$$

and rearranging yields the required weighting function in terms of previously calculated weighting functions and vertical gradients of the state vector quantities,

$$
\begin{aligned}
\frac{\partial R}{\partial \zeta_r} = \left(\frac{\partial \zeta_r}{\partial z} \right)^{-1} \Bigg[&\ \frac{\partial R}{\partial z} - \sum_l \left(\frac{\partial R}{\partial T_l} \frac{\partial T_l}{\partial z} \right) \\
&- \sum_l \sum_k \left(\frac{\partial R}{\partial \ln v_{kl}} \frac{\partial \ln v_{kl}}{\partial z} \right) \\
&- \sum_l \left(\frac{\partial R}{\partial \ln v'_{\lambda^\circ l}} \frac{\partial \ln v'_{\lambda^\circ l}}{\partial z} \right) \Bigg]
\end{aligned}
\tag{A.47}
$$

where $\partial \zeta_r / \partial z$ is obtained from the hydrostatic equation.

A.4   Spectral bandpass integration

Finally, we integrate the radiance and weighting functions over the channel spectral bandpass, $\Delta \nu$, with the filter function, $f(\nu)$, to obtain,

$$
R_h^{\Delta \nu} = \int_{\Delta \nu} f(\nu) R_h(\nu) d\nu
\tag{A.48}
$$

$$
K_{hl}^{\Delta \nu} = \int_{\Delta \nu} f(\nu) K_{hl}(\nu) d\nu
\tag{A.49}
$$

B   Level-2 Data Product Description

B.1   Overview

Size	175 MB / 24-hour
Format	HDF-EOS Swath
Sampling Frequency	1 Profile (9.6 seconds)
Content	Retrieved Geolocated Science Profiles and Ancillary Parameters
Basic Record	Vertical Profile (145 levels)

Table B.1: Level-2 Product Format.

The Level-2 data product (Table B.1) is a daily file, in an HDF-EOS swath format, containing geolocated atmospheric profiles of geophysical quantities, such as temperature and constituent mixing ratios, and associated ancillary information, such as profile location, spacecraft location and scan information.

B.2   Level-2 Data Content

The Level-2 data consist of retrieved geolocated geophysical parameters as well as associated ancillary data. The data, presented below in Tables B.2 and B.3, are on a per profile basis, and give the type of the parameter, name, a brief description, and the units of the parameter. The first eleven parameters are ancillary data used to locate each profile and provide additional information about modes of the instrument and location of the spacecraft. The remaining parameters contain retrieved vertical profiles, where each level in the profile is related to pressure by Eqn 83.

All ancillary data are reported with every profile including time, tangent point information, scan mode and direction, and spacecraft location. The time is reported in International Time (TAI93) at the 50 mb pressure level. The tangent point information includes: latitude, longitude, local time and solar zenith angle all given at the 50 mb level. Spacecraft location is reported in ECR coordinates respective to the 50 mb level.

Level 2 (t = 1 profile, profile = 145 levels)					
Parameter	**Units**	**Type**	**Bytes**	**Bytes/Profile**	**Description**
Time		double	8	8	TAI93 time for channel 14 50 mb tangent point
Latitude	degrees	float	4	4	Latitude for channel 14 50 mb tangent point
Longitude	degrees	float	4	4	Longitude for channel 14 50 mb tangent point
Orbitdir		byte	1	1	Orbit direction: ascending/descending
Scanmode		short	2	2	HIRDLS Science Scan Mode
Scandir		byte	1	1	Scan Direction: up/down
Solar zenith angle	degrees	float	4	4	Solar Zenith Angle for channel 14 50 mb tangent point
Local Solar time		float	4	4	Local Solar Time for channel 14 50 mb tangent point
Spacecraft Latitude	degrees	float	4	4	Spacecraft Latitude for channel 14 50 mb tangent point
Spacecraft Longitude	degrees east	float	4	4	Spacecraft Longitude for channel 14 50 mb tangent point
Spacecraft Altitude	km	float	4	4	Spacecraft Altitude for channel 14 50 mb tangent point
Z	km	float	4	580	Profile of Approximate Tangent Point Altitudes
Temperature	K	float	4	580	Profile of Temperature
O3	ppv	float	4	580	Profile of Ozone Mixing Ratio
H2O	ppv	float	4	580	Profile of Water Vapor Mixing Ratio
ClONO2	ppv	float	4	580	Profile of Chlorine Nitrate Mixing Ratio
N2O5	ppv	float	4	580	Profile of Nitrogen Pentoxide Mixing Ratio
N2O	ppv	float	4	580	Profile of Nitrous Oxide Mixing Ratio
NO2	ppv	float	4	580	Profile of Nitrogen Dioxide Mixing Ratio
CH4	ppv	float	4	580	Profile of Methane Mixing Ratio
HNO3	ppv	float	4	580	Profile of Nitric Acid Mixing Ratio
CFC11	ppv	float	4	580	Profile of CFC 11 Mixing Ratio
CFC12	ppv	float	4	580	Profile of CFC 12 Mixing Ratio
Aerosol01	1/km	float	4	580	Profile of Aerosol Extinction (channel 1)
Aerosol06	1/km	float	4	580	Profile of Aerosol Extinction (channel 6)
Aerosol13	1/km	float	4	580	Profile of Aerosol Extinction (channel 13)

Table B.2: Level-2 Product Data Description.

Table B.3: Level-2 Product Data Description continued.

Aerosol19	1/km	float	4	580	Profile of Aerosol Extinction (channel 19)
Aerosol Effective Radius	microns	float	4	580	Profile of Aerosol Effective Radius
Clouds		int	4	580	Profile of Cloud Presence Indicator
Temperature Error	K	float	4	580	Profile of Temperature Error
Pressure Error	hPa	Float	4	580	Profile of Pressure Error
O3 Error	ppv	float	4	580	Profile of Ozone Mixing Ratio Error
H2O Error	ppv	float	4	580	Profile of Water Vapor Mixing Ratio Error
ClONO2 Error	ppv	float	4	580	Profile of Chlorine Nitrate Mixing Ratio Error
N2O5 Error	ppv	float	4	580	Profile of Nitrogen Pentoxide Mixing Ratio Error
N2O Error	ppv	float	4	580	Profile of Nitrous Oxide Mixing Ratio Error
NO2 Error	ppv	float	4	580	Profile of Nitrogen Dioxide Mixing Ratio Error
CH4 Error	ppv	float	4	580	Profile of Methane Mixing Ratio Error
HNO3 Error	ppv	float	4	580	Profile of Nitric Acid Mixing Ratio Error
CFC11 Error	ppv	float	4	580	Profile of CFC 11 Mixing Ratio Error
CFC12 Error	ppv	float	4	580	Profile of CFC 12 Mixing Ratio Error
Aerosol01 Error	1/km	float	4	580	Profile of Aerosol Extinction Error (channel 1)
Aerosol06 Error	1/km	float	4	580	Profile of Aerosol Extinction Error (channel 6)
Aerosol13 Error	1/km	float	4	580	Profile of Aerosol Extinction Error (channel 13)
Aerosol19 Error	1/km	float	4	580	Profile of Aerosol Extinction Error (channel 19)
Aerosol Effective Radius Error	microns	float	4	580	Profile of Aerosol Effective Radius Error

Total Megabytes per Profile	0.02034
Total Megabytes per Day	174.924

References

[*Andrews* (1974)] H.C. Andrews, "Digital image restoration: A survey", *IEEE Comp.*, **7**, 36–45, 1974.

[*Andrews and Hunt* (1977)] H.C. Andrews and B. R. Hunt, "Digital Image Restoration", Englewood Cliffs, NJ, Prentice-Hall, 1977.

[*Bailey and Gille* (1986)] P.L. Bailey and J.C. Gille, "Inversion of limb radiance measurements: An operational algorithm", *J. Geophys. Res.*, **91**, 2757–2774, 1986.

[*Ballard et al.*(1988)] J. Ballard, W. B. Johnston, M. R. Gunson, and P. T. Wassell, "Absolute absorption coefficient of ClONO$_2$ infrared bands at stratospheric temperature", *J. Geophys. Res.*, **93**, 1659–1665, 1988.

[*Ballard et al.*(1996)] J. Ballard, P. E. Morris, T. J. Nightingale, J. Firth, R. J. Knight, C. W. P. Palmer, P. Venters, R. J. Wells, and J. G. Whitney, "Calibration of the improved stratospheric and mesospheric sounder I: Introduction, spectral and radiometric calibration", *J. Atmos. Ocean. Tech.*, **13**, 810–831, 1996.

[*Banham and Katsaggelos* (1977)] M.R. Banham and A. K. Katsaggelos, "Digital image restoration", *IEEE Sig. Proc. Mag.*, , 24–41, 1997.

[*Barber et al.*(1990)] P. W. Barber and S. C. Hill, Light Scattering by Particles, Computational Methods, World Scientific, New Jersey, 1990.

[*Born and Wolf* (1975)] M. Born and E. Wolf, Principles of Optics, Pergammon Press, Oxford, 1975.

[*Brault and White* (1971)] J.W. Brault and O. R. White, "The analysis and restoration of astronomical data via the fast Fourier transform", *Astron. Astrophys*, **13**, 169–189, 1971.

[*Browell et al.*(1990)] E. V. Browell, C. F. Butler, S. Ismail, P. A. Robinetter, A. F. Carter, N. S. Higdon, O. B. Toon, M. R. Schoeberl, and A. F. Tuck, "Airborne lidar observations in the wintertime arctic stratosphere: Polar stratospheric clouds", *Geophys. Res. Lett.*, **17**, 385–388, 1990.

[*Carslaw et al.*(1994)] K. S. Carslaw, B. P. Luo, S. L. Clegg, Th. Peter, P. Brimblecombe and P. J. Crutzen, "Stratospheric aerosol growth and HNO$_3$ gas phase depletion from coupled HNO$_3$ and water uptake by liquid particles", *Geophys. Res. Lett.*, **21**, 2479–2482, 1994.

[*Clough et al.*(1996)] S. A. Clough, F.X. Kneizys, R. Davies, R. Gamache, and R. Tipping, "Theoretical line shape for H$_2$O vapor; Application to the continuum", in Atmospheric Water Vapor, pp 25–46, eds. A. Deepak et al., Academic Press, 1980.

[*de Boor* (1978)] C. de Boor, "A practical guide to splines", Springer-Verlag, New York, 1978.

[*Deshler et al.*(1993)] T. Deshler, B. J. Johnson, and W. R. Rozier, "Balloonborne measurements of Pinatubo aerosol during 1991 and 1992 at 41°N: Vertical profiles, size distributions, and volatility", *Geophys. Res. Lett.*, **20**, 1435–1438, 1993.

[*Draine et al.*(1994)] B. T. Draine and P. J. Flatau, "Discrete-dipole approximation for scattering calculations", *J. Opt. Soc. Am. A.*, **11**, 1491–1499, 1994.

[*Drummond et al.*(1980)] J. R. Drummond, J. T. Houghton, G. D. Peskett, C. D. Rodgers, M. J. Wale, J. G. Whitney, and E. J. Williamson, "The stratospheric and mesospheric sounder on Nimbus 7", *Phil. Trans. R. Soc. London, Ser. A*, **296**, 219–241, 1980.

[*Dye et al.*(1992)] J. E. Dye, D. Baumgardner, B. W. Gandrud, S. R. Kawa, K. K. Kelly, M. Lowenstein, G. V. Ferry, K. R. Chan, and B. L. Gary, "Particle size distributions in arctic polar stratospheric clouds, growth and freezing of sulfuric acid droplets, and implications for cloud formation", *J. Geophys. Res.*, **97**, 8015–8034, 1992.

[*Echele et al.*(1998)] G. Echele, T. von clarmann, and H. Oelhaf, "Optical and microphysical parameters of the Mt. Pinatubo aerosol as determined from MIPAS-B mid-IR limb emission spectra", *J. Geophys. Res.*, **103**, 19,193–19,211, 1998.

[*Edwards et al.*(1991)] D. P. Edwards, and L. L. Strow, "Spectral line shape considerations for limb path temperature sounders", *J. Geophys. Res.*, **93**, 1659–1665, 1991.

[*Edwards* (1992)] D. P. Edwards, "GENLN2: A general line-by-line atmospheric transmittance and radiance model", NCAR Technical Note 367+STR, National Center for Atmospheric Research (1992).

[*Edwards et al.*(1993)] D. P. Edwards, M. López-Puertas, and M. A. López-Valverde, "Non-local thermodynamic equilibrium studies of the 15-μm bands of CO_2 for atmospheric remote sensing", *J. Geophys. Res.*, **98**, 14,955–14,977, 1993.

[*Edwards et al.*(1994)] D. P. Edwards, M. López-Puertas, and M . G. Mlynczak, "Non-local thermodynamic equilibrium radiance from O_3 and CO_2 in the 9–11-μm spectral region", *J. Quant. Spectrosc. Radiat. Transfer*, **52**, 389–407, 1994.

[*Edwards et al.*(1995)] "Selection of sounding channels for the high resolution dynamics limb sounder", *Appl. Opt.*, **34**, 7006–7018, 1994.

[*Edwards et al.*, *in preparation*] D. P. Edwards, C. Halvorson, and J.C. Gille, "Radiative transfer for the EOS-AM1 MOPITT instrument", in preparation.

[*Fu et al.*(1993)] Q. Fu and K. N. Liou, "Parameterization of the radiative properties of cirrus clouds", *J. Atmos. Sci.*, **50**, 2008, 1993.

[*Gille and Bailey* (1978)] J.C. Gille and P.L. Bailey, "Information content and results of nonlinear inversion of Nimbus 6 limb radiance inversion data", in Remote Sensing of the Atmosphere: Inversion Methods and Applications, eds A.L. Fymat and V.E. Zuev,, Elsevier North-Holland, New York, 107–113, 1978.

[*Gille and House* (1971)] J. C. Gille and F. B. House, "On the inversion of limb radiance measurements I: Temperature and thickness", *J. Atmos. Sci.*, **28**, 1427–1442, 1971.

[*Gille et al.*(1980a)] J. C. Gille, P. L. Bailey, R. A. Craig, F. B. House, and G. P. Anderson, "Sounding the stratosphere and mesosphere by infrared limb scanning from space", *Science*, **208**, 397–399, 1980.

[*Gille et al.*(1980b)] J. C. Gille, P. L. Bailey, and J. M. Russell III, "Temperature and composition measurements from the LRIR and LIMS experiments on NIMBUS 6 and NIMBUS 7", *Phil. Trans. R. Soc. Lond. A*, **296**, 205–218, 1980.

[*Gille and Russell* (1984)] J. C. Gille, and J. M. Russell III, "The limb infrared monitor of the stratosphere: Experiment description, performance, and results", *J. Geophys. Res.*, **89**, 5125–5140, 1984.

[*Gille et al.*(1992)] J. C. Gille, and J. J. Barnett, "The high resolution dynamics limb sounder (HIRDLS). An instrument for the study of global change", *Rendiconti S. I. F.*, **CXV**, 433–450, 1992.

[*Gobbi et al.*(1998)] G. P. Gobbi, G. D. Donfrancesco, and A. Adriani, "Physical properties of stratospheric clouds during the Antarctic winter of 1995", *J. Geophys. Res.*, **103**, 10,859–10,874, 1998.

[*Goody and Yung* (1989)] R. M. Goody and Y. L. Yung, Atmospheric Radiation: Theoretical Basis, Oxford University Press, 1989.

[*Grainger et al.*(1995)] R. G. Grainger, A. Lambert, C. D. Rodgers, F. W. Taylor, and T. Deshler, "Stratospheric aerosol effective radius, surface, and volume estimated from infrared measurements", *J. Geophys. Res.*, **100**, 16,507–16,518, 1995.

[*Grose et al.*(1994)] W. Grose and J. C. Gille (eds) "Upper atmosphere research satellite validation workshop IV report: Temperature and constituents", NASA Langley Research Center, Hampton VA, Sept. 19–21, 1994.

[*Hamill et al.*(1997)] P. Hamill, E. J. Jensen, P. B. Russell, and J. J. Bauman, "The life cycle of stratopsheric aerosol particles", *Bull. Am. Met. Soc.*, **78**, 1395–1410, 1997.

[*Heymsfield et al.*(1986)] A.J. Heymsfield, "Ice particles observed in a cirriform cloud at -83 c and implications for polar stratospheric clouds", *J. Atmos. Sci.*, **43**, 851–855, 1986.

HIRDLS Instrument Requirements Document (IRD), SC-HIR-018, 1997.

HIRDLS Pre-launch Calibration Plan, TP-HIR-007, 1998.

HIRDLS Scientific Data Product Validation Plan, SC-HIR-022, 1997.

[*Houze* (1993)] R. A. Houze, Cloud Dynamics, Academic Press, San Diego, 1993.

[*Humlicek et al.*(1982)] J. Humlicek, "Optimized computation of the Voigt and complex probability functions", *J. Quant. Spectrosc. Radiat. Transfer*, **27**, 437–444, 1982.

[*Kerridge et al.*(1989)] B. J. Kerridge, and E. E. Remsberg, "Evidence from the limb infrared monitor of the stratosphere for nonlocal thermodynamic equilibrium in the ν_2 mode of mesospheric water vapour and the ν_3 mode of stratospheric nitrogen dioxide", *J. Geophys. Res.*, **94**, 16,323–16,342 (1989).

[*Kneizys et al.*(1988)] F. X. Kneizys, E. P. Shettle, L. W. Abreu, J. H. Chetwynd, G. P. Anderson, W. O. Gallery, J. E. A. Selby, and S. A. Clough, "User guide to LOWTRAN-7", AFGL-TR-88-0177, AFGL(OPI), Hanscom AFB, MA 01731, 1988.

[*Knittl et al.*(1976)] Z. Knittl, Optics of Thin Films, John Wiley & Sons, 1976.

[*Lambert et al.*(1993)] A. Lambert, R. G. Grainger, J. J. Remedios, W. J. Reburn, C. D. Rodgers, M. Corney, and F. W. Taylor, "Measurements of the evolution of the Mt. Pinatubo aerosol cloud by ISAMS", *Geophys. Res. Lett.*, **20**, 1287–1290, 1993.

[*Lacis and Oinas* (1991)] A. A. Lacis and V. Oinas, "A description of the correlated-k distribution method for modeling nongray gaseous absorption, thermal emission, and multiple scattering in vertically inhomogeneous atmospheres", *J. Geophys. Res.*, **96**, 9027–9063, 1991.

[*Li and Varanasi* (1994)] Z. Li and P. Varanasi, "Measurement of the absorption cross-sections of CFC-11 at conditions representing various model atmospheres", *J. Quant. Spectrosc. Radiat. Transfer*, **52**, 137–144, 1994.

[*Liou et al.*(1980)] K. N. Liou, An Introduction to Atmospheric Radiation, Academic Press, New York, 1980.

[*López-Puertas et al.*(1992)] M. López-Puertas, M. A. López-Valverde, and F. W. Taylor, "Vibrational temperatures and radiative cooling of the CO_2 15-μm bands in the middle atmosphere", *Q. J. R. Meteorol. Soc.*, **118**, 499–532, 1992.

[*Macke* (1993)] A. Macke, "Scattering of light by polyhedral ice crystals", *Appl. Opt.*, **32**, 2780–2788, 1993.

[*Marks and Rodgers* (1993)] C. J. Marks and C. D. Rodgers, "A retrieval method for atmospheric composition from limb emission measurements", *J. Geophys. Res.*, **98**, 14,939–14,953, 1993.

[*Massie et al.*(1994)] S. T. Massie, "Indices of refraction for the HITRAN compilation", *J. Quant. Spectrosc. Radiat. Transfer*, **52**, 501–513, 1994.

[*Massie et al.*(1996)] S. T. Massie, T. Deshler, G. E. Thomax, J. L. Mergenthaler, and J. M. Russell III, "Evolution of the infrared properties of the Mount Pinatubo aerosol cloud over Laramie, Wyoming", *J. Geophys. Res.*, **101**, 23,007–23,019, 1996.

[*McCormick et al.*(1982)] M. P. McCormick, H. M. Steele, P. Hamill, W. P. Chu, and T. J. Swissler, "Polar strato-spheric cloud sightings by SAM II", *J. Atmos. Sci.*, **39**, 1387–1397, 1982.

[*McDaniel et al.*(1990)] A. H. McDaniel, C. A. Cantrell, J. A. Davidson, R. E. Shetter, and J. G.. Calvert, "The temperature dependent, infrared absorption cross sections for the chloroflorocarbons: CFC–11, CFC–12, CFC–13, CFC–14, CFC–22, CFC–113, CFC–114, and CFC–115", *J. Atmos. Chem.*, **12**, 211–227, 1990.

[*McFarquhar and Heymsfield* (1994)] G. M. McFarquhar and A. J. Heymsfield, Parameterization of Tropical Cir-rus "Ice Crystal Size Distributions and Implications for Radiative Transfer: Results from CEPEX", *J. Atmos. Sci.*, **54**, 2187–2200, 1997.

[*Mishchenko et al.*(1996)] M. I. Mishchenko, L. D. Travis, and D. W. Mackowski, "T-matrix computations of light scattering by nonspherical particles: A review", *J. Quant. Spect. Radiat. Transf.*, **55**, 535–575, 1996.

[*Niedziela et al.*(1998)] R. F. Niedziela, M. L. Norman, R. E. Miller, and D. R. Worsnop, "Temperature- and composition-dependent infrared optical constants for sulfuric acid", *Geophys. Res. Lett.*, **25**, 4477–4480, 1998.

[*Orlando et al.*(1991)] J. J. Orlando, G. S. Tyndall, K. E. Nickerson, and J. G. Calvert, "The temperature depen-dence of collision-induced absorption by oxygen near 6 μm", *J. Geophys. Res.*, **96**, 20,755–20,760, 1991.

[*Orlando et al.*(1992)] J. J. Orlando, G. S. Tyndall, A. Huang, and J. G. Calvert, "Temperature dependence of the infrared absorption cross sections of carbon tetrachloride", *Geophys. Res. Lett.*, **19**, 1005–1008 (1992).

[*Palmer and Williams* (1976)] K.F. Palmer and D. Williams, "Optical constants of sulfuric acid; application to the clouds of Venus?", *Appl. Opt.*, **14**, 208–219, 1975.

[*Peckham* (1995)] G.E. Peckham, "The vertical resolution of satellite borne radiometers for atmospheric measure-ments", *Int. J. Rem. Sens*, **16**, 1557–1569, 1995.

[*Roche et al.*(1993)] A. E. Roche, J. B. Kumer, J. L. Mergenthaler, G. A. Ely, W. G. Uplinger, J. F. Potter, T. C. James, and L. W. Serritt, "The cryogenic limb array etalon spectrometer (CLAES) on UARS: Experiment description and performance", *J. Geophys. Res.*, **96**, 10,763–10,775, 1993.

[*Rodgers* (1976)] C. D. Rodgers, "Retrieval of atmospheric temperature and composition from remote measure-ments of thermal radiation", *J. Geophys. Res.*, **14**, 609–624, 1976.

[*Rodgers* (1990)] C. D. Rodgers, "Characterization and error analysis of profiles retrieved from remote sounding measurements", *J. Geophys. Res.*, **95**, 5587–5595, 1990.

[*Rodgers et al.*(1996)] C. D. Rodgers, R. J. Wells, R. G. Grainger, and F. W. Taylor, "Improved stratospheric and mesospheric sounder validation: General approach and in-flight radiometric calibration", *J. Geophys. Res.*, **101**, 9775–9793, 1996.

[*Rodgers, in preparation*] C. D. Rodgers, Inverse Methods for Atmospheric Sounding: Theory and Practice, `http://www.atm.ox.ac.uk/user/rodgers/`.

[*Rothman et al.*(1992)] L. S. Rothman, R. R. Gamache, R. H. Tipping, C. P. Rinsland, M. A. H. Smith, D. Chris Benner, V. Malathy Devi, J. -M. Flaud, C. Camy-Peyret, A. Perrin, A. Goldman, S. T. Massie, L. R. Brown, and R. A. Toth, "The HITRAN database: Editions of 1991 and 1992", *J. Quant. Spectrosc. Radiat. Transfer*, **48**, 469–507, 1992.

[*Rothman et al.*(1998)] L. S. Rothman, et al., "The HITRAN molecular spectroscopic database and HAWKS (HI-TRAN atmospheric workstation): 1996 edition", *J. Quant. Spectrosc. Radiat. Transfer*, **60**, 665–710, 1998.

[*SDP Toolkit* (1995)] Theoretical Basis of the SDP Toolkit Geolocation Package for the ECS Project, 445-TP-002-002, Hughes Information Technology Systems, Landover, MD, May 1995.

[*Seals et al.*(1991)] R. Seals, "UARS Climatology, NASA Langley Research Center", Unpublished, 1991.

[*Steele and Hamill* (1982)] H.M. Steele and P. Hamill, "Effects of temperature and humidity on the growth and optical properties of sulfuric acid-water droplets in the stratosphere", *J. Aerosol. Sci.*, **12**, 517–528, 1981.

[*Taylor et al.*(1993)] F. W. Taylor, C. D. Rodgers, J. G. Whitney, S. T. Werrett, J. J. Barnett, G. D. Peskett, P. Venters, J. Ballard, C. W. P. Palmer, R. J. Knight, P. Morris, T. Nightingale, and A. Dudhia, "Remote Sensing of atmospheric structure and composition by pressure modulator radiometry from space: The ISAMS experiment on UARS", *J. Geophys. Res.*, **98**, 10,799–10,814, 1993.

[*Tisdale et al.*(1998)] R. T. Tisdale, D. L. Glandorf, M. A. Tolbert, and O. B. Toon, "Infrared optical constants of low-temperature H_2SO_4 solutions representative of stratospheric sulfate aerosols", *J. Geophys. Res.*, **103**, 25,353–25,370, 1998.

[*Toon et al.*(1994)] O. B. Toon, M. A. Tolbert, B. G. Koehle, A. M. Middlebrook, and J. Jordan, "Infrared optical constants of H_2O ice, amorphous nitric acid solutions, and nitric acid hydrates", *J. Geophys. Res.*, **99**, 25,631–25,654, 1994.

[*van de Hulst* (1975)] H. C. van de Hulst, Light Scattering by Small Particles, Wiley, New York, 1975.

[*Varanasi and Nemtchinov* (1994)] P. Varanasi and V. Nemtchinov, "Thermal infrared absorption coefficients of CFC-12 at atmospheric conditions", *J. Quant. Spectrosc. Radiat. Transfer*, **51**, 679–687, 1991.

[*Wang et al.*(1996)] P-H. Wang, P. Minnis, M. P. McCormick, G. S. Kent, and K. M. Skeens, "A 6-year climatology of cloud occurrence frequency from Stratopsheric Aerosol and Gas Experiment II observations (1985-1990)", *J. Geophys. Res.*, **101**, 29,407–29,429, 1996.